Ruddlesden-Popper type phases in the Ln-Sr-Fe-O (Ln = La, Nd; n = 3) system

Synthesis & Characterization

Junshan Li

Master Thesis in Materials, Energy and Nanotechnology

Faculty of Mathematics and Natural Sciences

UNIVERSITY OF OSLO

August 2013

Preface

This thesis is the review of my master work and experiments, as an essential part of a two-year MSc program at the University of Oslo. The work was conducted from September 2011 to August 2013 under the NAFUMA (Nanostructure and Functional Materials) research group at the center for Materials Science and Nanotechnology (SMN), Department of Chemistry.

Acknowledgments

Pursuing a MSc degree in Norway has proved a definite choice. Considerable support and help have been given to make this research possible by those extraordinary people and I cherish this precious opportunity to express my gratitude to them.

First, I would like to show my deepest gratitude to my supervisor prof. Helmer and prof. Anja for their wonderful guidance, patience and support on the experiment as well as comments on the thesis. I really benefited a lot in many aspects.

Here, I am also very grateful to these fantastic guys who are in the NAFUMA research group, Chris, Pushpaka, Eirini, Per, Marius, Hanyan Song, Yang Hu and David for teaching and helping me, and your advice was helpful especially when I was confused.

Many thanks, of course, I want to give to Sindre, Hanne, Østain, Ammun, Jon magnus and Carla, it was so nice to share office and work with you. Your jokes, stories… made my life in Norway more colorful.

I would like to thank all my friends who have made these two years of my life unforgettable.

Yet, most of all, I want to thank my parents and sister for their spiritual and financial support, which ensure I can finish my study here. I still could feel their love and care even I was very far away from home.

Junshan Li

University of Oslo, Norway

22 August 2013

Abstract

In our modern society, the consumption and demand for energy is increasing rapidly. Fuel cells (FCs) provide renewable energy by electrochemically converting chemical energy into electrical energy and heat without direct combustion as an intermediate step. Solid oxide fuel cells (SOFCs) have some advantages over other types of fuel cells. Here, the cathode materials have a large impact on the performance of SOFCs. The Ruddlesden-Popper (RP) types oxides, such as the RP3 phase $Ln(Sr,Ca)_3(Fe,Co)_3O_{10}$, are promising cathode materials due to their good mixed ionic and electronic conductivity (MIEC).

The objective of this master work has been to synthesize RP3 phase $Ln_xSr_{4-x}Fe_3O_{10-\delta}$ (Ln = La, Nd; $0 < x < 4.0$) via citric acid method. In addition, the investigation of the crystal structure, thermal behavior and magnetic property of this RP3 type compounds represents a main task.

A large number of compositions were attempted synthesized. The crystal structure of the RP3 products consists of a triple perovskite slabs separated by rock salt layer. A novel finding is that certain compositions with $0 < x \leq 1.0$ are phase-pure, hence representing a heterovalent substitution that simultaneously changes the average oxidation state for the iron atoms. The unit cell parameters for the as-synthesized RP3 type compounds are consistent with a tetragonal, space group I4/mmm and with dimensions $a = b \approx 3.85$ Å, $c \approx 28.00$ Å.

The main focus has been on samples with $x = 1.0$. Among the obtained phase-pure compounds, $LnSr_3Fe_3O_{10-\delta}$ (Ln = La, Nd) was selected for preparing derivate materials through tuning the concentration of oxygen vacancies ($0 < \delta < {\sim}1.5$), applying methods of full oxidation at low temperatures, quenching and an oxygen-getter method.

Conventional powder X-ray (XRD) as well as Synchrotron radiation X-ray diffraction (SRXRD) data were collected and used as input to Rietveld refinement in order to describe the atomic arrangement of these oxygen deficient samples. The oxygen vacancies are located to the equatorial layer of the central octahedra in the triple perovskite block. The length of the c-axis varies linearly with oxygen vacancy concentration, increasing in length upon decreasing the oxygen content. The Fe-O and La/Sr-O bond length and their bond valence sum (BVS) calculated from the Rietveld refinement are evaluated and discussed to present changes connected with oxygen deficiencies.

Thermogravimetric analysis (TGA) was carried out from 30 ^{o}C to 1200 ^{o}C with a rate of 10 ^{o}C/min in air. For the oxidized samples, oxygen is lost upon heating. However, reintercalation of oxygen occurs reversibly as a function of temperature. The oxygen deficient samples are found to be kinetically stable until some 200 ^{o}C, thereafter followed by a dramatic oxygen intercalation until 400 ^{o}C. Then a mass loss starts and continues up to elevated temperature of 1200 ^{o}C. Reversible weight gain is observed upon cooling due to oxygen intercalation.

The magnetization as a function of temperature (M(T)) and field (M(H)) was measured for these two series compounds $LnSr_3Fe_3O_{10-\delta}$ (Ln = La, Nd). With different Fe state, ferromagnetic and antiferromagnetic exchange interactions are present in $LnSr_3Fe_3O_{10-\delta}$ and hysteresis loop shows that this series compounds are of paramagnetic at high temperatures , and probably quite generally antiferro- or ferrimagnetic at 5K.

List of abbreviations

RP	Ruddlesden-Popper phase
RPn	Ruddlesden Popper phase with n perovskite layers alternating AO layer
FCs	Fuel Cells
SOFCs	Solid Oxide Fuel Cells
MLCCs	Multi-Layer Ceramic Capacitors
MIEC	Mixed Ionic and Electronic Conductor/Conductivity
HTS	High Temperature Superconductor
LTS	Low Temperature Superconductor
RT	Room Temperature
TGA	Thermogravimetric Analysis
XRD	X-ray Diffraction
SRXRD	Synchrotron Radiation X-ray Diffraction
D	Dimension/Dimensional
HS	High Spin
LS	Low Spin
JT	John-Teller
CD	Charge Disproportionation
CO	Charge Ordering
CN	Coordination number
NPD	Neutron Powder Diffraction
PM	Paramagnetic
FM	Ferromagnetic
AFM	Anti-Ferromagnetic
SG	Spin Glass
a_p	The dimension of a primitive perovskite cubic cell

PPMS	Physical Properties Measurement System
MPMS	Magnetic Properties Measurement System
SNBL	Swiss-Norwegian Beam Line
ESRF	European Synchrotron Radiation Facility
TOPAS	TOtal Pattern Analysis Solutions
GSAS	General Structure Analysis System
FC	Field Cooling
ZFC	Zero Field Cooling
M(T)	Magnetization as a function of temperature
M(H)	Magnetization as a function of external applied field
χ	Magnetic susceptibility
χ^{-1}	Inverse magnetic susceptibility
u_{eff}	effective paramagnetic moment
B.M.	Bohr magneton
A/B/X	Atomic site/cation in Ruddlesden-Popper and perovskite
Ln	Rare earth element
δ	Overall oxygen nonstoichiometry per formula unit
$10-\delta$	Overall oxygen content per formula unit
ICSD	Inorganic Crystal Structure Database
SQUID	Superconducting Quantum Interface Device

Contents

路漫漫其修远兮，吾将上下而求索。

Endless is the truth, we shall spare no pains to seek and explore.

Chapter 1

Introduction and background

Perovskite type compounds and related structures, represent a large family of important inorganic materials, which have been widely used in industry and comprehensively studied in laboratory due to their wide variation of useful and also exotic properties. The Ruddlessden-Popper type oxides, have a kind of layered perovskite crystal structure, and they show frequently intriguing physical properties. Both these categories of oxides are heavily studied in the NAFUMA research group at the Department of Chemistry, University of Oslo.

Introducing provskite to chemists, as a master student, is a bit like introducing the Moonlight Sonata to Beethoven. However, for interested readers, comprehensive textbooks of depth to pervoskite and its related structures by Mitchell [1], Francis S [2], Alexandra Navrotsky [3] and Maxim Borowski [4] etc. are available.

Here, the first chapter presents a general introduction to the perovskite and related types of materials, including descriptions of cation substitutions and oxygen deficiency. Some technical applications of RP3 (Ln-Sr-M-O) phase oxide, a short literature review and the objective of this work will be illustrated thereafter.

1.1 Introduction to perovskite type compounds

The mineral perovskite, was named after a Russian mineralogist Count Lev Provski Von, who firstly discovered it in Ural Mountains in 1839 [5]. Then the term perovskite was used to describe a class of compounds sharing the same general stoichiometry and connectivity with $CaTiO_3$ [6], which was the first synthesized perovskite by Goldschmidt in 1926 at the University of Oslo.

As a versatile inorganic structure, the perovskite structure has the general formula ABX_3 with stoichiometry of 1:1:3, nearly all the stable elements in the periodic table has been studied in the perovskite framework [7]. As shown in Figure 1, A is an alkali, alkaline earth metal or rare-earth metal element, B is usually a transition metal element, while X is an anion such as F, Cl, Br, I and even H, etc. but usually O.

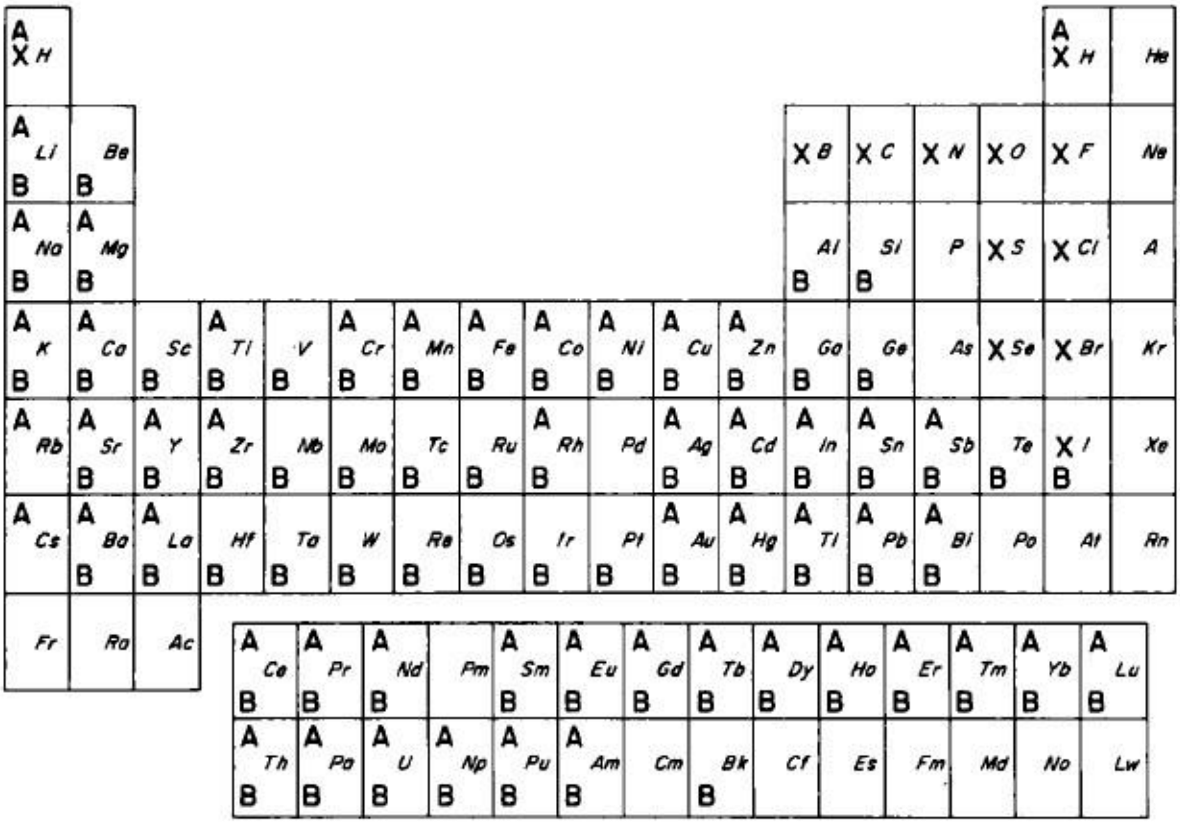

A X H																A X H	He
A Li B	Be B											X B	X C	X N	X O	X F	Ne
A Na B	A Mg B											Al B	Si B	P	X S	X Cl	A
A K B	A Ca B	Sc B	A Ti B	V B	A Cr B	A Mn B	A Fe B	A Co B	A Ni B	A Cu B	A Zn B	Ga B	Ge B	As	X Se	X Br	Kr
A Rb	A Sr B	A Y B	A Zr B	Nb B	Mo B	Tc B	Ru B	A Rh B	Pd	A Ag B	A Cd B	A In B	A Sn B	A Sb B	Te B	X I B	Xe
A Cs	A Ba B	A La B	Hf B	Ta B	W B	Re B	Os B	Ir B	Pt B	A Au B	A Hg B	A Tl B	A Pb B	A Bi B	Po	At	Rn
Fr	Ra	Ac															

A Ce B	A Pr B	A Nd B	Pm	A Sm B	A Eu B	A Gd B	A Tb B	A Dy B	A Ho B	A Er B	A Tm B	A Yb B	A Lu B
A Th B	A Pa B	A U B	A Np B	A Pu B	A Am B	Cm	Bk B	Cf	Es	Fm	Md	No	Lw

Figure 1. Survey of the chemical elements that are known to be in the A, B and X site [7]

The perovskite structure was established in 1945 by Helen Dick Mcgaw, the Irish crystallographer, who along with her colleagues systematically studied the structure of $BaTiO_3$ [8] and determined symmetry and unit cell parameters [9].

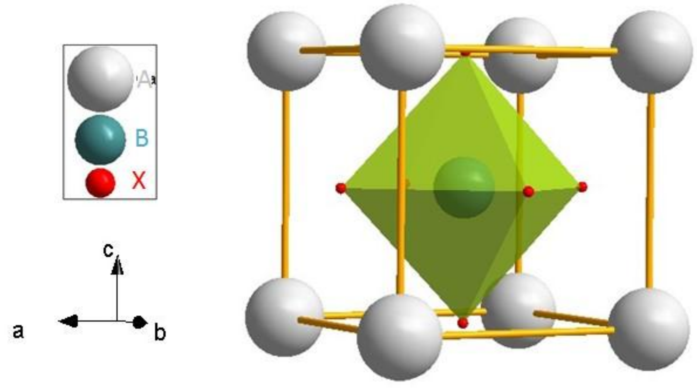

Figure 2. The 3D structure of ideal perovskite. Grey: A, Green: B, Red: X

As a matter of fact, there are many ways of presenting the structure of perovskite with A-, B-, and X- cell setting (referring to A-, B-, and X-site atom situated at the origin of the unit cell, respectively). The structure of perovskite is shown in Figure 2 (A-cell setting), the ideal structure of which is cubic with the space group of Pm-3m. As can be seen from Figure 2, in the structure, (the grey) A cation accommodates the eight corners of the unit cell and B is located in the center of the structure (the green one), while the X cation is situated on the face-centered position (the red one), which is a bridging point, linking two BX_6 octahedra. Their equivalent relative coordinates of the atoms are detailed in Table 1, the size of the X atom ought to be as large as that of A atom. Thus, in the finite 3D structure, it is a network of corner-linked octahedra, with the small cation filling the octahedral holes and the large cation filling the dodecahedral holes.

Table 1. Atomic positions in cubic pervoskite

Site	Wyckoff Position	Co-ordinates
A	1a	(0, 0, 0)
B	1b	(1/2, 1/2, 1/2)
X	3d	(1/2, 0, 0) (0, 1/2, 0) (0, 0, 1/2)

Until now, just a few compounds of ideal cubic structure were found. Based on the known compounds of perovskite, Mcgaw and her colleagues pointed out that ion size difference between A and B atoms may lead to distorted structures [10]. Years earlier, Goldschmidt, at the University of Oslo, introduced the tolerance factor "t", which is an indicator for the stability and distortion of crystal structures [11], and this pioneering work provided a basis for the further exploration of the structure of the perovskite family.

$$t = \frac{r_{A+X}}{\sqrt{2} r_{B+X}} \qquad \textbf{Equation 1}$$

where, r_{A+X} is the sum of the A and X ionic radii

r_{B+X} is the sum of the B and X ionic radii

Note that the Equation 1 is applicable at certain temperature and pressure to the empirical ionic radii and the limiting values for the tolerance factor have been determined by experiment. In most cases, perovskite type structures are distorted from the ideal cubic symmetry [12].

Since perovskites are not truly ionic compounds and the *t* values also depend on what values are taken for the ionic radii, the tolerance factor is only a rough estimate [13]. The tolerance factor and its distorted structure and examples are briefly illustrated in Table 2, it should be pointed out that such an analysis works better for 2+, 4+ perovskites than for the 3+, 3+ perovskites [14].

Table 2. Tolerance factor and its structure and examples [1, 15]

Tolerance factor	Possible structure	Examples
> 1	Hexagonal/rhombohedral	$BaFeO_3$
0.95 ~ 1.0	Cubic	$BaTiO_3$/$CaTiO_3$
0.75 ~ 0.9	Orthorhombic	$GdFeO_3$
< 0.75	Other structures	Ilmenite, $FeTiO_3$

In general, *t* is unity for ideal structure, however, many compounds have been found to adopt perovskite structure of lower symmetry for the value $0.75 < t < 1.13$ (this limiting value varies). It is noticeable that this value is not applicable for every case, e.g. $MgTiO_3$ with $t = 0.81$ as reported, shows ilmenite type structure for which the value of the A site ion is smaller than ideal, and the TiO_6 octahedra will tilt in order to fill space [1].

If tolerance factor less than 0.9, the B-X bonds are under a compressive strain causing the BX_6 octahedron to rotate, tilt or expand, in order to adopt an orthorhombic type structure (e.g. $PbZrO_3$, $CaFeO_{3-x}$). A series of notation developed by Glazer [16] to describe octahedral tilting distortions in perovskite has become popular. The Glazer notation is used to specifying the rotations of the octahedral about each of the three Cartesian axes [17].

If the t-value drops below 0.75, the compound can adopt a hexagonal ilmenite type structure for A and B ion have the similar radii. e.g. $FeTiO_3$ ($t = 0.723$, where $R_{Fe^{2+}} = 0.76$ Å, $R_{Ti^{4+}} = 0.68$ Å, $R_{O^{2-}} = 1.40$ Å) adopts the ilmenite type structure at low pressures [18]. This compound is an extremely distorted perovskite derived from archetypal structure and then is not a stable perovskite type structure because of extensive polyhedral rotation [1].

On the basis of the tolerance factor v, if t is larger than 1(usually1 $< t <$ 1.13), the BX_6 octahedra are stretched from B-X bond lengths, making the B site cations distort to create spaces for the B cations to move from the center, thereby resulting in hexagonal/rhombohedral type structure. e.g. $BaFeO_3$, $PbTiO_3$ [19].

The distortions of perovskite type structures are not only determined by the value t, but also influenced by the degree of covalency, metal-metal interaction, Jahn-Teller distortion and the lone pairs on the A cations [1]. It is rare that the distortion can be assigned to a single effect, in other words, several factors interact on the space group and structure adopted [1]. $BaTiO_3$, widely used in the Multi-Layer Ceramic Capacitors (MLCCs) due to its excellent dielectricity, is such a good example for which has five phase existing, hexagonal, cubic, tetragonal, orthorhombic, and rhombohedral from high to low temperatures [20, 21].

In addition, such structural deformations in the perovskite type compounds may give an enlargement of the cubic cells to the presence of super ones [22]. These distortions have some specific effects on the properties, especially on the magnetic property. The spin alignment of magnetic cations and its ordering would be influenced by the Jahn-Teller (JT) deformations, charge disproportionation (CD) with charge ordering (CO) [15, 17].

1.2 Perovskite related structures

There exists a large number of structures that are related to the perovskite type, due to the compositional versatility of the $ABX_{3-\delta}$ structures. These related perovskite phases range from anti-/ hybrid perovskites to intergrowth of perovskites.

Since the classification to the related perovskite type structures is out of the main aim of this thesis, only some examples are sorted into different groups with similarity.

1.2.1 Simple related perovskites

Here, some examples are given to demonstrate the simple perovskite phases according to textbook [1].

- Briefly, $A^{1+}B^{5+}O_3$, $A^{2+}B^{4+}O_3$ and $A^{3+}B^{3+}O_3$ are the simple examples of perovskite type, while $A(B'_{1-x}B''_x)O_3$, $(A'_{1-x}A''_x)BO_3$, $(A'_{1-x}A''_x)(B'_{1-y}B''_y)O_3$ are the complicated ones, i.e. representing solid solution derivatives.
- **BAX_3** inverse perovskite: this kind of structure contains Li^+ ion and alkaline earth elements, $EuLiH_3$ and $BaLiH_3$ were the first discovered ones, in this kind of structure, Li^+ is located at the center of LiF_6 polyhedron.
- Anti-perovskite structure, **A_3BX** or **XBA_3** perovskite inversely with the general composition ABX_3 where the anion occupies the center of the octahedra, Na_3OCl [23], Ga_3GeO [24] etc. belong to such kind of structures.
- **AB_3X** or **AXB_3** Anti-perovskite: this structure of which can be regarded as the derivatives of $AuCu_3$, the network links by sharing the Cu_6 octahedrals while the Au locates in the cubo-octahedral holes, so this compound can be written as □$AuCu_3$, where □ donates the A site. E.g $GaSc_3C$ belongs to this structure.

1.2.2 Layered perovskite related compounds

There exist a large number of perovskite-related compounds beyond the distorted derivatives described above. If perovskite structure elements are separated by rock salt layer, superstructures will be formed. The compounds of this type structure are called layered perovskites. Layered perovskites consist of infinite 2D slabs of ABX_3 type structure which are separated by certain motif. The two differentiating characteristics for the layered perovskites are ***1)*** the motif separating the layers, and ***2)*** the offsetting of the layers from each other. In this case, three widely studied structure families are found and usually named after their first researchers.

The general formula of these three phases is as follows:

- The Ruddlesden–Popper phase $(A'X)(ABX_3)_n$
- The Dion–Jacobson phase $A'(A_{n-1}B_nX_{3n+1})$
- The Aurivillius phase $(A'_2X_2)(A_{n-1}B_nX_{3n+1})$

Where n indicates the size of the 2D slabs, e.g. n = 1 means the slab is one BX_6 octahedron thick. n = 2 presents two BX_6 octahedral thick, etc.

Figure 3 shows the structure (n = 3) for each of these three variants.

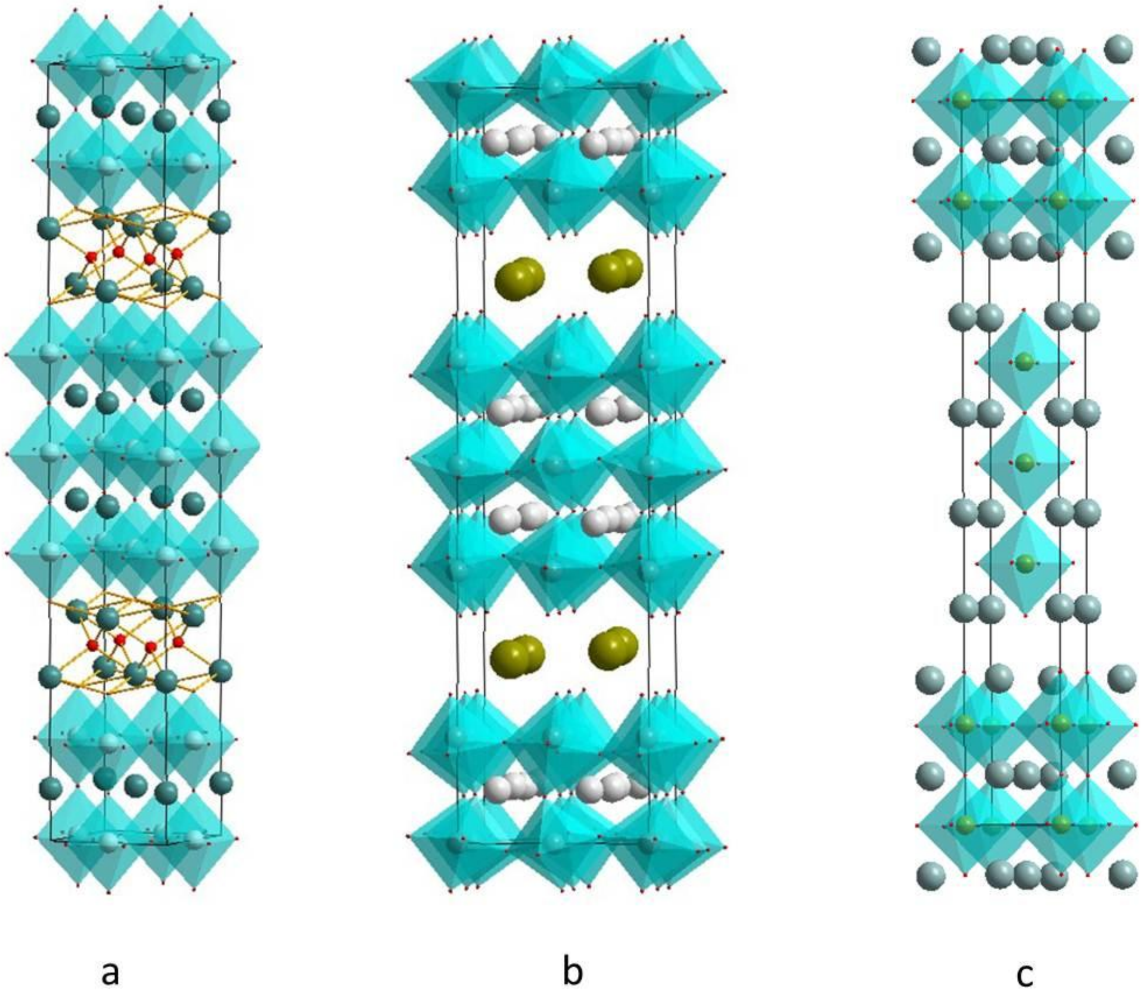

Figure 3. Schematic crystal structures of layered perovskites, n = 3 [25]. (a) Ruddlesden–Popper phase. (b) Dion–Jacobson phase. (c) Aurivillius phase.

1.2.2.1 Aurivillius type of compounds

The $(Bi_2)(A_{n-1}B_nX_{3n+3})$ series of related perovskites named after Aurivillius who first introduced this structure in 1949 for discovering $Bi_4Ti_3O_{12}$ (n = 3) [26]. The compounds are structurally related to Dion-Jacobson (DJ) and Ruddlesden-Popper (RP) phases and to emphasize the relationship the formula is better to expressed as $(Bi_2O_2)(A_{n-1}B_nX_{3n+1})$, where n indicates the perovskite-like slabs in thickness with (Bi_2O_2) sheet occupying the inter-slab regions [1]. Simple and coupled cation substitution in this structure might involve at: the B-site by Ti, Nb, Ta, Fe, W, Mo, Ga and Cr, the cubooctahedral site of the perovskite slab by Bi, Ba, Sr, K etc. The replacement of anion by halogens is synthesized to a limited extent.

Numerous Aurivillius phases (n = 1~8) have layers defined by Bi_2O_2, and substitution of Bi by Pb, Tl, Sb and Sn in the separating layer has been reported [27].

1.2.2.2 Dion–Jacobson type of compounds

In the Dion-Jacobson phase, with general formula of $A'(A_{n-1}B_nX_{3n+1})$, where the $(A_{n-1}B_nX_{3n+1})$ term represents the common unit of 2D perovskite slabs. A usually accommodates alkaline earth or rear earth elements and B site is typically occupied by some transition metals. This type of superstructure, which consists of n perovskite-like layers with a monovalent cation A' occupying the interlayer space, was firstly discovered by Dion [28] and then Jacobson [29] developed its range by introducing the number "n" of the stacked perovskite unit cells. Compouds with n values of 2 to 7 have been synthesized [30]. This type compounds have been intensively studied because of their interesting ionic, ion-exchange, intercalation and luminescence properties.

1.2.2.3 Ruddlesden–Popper type of compounds

Ruddlesden and Popper investigated the structure of $Sr_3Ti_2O_7$ (n = 2) [31] and $Sr_4Ti_3O_{10}$ (n = 3) [32] in 1958, although the n = 1 of this series (K_2NiF_4 [33]) has been reported years earlier.

Similar to Aurivillius phases, Ruddlesden-Popper (RP) phase has the separating rock salt layer with A/B ration of 1:1. However in RP phases, the unity A/B ratio is preserved within the perovskite slabs, the total cation to anion ratio is smaller and its general formula is $A_{n+1}B_nX_{3n+1}$. In this formula, "n" indicates the size of the 2D corner-sharing slabs that are stacked along c axis. For these phases, A and B are the cations, the separating motif is a rock salt layer of AX and the "n" perovskite slabs $(ABX_3)_n$ are offset by a (1/2, 1/2) translation along a and b axis. It is possible, and perhaps another way to think Ruddlesden Popper phases as $A_2(A_{n-1}B_nO_{3n+1})$, where the separating motif is a layer of A_2 and the perovskite slabs $(A_{n-1}B_nX_{3n+1})$ are also offset by a (1/2, 1/2) displacement.

For the RP phases, the A site contains usually alkaline earth or lanthanide, Y, Bi etc…whereas 3d and 4d transition metal elements accommodate on the B site, some elements like group XIII and XIV and even carbonates have been reported. As displayed in Figure 4, it illustrates the crystal structure of RP (n = 1, 2, 3, respectively) phases in comparison with the ideal cubic perovskite, which can be regarded as the $RP\infty$ phase.

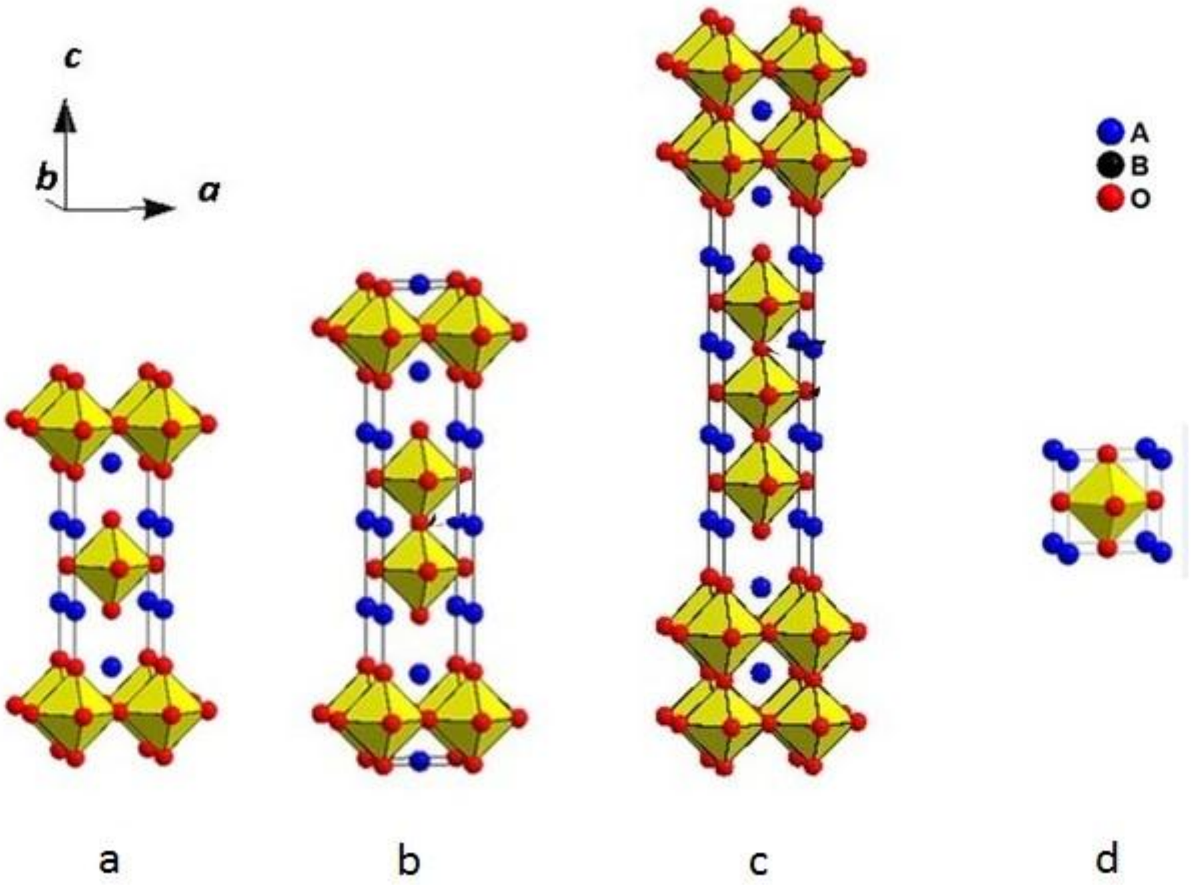

Figure 4. Crystal structure of $A_{n+1}B_nO_{3n+1}$ Ruddlesden-Popper phase oxide [34]. (a)n = 1, RP1 phase, e.g. Sr_2TiO_4. (b)n = 2, RP2 phase, e.g. $Sr_3Ti_2O_7$. (c) n = 3, RP3 phase, e.g. $Sr_4Ti_3O_{10}$. (d) n = ∞, ideal perovskite, e.g. $SrTiO_3$.

Since the first discovery of RP phases, a very large number of RP compounds have been synthesized. Until now, most of RP phases are for n = 1, 2, 3, but also some of higher ordering number (n = 4, 5, 6 ……) [35] have been reported.

These three categories of RP-phases exhibit higher flexibility in terms of oxygen content and cation composition. As such they are promising candidates for studying the effect of cation composition and oxygen content on various physical properties.

1.3 Defective perovskites

The ideal crystalline solids repeat the specific position of atoms or molecules in 3D structures at fixed distances, which are determined by the unit cell parameters. As a matter of fact, it is impossible to find a perfect crystal theoretically above 0 K, which means that the arrangement of atoms or molecules is not in perfect repeatment, and then it comes to the term “defect”.

As stars make our universe more beautiful, defects are the star to make the “whole materials” have fantastic properties. Many of them, such as electronic or ionic conductivity, the color, the luminescence, and the magnetic susceptibility may be determined to larger or less extent by the presence of defects [36].

1.3.1 Background of defects

In a wide sense, defects can be either stoichiometric or non-stoichiometric. The former one means the defect in the crystal lattice which does not change or have any effect on the molecular formula of the crystal while non-stoichiometric defects affects the ratio of cation to anion which then becomes different from that indicated by the ideal chemical formula.

According to the dimensionality of the defects, they can be classified as point defects, line defects, planar defects as well as bulk/volume defects.

Point defects can only occur at or around a single position in a structure, which can be a vacancy, an electron, an interstitial atom or a substitutional atom, typically these defects involves a few atoms or vacancies as a “single point”. Kröger and Vink developed a notation to describe the charge, electron, vacancy and lattice point for point defect species in a crystal [36] as shown in Table 3.

Table 3. Kröger-Vink notation

Defects	Notation
Defect electron	e'
Electron hole	$h^{\cdot}$
Hole/vacancy	V
Interstitial site	i
Neutral charge	×
Elements defect	Element itself

By using the above notations, it is particularly useful to describing various defect reactions in crystals. Additionally, one more notation should be defined:

$$M_S^C$$

where, M corresponds to the species, which can be atoms, vacancies, electrons, or electron holes; S illustrates the lattice site that the species occupies; C is the electronic charge of the species relative to the site that occupies.

As can be imagined, a number of zero dimensional point defects can compose 1D line defects and 2D planar defects, further 3D defects maybe formed. All the above-mentioned defects may exist simultaneously in any crystal compounds.

1.3.2 Thermodynamics of defects

In thermodynamics, the existence of defects with a specific concentration will result in an increase of enthalpy and a reduction of Gibbs free energy, in other words, it take energy to create defects in crystals.

The thermodynamics of defects are closely related to the thermodynamic of basic chemical reactions and can be explained through Gibbs free energy equation:

$$\Delta G = \Delta H - T\Delta S \qquad \text{Equation 2}$$

In a chemical reaction, the energy of forming defects in solids can be treated in a statistical way. As specified in defect chemistry, there are two types of entropy, ΔS_{vib} and ΔS_{conf}, which describles the vibrational and configurational entropy respectively. If n_v mole vacancies are formed in a solid, the total change of the enthalpy is $n_v\Delta H$. Thus, the total Gibbs energy of formation numbers of n_v new sites is:

$$\Delta G = n_v(\Delta H - T\Delta S_{vib}) - T\Delta S_{conf} \qquad \text{Equation 3}$$

where the total configurational entropy can be calculated by thermodynamic probability W:

$$\Delta S_{conf} = klnW \qquad \text{Equation 4}$$

W describes the n_v vacancies distributing on all the possible sites of $\mathrm{N} + n_v$, in the mathematical way, which gives:

$$\mathbf{W} = \frac{(N+n_v)!}{N!n_v!} \qquad \textbf{Equation 5}$$

By using Stirling's approximation ($lnx! = xlnx - x$ for $x \gg 1$), Equation 4 can be simplified as:

$$\Delta S_{conf} = k\left(Nln\frac{N+n_v}{N} + n_v\frac{N+n_v}{n_v}\right) \qquad \textbf{Equation 6}$$

At equilibrium, the derivative of Equation 3 ΔG by n_v should be zero, combining Equations 5 and 6 gives:

$$\frac{\partial \Delta G}{\partial n_v} = (\Delta H - T\Delta S_{vib}) + kTln\frac{n_v}{n_v+N} = 0 \qquad \textbf{Equation 7}$$

The term $\frac{n_v}{n_v+N}$, expressing the concentration of the vacancies in the crystal lattice, is as a function of the enthalpy change, the vibrational entropy and temperature. Thus the expression of the vacancy concentration gives:

$$K_v = \frac{n_v}{n_v+N} = \exp(\frac{\Delta S_{vib}T - \Delta H}{kT}) \qquad \textbf{Equation 8}$$

K_v is the equilibrium constant in the vacancy formation reaction.

1.3.3 Defect situations in perovskite type compounds

Solid solution of aliovalent impurities and deviations from stoichiometry lead to the presence of point defects in crystalline inorganic compounds [37]. As a compound of perovskite structure, besides the radii requirements, another condition should also be fulfilled is electroneutrality [22], e.g. the sum of charge of A and B equals to the total charge of X anion in perovskite, this can be obtained in, such as $A^{a+}B^{b+}O_3$ (a + b = 6) as presented in section 1.2. Because of the large accommodation and substitution of the anions, a little bit more or less partial substitution of A and B site ion are allowed, which lead to a deficiency in the compound but preserving the perovskite structure. Generally speaking, nonstoichometry in perovkites can arise from A-/B-cation sites deficiency or O-anion site deficiency and excess. This kind of defects is comprehensively discussed in several reviews[38] and books [39].

In most cases, the oxygen defects are more common than that of cationic ones. For the oxygen defects in provskite structure, the oxygen vacancies are nonstoichometry is more common than the oxygen excess nonstoichometry for the latter one would introduce interstitial oxygen on the A-/B- sites in this structure is thermodynamically unfavorable. Some compounds have oxygen excess in the structure, for instance $LaMnO_{3+\delta}$, which is well exemplified. Tofield et al. [40] reported that a proved composition of $LaMnO_{3.12}$, the Neutron diffraction shows that the oxygen do not enter the A-/B- sites, while the O-sublattice remains perfect. Thus the real chemical formula can be written as $La_{0.94}\square_{0.06}Mn_{0.98}\square_{0.02}O_3$ (where □ indicates cation vacancies). The interstitial oxygen atoms enter into RP3 phase e.g. $La_4Co_3O_{10}$ within LaO rock salt layer [41, 42].

In many circumstances, the oxygen vacancies can be found in perovskite and related perovskite type phases. Bringley et al. [43] has synthesized a stable $LaCuO_{3-\delta}$ over a large oxygen vacancy range of $0 < \delta < 0.5$. In RP oxides, an oxygen deficiency was found in many cases. Lee et al. [44] reported that the $LaSr_3Fe_3O_{10-\delta}$ sample is able to adopt a large amount of oxygen vacancies (δ~0.8 per formula unit) in central perovskite slabs of the crystal structure without any degradation.

Cation nonstoichometry can be achieved by oxygen excess, which means that the structure is in oxygen deficiency [7]. B-site vacancies are not common, for which are not thermodynamically favored because of the small size and large charge of B ion. These vacancies are available among h-h (hexagonal stacking layers of AO_3) layers, where the BO_6 octahedra share faces. On the contrary, A-site vacancies are exhibited in some perovskites, where large A ion can be partially missing for the BO_3 that forms a stable network. The RO_3 type structure is the limiting case of A-site vacancies.

1.4 Possible applications

Since perovskite structure can accommodate a wide variety of ions, this type compounds have various technologically applicable properties, dependent on the composition, defects and structural distortions. This makes them to be widely used in diverse fields, such as dielectricity, ionic conductivity, superconductivity, magnetism, luminescence, photocatalys, catalysis etc.

RP-type oxides, exhibiting ion conduction, electronic conduction and catalysis, are very promising for the use in many electrochemical applications. For instance, they are currently used as cathode materials for Solid Oxide Fuel Cells (SOFCs) [45] and oxygen separation membrane [46, 47]. What's more, these RP family compounds have been extensively investigated for the new potential applications such as high temperature superconductivity (HTS) [48] or colossal magnetoresistance (CMR) [49].

In the following paragraphs, one possible application of this kind of RP3 phase oxide will be demonstrated.

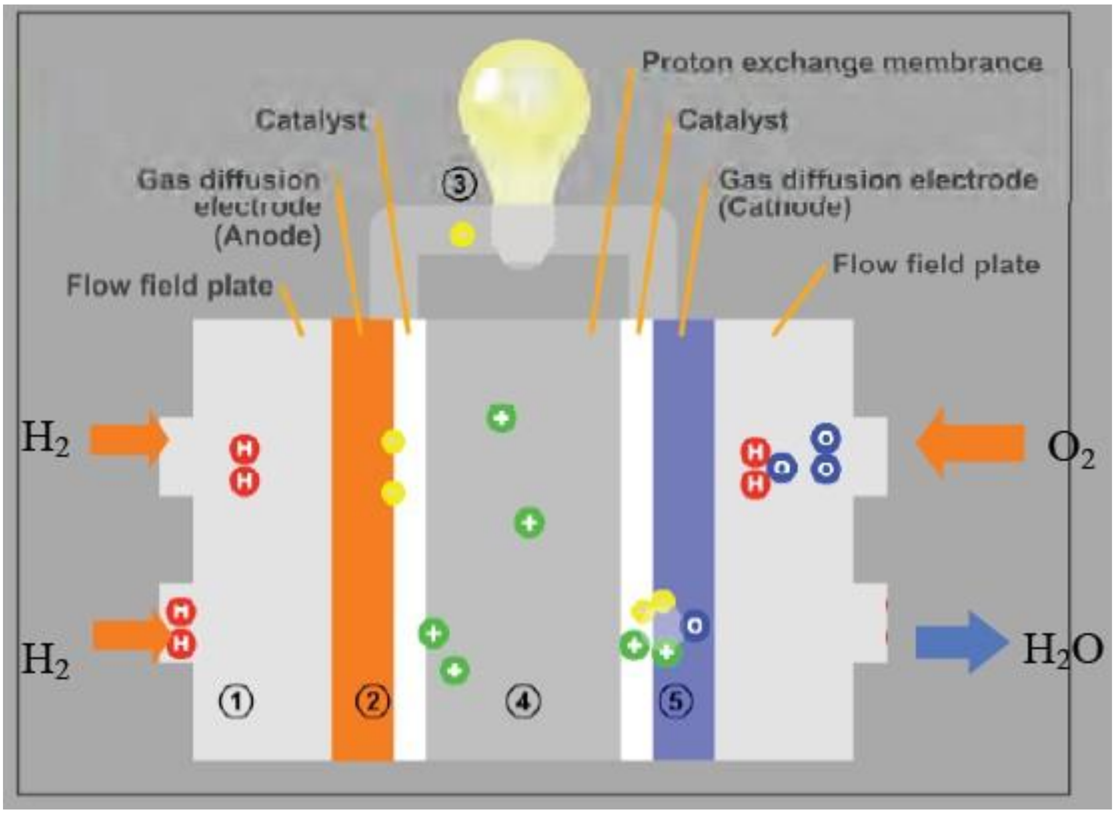

Figure 5. Schematic of Hydrogen-Oxygen Fuel Cells [50]

Figure 5 demonstrates the schematic of the Hydrogen-Oxygen Fuel Cell, the procedure of which is as follows:

- Hydrogen gas is splited into protons and electrons on the anode side after it goes through the channel of the flow field plate.
- The electrons travel through the external circuit to the cathode, at the same time, and the protons travel through the proton exchange membrane and arrive at the cathode, forming the electrical current of the cell.
- The hydrogen protons and electrons are caused by the catalyst at the cathode side to combine with oxygen to form water vapor.

The RP series of intergrowth oxides are found to be able to demonstrate this role for they are good Mixed Ionic and Electronic conductors (MIECs), such as high electronic and oxide-ion conductivities and good structural and chemical stabilities at intermediate operating temperatures (500 ^oC - 800 ^oC) and under low or high oxygen partial pressures. In addition to the requirements to the cathode materials function as the cathode site for the electrochemical reduction of oxygen in SOFCs were comprehensively documented [51, 52]. The MIEC oxides for SOFCs, including the series of RP phase oxides, have been fully investigated in a few reviews [34, 44, 51, 53, 54] etc.

1.5 Literature review

Since Ruddlesden and Popper discovered the RP materials, the Ln-Sr-M-O (M = Fe, Co, Mn, Al…) systems have attracted increasing attentions. However, RP3 phases are less investigated, compared with RP1 and RP2 compounds. Thanks to many research groups all over the world, the results (structure, electric and magnetic properties) and possible applications of this series of interesting oxide have been studied using both classical and new methods of synthesis and characterization. These studies have been carried out independently by each group with certain aspects of their interests.

After a comprehensive search of the related literatures, a short summary of the earlier study of Ln-Sr-M-O and its related oxygen deficient oxides relating to my investigation will be made. This section focuses on the crystal structures, physical properties with respect to the materials in this work.

1.5.1 The structure of $LnSr_3Fe_3O_{10-\delta}$

Undistorted $A_4B_3O_{10}$ Ruddlesden-Popper compounds with n = 3 adopt the space group of aristotype *I*4/mmm, e.g. $Sr_4Fe_3O_{10}$ [32], as the parent structure, is such an example. Numerous structures have been derived from this RP3 patent compounds by the replacement of Ti with lower valent transition metals (e.g. Fe, Co) and charge compensation by higher valent ions on the A site. Thus, this derived series of compounds with n = 3 have not been extensively studied. Brisi et al. [55] investigated the Sr-Fe-O system and reported an oxygen deficient $Sr_4Fe_3O_{10-\delta}$, which has the oxygen vacancies to charge compensation for substitution of Ti^{4+} by lower variable valence Fe ion.

Lee et al. [56] has investigated the crystal chemistry of $LaSr_3(Fe,Al)_3O_{10-\delta}$ with $\delta < 0.8$ in the phase $LaSr_3Fe_3O_{10-\delta}$.

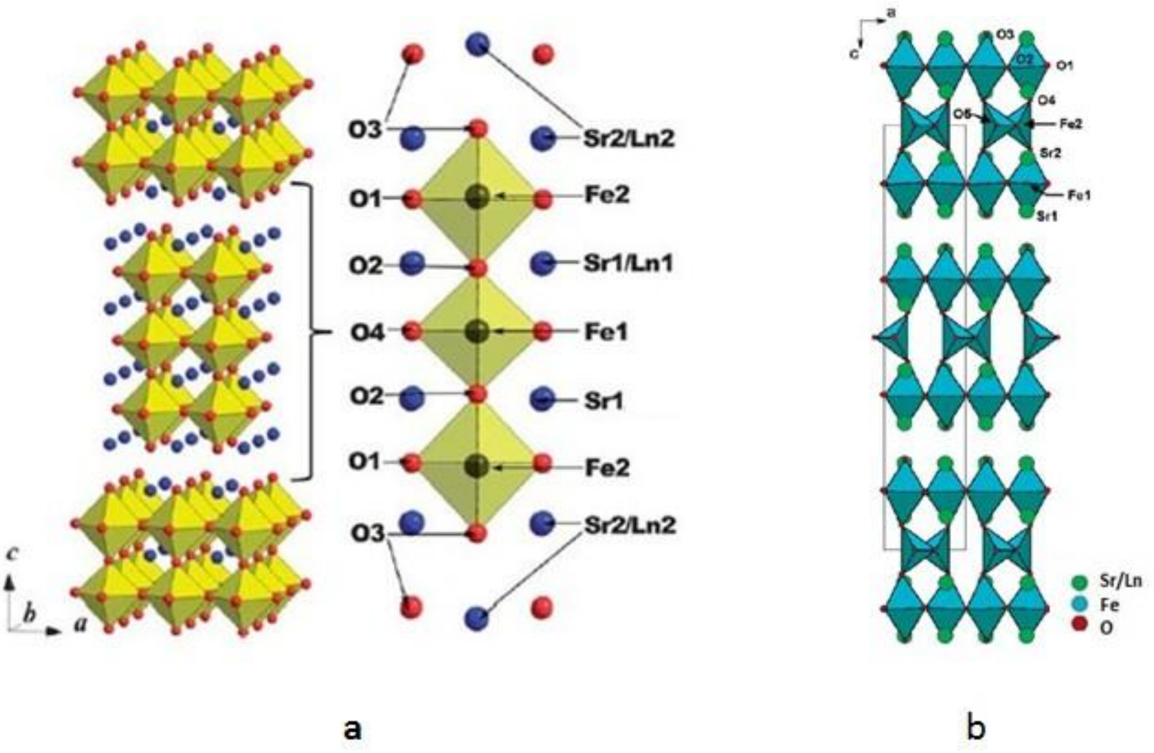

Figure 6. Crystal structure and their atom sites in the structure for $LnSr_3Fe_3O_{10-\delta}$ series (Ln = La, Nd). (a) Crystal structure of $LaSr_3Fe_3O_{10-\delta}$ ($\delta < 0.8$), the oxygen atoms at the front side of the octahedral sites (O1 and O4) are omitted for simplicity in the expanded view [53]. (b) Crystal structure and their atom sites in the structure of $NdSr_3Fe_3O_9$ [57].

The crystal structure of $LaSr_3Fe_3O_{10-\delta}$, as illustrated in Figure 6, consists of a triple layer of La/Sr-Fe-O octahedral separated by La/Sr-O layers. The sample is able to adopt a large amount of oxygen vacancies ($0.1 < \delta < 0.8$) in the lattice without any structural degradation [56]. From the Rietveld refinement of neutron powder diffraction in addition to the X-ray study, the oxygen vacancies have been found to be localized on the central FeO_6 octahedral with three consecutive FeO_6 octahedral along the c axis, corresponding to the O2 and O4 sites in Figure 6.a. With the decreasing oxygen stoichiometry, the value of c-axis parameter shows a linear increase from 28.04 Å for the phase $LaSr_3Fe_3O_{9.9}$ to 28.52 Å for the phase containing 9.2 oxygen atoms, while a and b parameter nearly stay stable at 3.87 Å [56]. The atomic coordinates for this RP3 phase ($LaSr_3Fe_3O_{9.9}$) are illustrated in Table 4.

Table 4. Atomic coordinates for $LaSr_3Fe_3O_{10-\delta}$ refinement

Site	Multiplicity	Wyckoff	Atom	OX	X	Y	Z	Occupancy
A1	4	e	La	La^{+3}	0	0	0.569	0.25
A1	4	e	Sr	Sr^{+2}	0	0	0.569	0.75
A2	4	e	La	La^{+3}	0	0	0.701	0.25
A2	4	e	Sr	Sr^{+2}	0	0	0.701	0.75
B1	2	a	Fe	$Fe^{+3.67}$	0	0	0	1
B2	4	e	Fe	$Fe^{+3.67}$	0	0	0.139	1
O1	8	g	O	O^{-2}	0	0.5	0.138	1
O2	4	e	O	O^{-2}	0	0	0.069	1
O3	4	e	O	O^{-2}	0	0	0.211	1
O4	4	c	O	O^{-2}	0	0.5	0	0.97

Moreover, in this series, the possibility of higher oxygen deficiency was demonstrated in $NdSr_3Fe_3O_9$ [57]. In this compound, the atomic coordinates (see Table 5) is illustrated as *Bbmm* space group with the unit cell parameters a = 5.54 Å, b = 5.50 Å and c = 28.81 Å respectively.

Table 5. Atomic coordinates for $NdSr_3Fe_3O_9$

Site	Multiplicity	Wyckoff	Atom	OX	X	Y	Z	Occupancy
A1	8	g	Nd	Nd^{+3}	-0.253	0.75	0.203	0.25
A1	8	g	Sr	Sr^{+2}	-0.253	0.75	0.203	0.75
A2	8	g	Nd	Nd^{+3}	-0.242	0.75	0.078	0.25
A2	8	g	Sr	Sr^{+2}	-0.242	0.75	0.078	0.75
B1	8	g	Fe	Fe^{+3}	0.251	0.75	0.145	1
B2	4	e	Fe	Fe^{+3}	0.306	0.75	0	1
O1	8	e	O	O^{-2}	0	0.5	0.139	1
O2	8	e	O	O^{-2}	0.5	1	0.135	1
O3	8	g	O	O^{-2}	0.258	0.75	0.214	1
O4	8	g	O	O^{-2}	0.213	0.75	0.058	1
O5	8	c	O	O^{-2}	0.378	0.127	0	0.5

As shown in Figure 6.b, the crystal structure can be described as an intergrowth of a brownmillerite-type layer ($Sr_2Fe_2O_5$) and a K_2NiF_4-type layer ($NdSrFe_3O_4$) along the c-axis direction. The resulting Fe_3O_9 framework is built of a central sheet of parallel chains of FeO_4 tetrahedral and parallel rows of oxygen running along b axis. In this way, this compound can be considered as an ordered oxygen-deficient RP3 phase with the formula of $NdSr_3Fe_3O_9$□, where □ represents the one oxygen vacancies per formula unit. This tetrahedral sheet is sandwiched between two octahedral FeO_3 perovskite-like slabs. Along c axis, two successive Fe_3O_9 blocks are offset by (1/2, 1/2) translation in the direction of a and b axis as viewed in the RP3 phase.

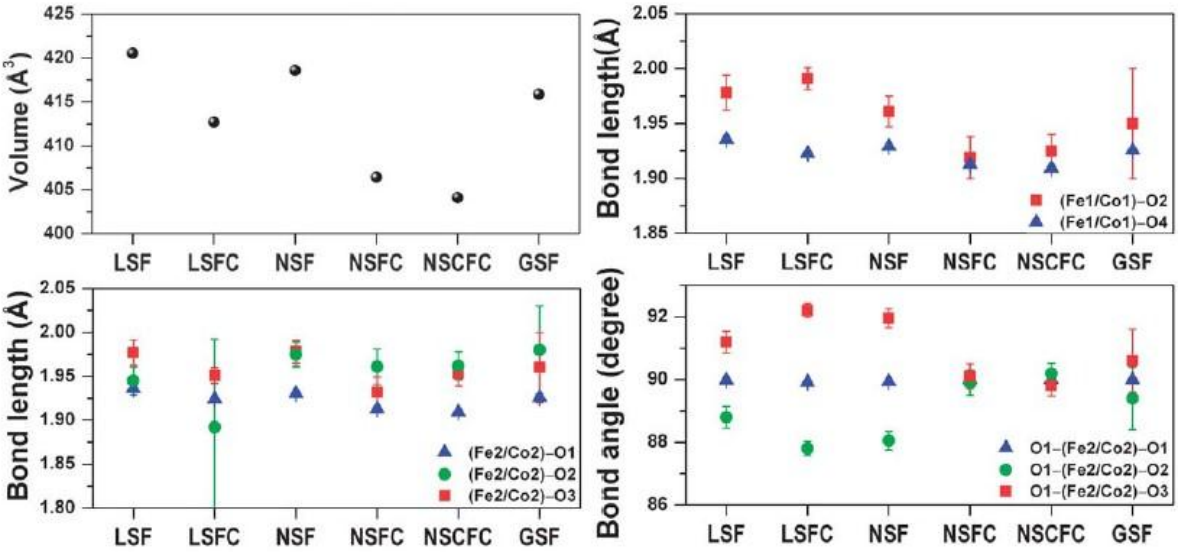

Figure 7. Variations of the unit cell volumes, Fe-O bond length and O-(Fe2/Co2)-O bond angles in the various $Ln(Sr,Ca)_3(Fe,Co)_3O_{10}$ phases [44]. $LaSr_3Fe_3O_{10}$ (LSF) and $NdSr_3Fe_3O_{10}$ (NSF).

Figure 7 was plotted with the (Fe,Co)-O bond lengths, calculated from the Rietveld refinement. The equatorial (Fe1/Co1)-O4 and (Fe2/Co2)-O1 bond lengths in the series show close values in the range of 1.91~1.94 Å. However, the apical (Fe, Co)1-O bond length is strongly influence by the different chemical compositions and oxygen stoichiometry of the sample [44].

1.5.2 The thermal investigation

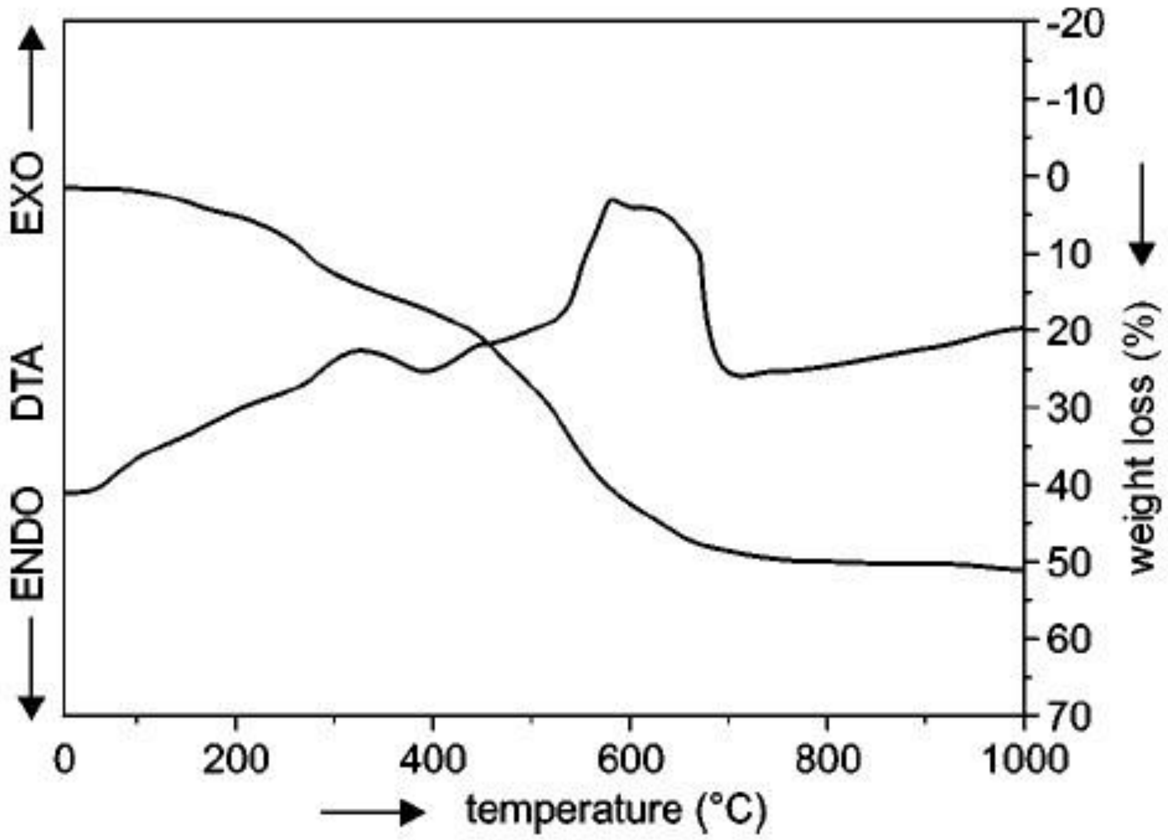

Figure 8. TG/DTA of the gels with nominal compositions $LaSr_3Fe_3O_{10}$ [58]

As displayed in Figure 8, Velinov et al. [58] presented the TG and DTA curves of the gel of the RP (La-Sr-Fe-O system with n = 1, 2, 3 using citric acid method) oxide. The measurement was conducted with 10°C/min in the temperature range 15 °C and 1000 °C after preheat treatment being dried at 200°C for 2h. The initial weight loss occurs at about 200 °C due to the removal of the water. A more significant loss of weight is observed after 300 °C due to a stepwise burning out of the organic matter in the gel. With the increasing temperature, a strong endothermic effect appears at around 700 °C mainly because of the formation of perovskite phase, no obvious weight loss and thermal effects in the sample were involved.

The thermogravimetric analysis of solid solution $LnSr_3M_3O_{10}$ (Ln = La, Nd, Gd; M = Fe, Co) is conducted under different atmosphere by several research groups, as displayed in Figure 9.

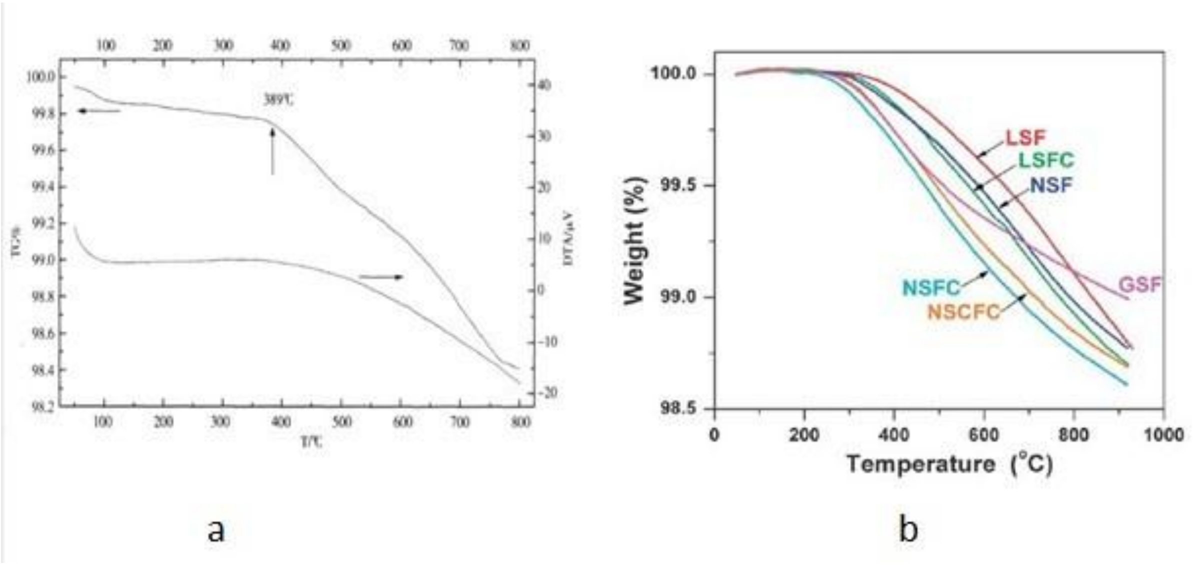

Figure 9. Thermal analysis of Ln-Sr-M-O (RP3) phase.(a)TG and DTA of $LaSr_3Fe_3O_{10-\delta}$ [59]. (b) TGA plots of $Ln(Sr,Ca)_3(Fe,Co)_3O_{10-\delta}$ 3°C/min from RT to 900°C, in air [44].

As shown in Figure 9, the thermal analysis of Ln-Sr-M-O RP3 compounds shows that the oxygen losses begin between 300°C to 400 °C upon heating and continue loss lattice oxygen at elevated temperatures, reaching different values at maximum temperature conducted.

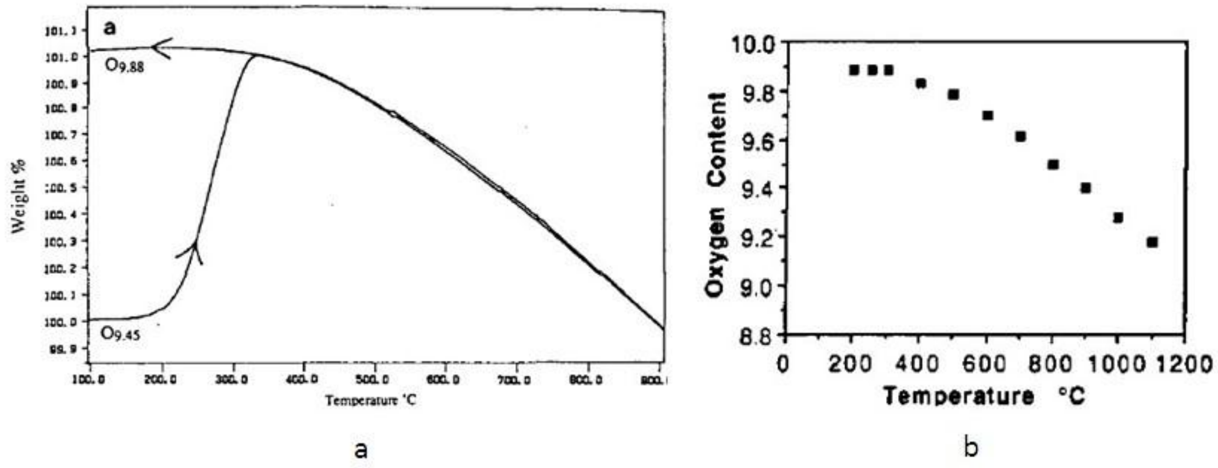

Figure 10. Oxygen content as a function of temperature [56]. (a) Plot of oxygen content of the sample calculated from the thermogravimetric data of $LaSr_3Fe_3O_{9.45}$ in air. (b) The variation of oxygen content with temperature for fully oxidized $LaSr_3Fe_3O_{10-\delta}$.

For oxygen deficient compound $LaSr_3Fe_3O_{9.45}$, as displayed in Figure 10.a, the thermogravimetric curves show that oxygen is reversibly lost and reintercalated upon heating and cooling. Lee et al. [56] in his article, reported the variations of oxygen stoichiometry in air as a function of temperature for $LaSr_3Fe_3O_{10-\delta}$. Figure 10.b shows the oxygen content per formula unit as a function of quenching temperature. The fully oxidized with a oxygen stoichiometry of $O_{9.9}$ and then cooled down to and kept at the temperature ranging from 500 ^{o}C to 1000 ^{o}C with a interval of 100 ^{o}C for 4 hours and then quenched into liquid N_2 immediately and directly.

Armstrong et al. [60] performed this series samples under different atmosphere, showing that all this series has larger oxygen deficiency in N_2 than that of air when the oxygen begin to loss upon heating, by calculating from the TGA data.

1.5.3 The topotactics involving in the $NdSr_3Fe_3O_{10-\delta}$ ($0 < \delta \leq 1.5$)

Stabilization is an important issue for any solid materials. From previous study, the RP phase oxides are somewhat unstable in presence of water, O_2 and CO_2. Some reviews are available to demonstrate this property.

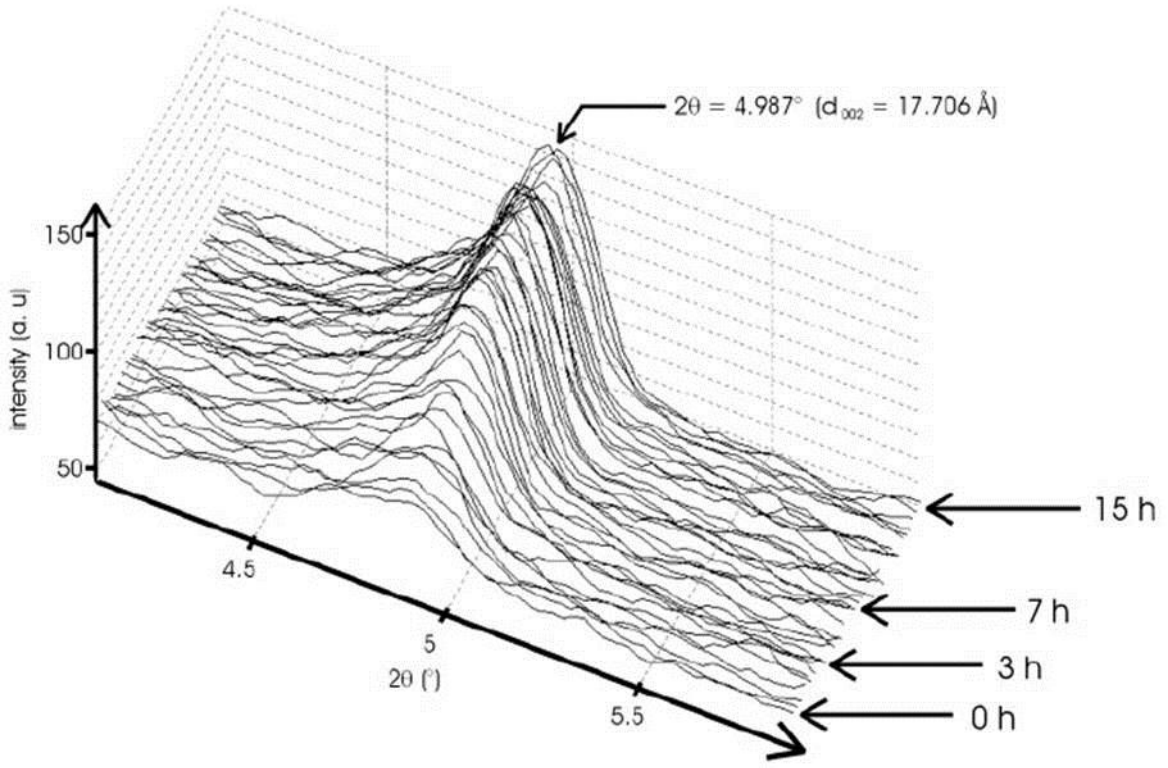

Figure 11. XRD of $NdSr_3Fe_3O_{8.5}$ in the air as a function of time [57]

Pelloquin et al. [57] synthesized Nd-Sr-Fe-O phase and obtained high oxygen deficient, RP3 ferrite, with nominal composition of $NdSr_3Fe_3O_{8.5}$. The XRD shows this reactivity is very quick as shown in Figure 11 by the growth of a peak at 2θ~5.5^{o}.

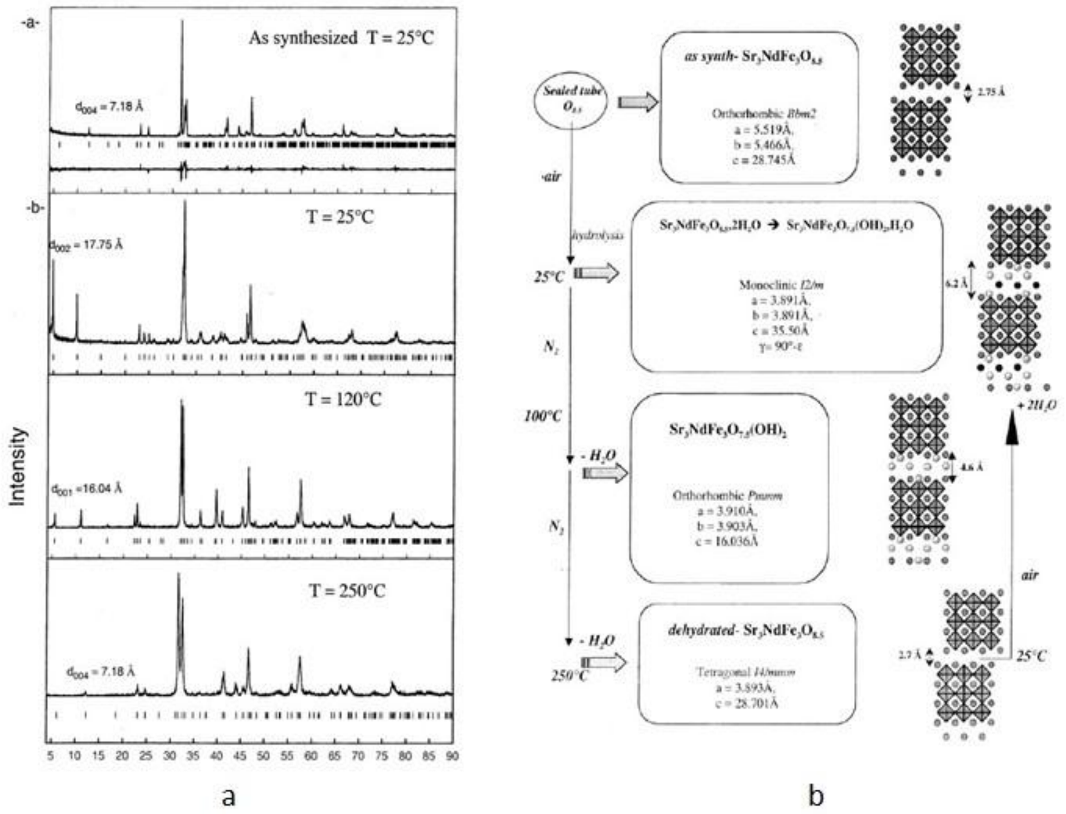

Figure 12. The different phases of the $NdSr_3Fe_3O_{8.5}$ dehydrooxylation mechanism involved [57]. (a) Experimental XRD pattern of different phases. (b) Structural mechanism and stacking mode of the different phases. Water molecules and hydroxyl groups are idealized as black and gray circles, respectively.

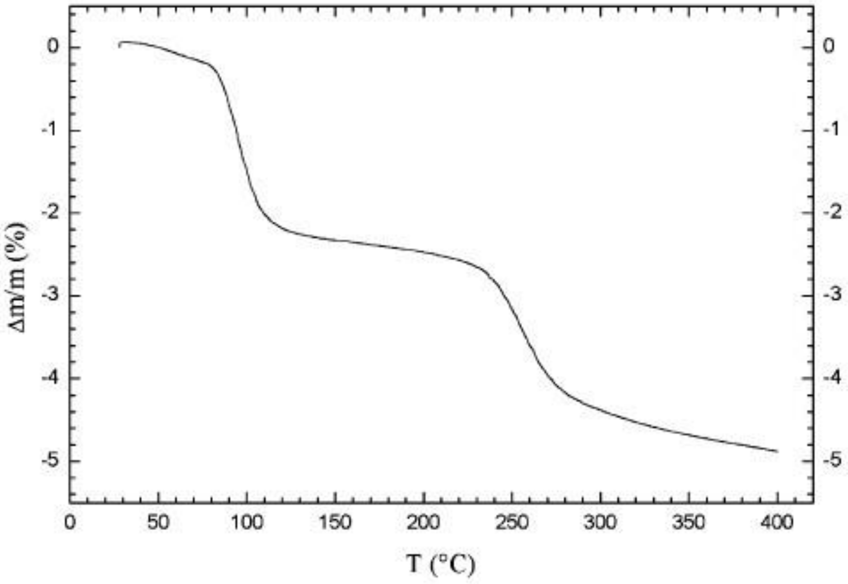

Figure 13. TGA pattern of the oxy-hydroxyl hydrate $NdSr_3Fe_3O_{7.5}(OH)_2·H_2O$ collected under nitrogen flow [57].

This highly oxygen deficient (n = 3) RP phase reacts at room temperature in the presences of humidity (H_2O) and transforms into a layered oxyhydroxide $NdSr_3Fe_3O_{7.5}(OH)_2 \cdot H_2O$, in which no carbonates have been found. The X-ray powder diffraction (as shown in Figure 12) and the thermogravimetric analysis (as displayed in Figure 13) show a second phase of which can be dehydrated topotactically by hearing to 250 °C, giving rise to first $NdSr_3Fe_3O_{7.5}(OH)_2$ at around 90 °C. Then followed by $NdSr_3Fe_3O_{8.5}$, a second water molecule departure at about 250 °C, suggesting that a dehydrooxylation mechanism is involved.

For the homologous series $Sr_{n+1}Fe_nO_{3n+1}$ RP phase oxide, Lehtimaki et al. [61] investigated their tendency to accept additional layers of water in their crystals. In the paper, it is revealed that the RP1, 2, 3 phase readily accommodate one or two layers of water between the adjacent SrO layers while $SrFeO_3$ remains intact in the presence of water because of lacking the SrO–SrO double layers. When increasing the layers, the water intercalation is found to decrease.

1.5.4 Electrical properties

There are many literatures reports demonstrating the electrical properties of the RP-series of compound.

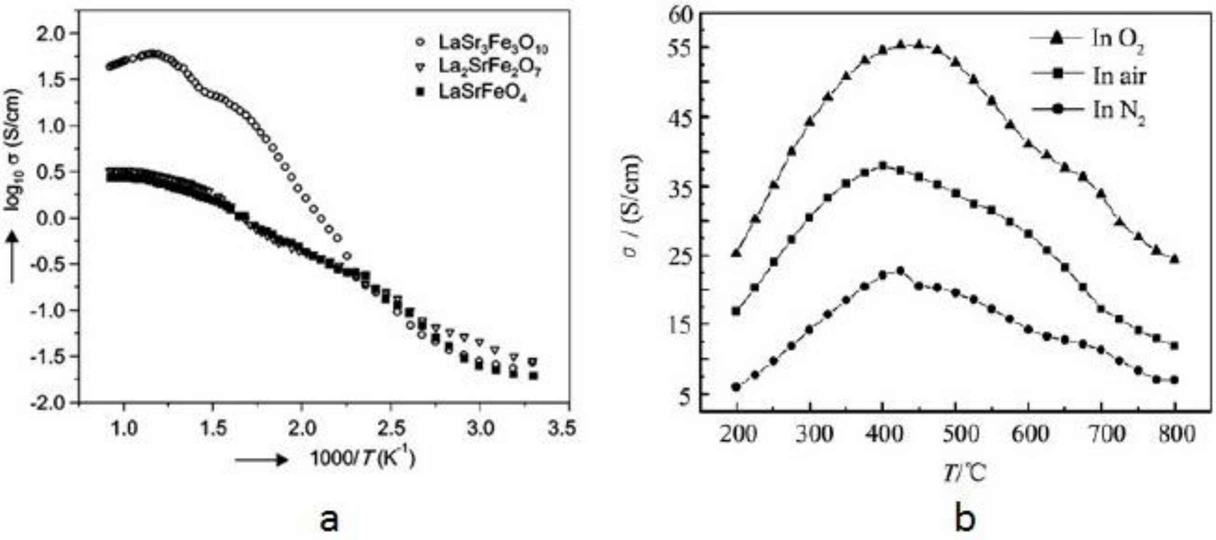

Figure 14. Temperature dependence of the total conductivity of $(La,Sr)_{n+1}Fe_nO3_{n+1}$ series. (a)Conductivity of $LaSrFeO_4$, $La_2SrFe_2O_7$ and $LaSr_3Fe_3O_{10}$ samples [58]. (b)Conductivity of $La_3SrFe_3O_{10-\delta}$ under different atmosphere.

Velinov et al. [58] measured the total conductivity of $(La,Sr)_{n+1}Fe_nO_{3n+1}$ (n = 1, 2, 3) as displayed in Figure 14.a. At the temperatures over 140 ^oC, it shows that the triple layered $LaSr_3Fe_3O_{10}$ perovskite, reaching its maximum of 58 S/m at 580 ^oC over the range 140 ^oC and 800 ^oC. The conductivity of triple layered phase is not only significantly higher than that of the single and double layered compounds, but also possess potentially applicable mixed ion conductivity and catalytic activity. The macrostructure of these compounds was investigated by Scanning Electric Microscopy (SEM), a uniform distribution and size of the grains and pores was observed in $LaSrFeO_4$ and $La_3SrFe_3O_{10}$ compounds.

As displayed in Figure 14.b, the temperature dependent conductivity of RP3 phase oxide ($LaSr_3Fe_3O_{10-\delta}$) was measured by Cui et al. [62] under air, O_2 and N_2 atmosphere between 200 ^oC and 800 ^oC. It is revealed that a semi-conductor metal transition behavior due to the significant amount oxygen loss at high temperatures, the conductivity increased gradually before reached its maximum at around 400 ^oC, followed by a stable decrease when elevating the temperature.

1.5.5 Magnetic properties

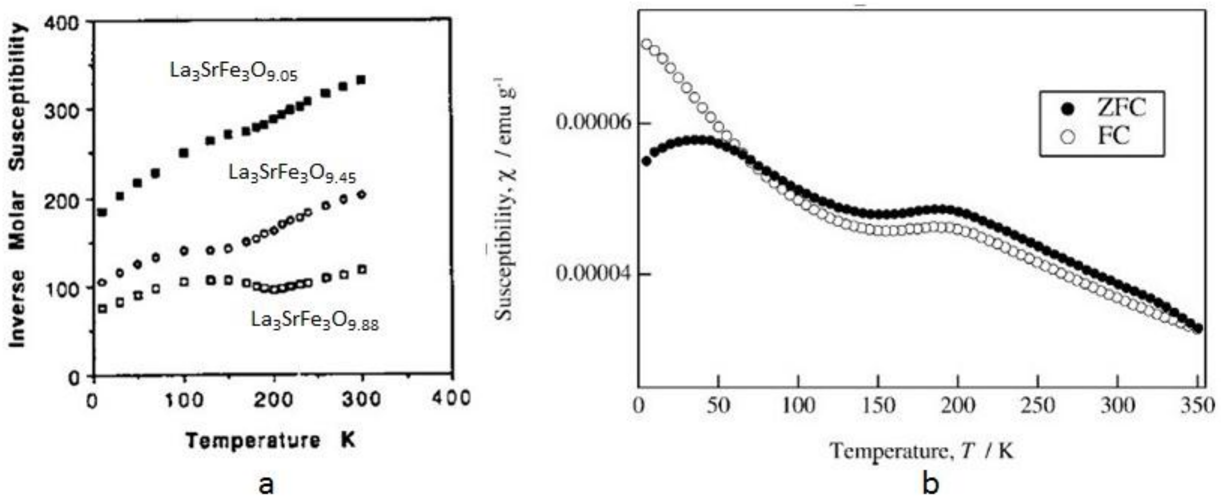

Figure 15. Magnetic properties of $La_3SrFe_3O_{10-\delta}$ series. (a) The inverse magnetic susceptibility as a function of temperature for $La_3SrFe_3O_{9.05}$, $La_3SrFe_3O_{9.45}$, $La_3SrFe_3O_{9.88}$ respectively [56]. (b) Temperature independence of the magnetic susceptibility of $La_3SrFe_3O_{10}$ [63].

As shown in Figure 15.a, magnetic susceptibilities of $LaSr_3Fe_3O_{10-\delta}$ series show that the inverse molar susceptibility nearly increases from 5 K to 300 K and the more oxygen vacancies in the sample, the larger inverse molar susceptibility. In Figure 15.b, it shows a broad hump near 200 K and where temperature dependent susceptibility is not typically from the antiferromagnetic materials, the author suspected the impurity substance attribute to this behavior.

1.5.6 Other properties

The properties of RP series have been widely investigated, such as the thermal expansion coefficient [44], conductivity as a function of partial pressure at various temperatures and Seeback coefficient [62], current density [44, 64], bulk density [64], Mössbauer spectra [65], etc.

Investigating of these properties is not included in this master's work, so which are not presented here.

1.6 Objective of the thesis

Complex oxides exhibit several chemical and physical properties that may open up for applications ranging from energy technologies to microelectronics. There is often a strong link between chemical composition, crystal structure and properties. In order to develop improved technologies for society, both theoretical and experimental studies for finding novel materials with optimized properties are needed.

The Ruddlesden-Popper type oxides, which is the focus of this Master thesis, is a less explored oxide class, but still have candidates that are quite promising as e.g. cathode materials for solid oxide fuel cells (SOFCs) and oxygen separation membranes. The Ruddlesden-Popper (RP) phases, named after their discovers, are (quasi) layered transition metal oxides described by the general formula $A_{n+1}B_nO_{3n+1}$ (A = alkaline earth; B = 3*d* element. Ln = rare earth enter on A site). This work focus on Fe-based Ruddlesden-Popper phases with Sr(II) and Ln(III) (Ln = La, Nd) as A-site cations. Iron has the interesting feature that it can exhibit several oxidation states, such as Fe(II), Fe(III) and Fe(IV). The huge flexibility in the iron oxidation state open up for tuning the oxygen deficiency that eventually may lead to interesting physical properties.

This thesis focus on investigate developing synthesis routes and sample handling that give phase pure products described by the formula this triple layerd perovskites with a composition of $Ln_xSr_{4-x}Fe_3O_{10-\delta}$ (Ln = La, Nd; $0 < x < 4.0$). The goal is to achieve a wide range of oxygen contents ($8.5 < 10-\delta < 10$) for some selected phase pure RP3 type samples by using different methods approaches; i.e. full oxidation, quenching and Zr-reduction. The oxygen content of these obtained compounds together with as-synthesized samples will be determined by cerimetric titration. Synchrotron and conventional X-ray diffraction along with Rietveld refinements will be used to refine the crystal structure and unit cell parameters. In addition, thermal analyses together with magnetic measurements for some selected samples will be carried out to fulfill a detailed investigation of their structural behavior and properties under certain conditions.

Chapter 2

Theory and methods

In this chapter are the methods and instrumentation used to synthesize and characterize RP3 phase oxides presented.

2.1 Synthetic methods

A rich variety of solids, including perovskites and its related phases, can be synthesized using a wide range of methods. There are abundant scientific reports regarding available methods [38, 66].

Generally, some typical methods of choice are available for the synthesis of perovskites and its related compounds as bulk:

- Solid-state/Ceramic methods (Shake and bake)
- Precipitation/Co-precipitation methods
- Sol-gel/Citric acid methods

The solid-state methods is one of the most frequently used routes for preparing mixed oxides using binary oxides, hydroxides, carbonates etc as starting materials. The procedure is based on that stoichiometric quantities of the starting materials are mixed and pelletized from the finely grinded powder and subsequently fired at very high temperatures to obtain complete reaction. Even though this method is popular because of simplicity, it has its important drawbacks as lack of full homogeneity in the complex solids due to incomplete reaction between the mixed precursors [38]. To achieve good sample quality repeated grinding, pelleting and heating circles are required. Further, the high firing temperatures may cause undesired impurities to be incorporated from e.g. the crucible material.

The last two methods are solution based techniques allowing mixing of the different cations on atomic level rather than being mixed by grinding. The fine powders obtain from the drying of the solution require and have shorter diffusion lengths. Thus these two methods can stabilize single phases at lower temperatures than ceramic route.

In this work, all samples were prepared using the so-called citric acid route. This method starts with dissolving all starting materials in diluted acid (typically HNO_3) to create a solution. All the cations are distributed uniformly on atomic level. Citric acid is added into the solution to form a sol of cation complexes. A drying process at moderate temperature (i.e. 160–200 ^{o}C) is required to start dehydroxylation and decarboxylation of the citric acid and a 3D net-work is starting to form. This gelling process is typically accompanied by a significant amount of shrinkage. In this work, the resulting gel is subsequently calcined at 450 ^{o}C in an oxidative environment to burn off the organic residues. The last step is repeating steps of grinding, pelletizing and annealing of the obtained amorphous powders at certain temperatures until desired single phases are obtained. Choice of atmosphere sintering (i.e. O_2, N_2, Ar) during the annealing process is also an essential parameter. The experimental details used in this work can be found in the experimental section (see subchapter 3.1.3, Page 46).

2.2 Large oxygen deficiencies

Complex oxides with presence of the multivalent cations as for instance Fe, Mn and Co opens up for preparation of oxygen deficient oxides. For RP3 phases, depending on the valence of the larger A-cation (A^{3+}), the B-cation can take valence $B^{+2.5}$ to $B^{+3.67}$ as for instance in the $PrSr_3Fe_{1.5}Co_{1.5}O_{10-\delta}$ system, corresponding to the oxygen content of $O_{8.25}$ and $O_{10.00}$ respectively [67].

In order to create samples with large oxygen deficiency, some methods of choice exist for reducing the oxygen content in RP3 phase oxides-Lattice oxygen can be removed from the oxides by annealing it in a reductive atmosphere (H_2, or a mixture of H_2 and N_2 or another inert diluting gas) [67] at suited temperature. Alternatively, as oxides are more oxygen deficient at high temperatures, the samples can be quenched from high temperature by putting it directly into liquid N_2 [62], or using an oxygen-getter as Zr [42]. An oxygen-getter is a metal that easily oxidize.

In this work, we used quenching and the oxygen-getter approach. The sample was quenched at different temperatures and allowed to cool down to ambient temperature in the desiccator. The pellet was crushed into powder right after and then three batches of ~50 mg powder were taken to determine its real oxygen content. Meanwhile, the powder was well kept in glove box ($pO_2 < 6$ ppm; $pH_2O < 1$ ppm).

Zr-reduction involve in principle a chemical transport reaction (CTR) [68]. The principle behind this approach is:

a) RP3 phase will naturally release or take up oxygen depending on pO_2 and temperature

$$A_4B_3O_{10-\delta 1} \overset{pO_2,T}{\Longleftrightarrow} A_4B_3O_{10-\delta 2} \qquad \text{Equation 9}$$

b) Correspondingly will a metal as Zr be oxidized/reduced depending on the pO_2 and temperature conditions

$$Zr \overset{pO2,T}{\Longleftrightarrow} ZrO_2 \qquad \text{Equation 10}$$

c) By controlling temperature conditions for oxide and metal so metal want to be in oxidized form and oxide want to release oxygen, one can controlled “pick out” or remove oxygen from the oxide’s oxygen lattice by adding a known quantity of metal to the oxide. A schematic drawing of a possible set-up is given in Figure 16.

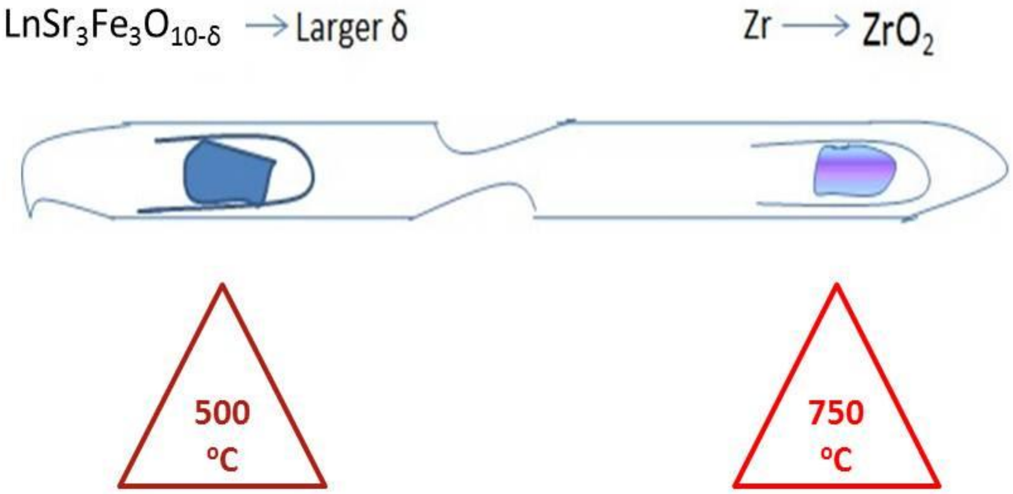

Figure 16. The schematic of the reactor used to tune oxygen content of RP3 phases. The oxygen-getter (Zr) is physically separated from the oxide it is reducing inside an evacuated sealed quartz tube.

The oxide and metal are physically separated by being located in different crucibles. The two crucibles may be located at the same or different temperatures in the reactor depending on their red-ox properties. Normally the metal is located at a higher temperature than the oxide.

The reactor is located in a furnace with a known temperature gradient (see Appendix A, Page 125), and the length of the reactor is decided based on desired temperature at oxide and metal (refer to Chapter 3 – experimental, Page 46). The reactor is put under vacuum so all oxygen the metal take up is originating from the oxide.

d) It is critical to choose crucible material that does not react with the metal. Ellingham diagrams show that Zr will be able to reduce SiO_2 but not Al_2O_3 up to approximately 600 ^oC [69]. For this reason Zr is located in dry Al_2O_3 crucibles.

e) After ended experiment the reactor is opened in a glove box ($pO_2 < 6$ ppm; $pH_2O < 1$ ppm). Oxygen content of the RP3 phase is then verified through cerimetric titration. And the Zr metal is carefully inspected to check if it is fully oxidized.

Assuming that the oxygen nonstoichiometry of the sample $LnSr_3Fe_3O_{10-\delta 1}$ is δ1 before reducing, while δ2 is the oxygen deficiency we aim to obtain (δ2 > δ1). During the process, the following chemical equation will take place:

$$LnSr_3Fe_3O_{10-\delta 1} + Zr \rightarrow LnSr_3Fe_3O_{10-\delta 2} + ZrO_2 \qquad \text{Equation 11}$$

After each sample is reduced, the practical oxygen content will be subsequently determined by cerimetric titrations. Care is taken to avoid any oxidization of the sample prior to the cerimetric titration (see section 2.4 and 3.2.3 for details for cerimetric titration)

2.3 Phase identification and structure refinement

In this work, some typical and essential methods are used to characterize the RP3 phase oxide and the most important step characterizing a solid-state material is to determine its crystal structure.

2.3.1 X-ray Diffraction

The RP phase oxides, we are aimed to get, are crystalline materials, in which the atoms and molecules are arranged in a regular pattern. The diffraction technology is not only designed for the basic phase determination but also for the further analysis, including cell parameters, structures etc.

X-ray, a form of electromagnetic radiation with a wavelength of 0.01 to 10 nanometers, was discovered by Wilhelm Conrad Röntgen while experimenting with Lenard and Crookes tubes and began studying them in 1895. Nearly at that time, it was strongly believed that crystals are consisted of many repeating blocks and each block has the same number of different atoms with the same pattern. Until now, these are well described in crystallography and classified into 7 lattice systems, 14 Bravais Lattice, 32 point groups and 230 space groups.

The diffraction will occur when the repeat distances in a crystal are of the order of magnitude of the wavelength of the radiation. Friedrich and Knipping performed the x-ray diffraction for the first time by using copper sulfate to study its crystal structure [70]. Bragg diffraction was first proposed by William Lawrence Bragg in 1912, he along with his father William Henry Bragg developed this relationship to explain the cleavage faces of crystals appear to reflect X-ray beams at certain angles of incidence. Several years later, Albert W. Hull pointed out that “every crystalline substance gives a pattern; the same substance always gives the same pattern; and in a mixture of substances each produces its pattern independently of the others” [71].

The discovery of the phenomenon of X-ray diffraction in crystals paved a way to the understanding of its structure. Many solid materials, around 95%, can be described as crystals, each of which produces a unique “X ray” fingerprint of diffracted X-ray intensities versus scattering angle that is becoming a possible characterization of an unknown material by comparing with the known patterns.

Now, the secrets behind it have become clear. When an x-ray electron beam hits an atom, the electrons around the atom start to oscillate with the same frequency as the incident beam. Destructive interference would occur in almost all directions while we only have the constructive interference occurring in crystals in a few directions. The X-ray we talked about reflects from a series of parallel planes inside the crystal, the set of the orientation and interplannar of atoms are defined by three integers donating as *hkl* which are called diffraction indices.

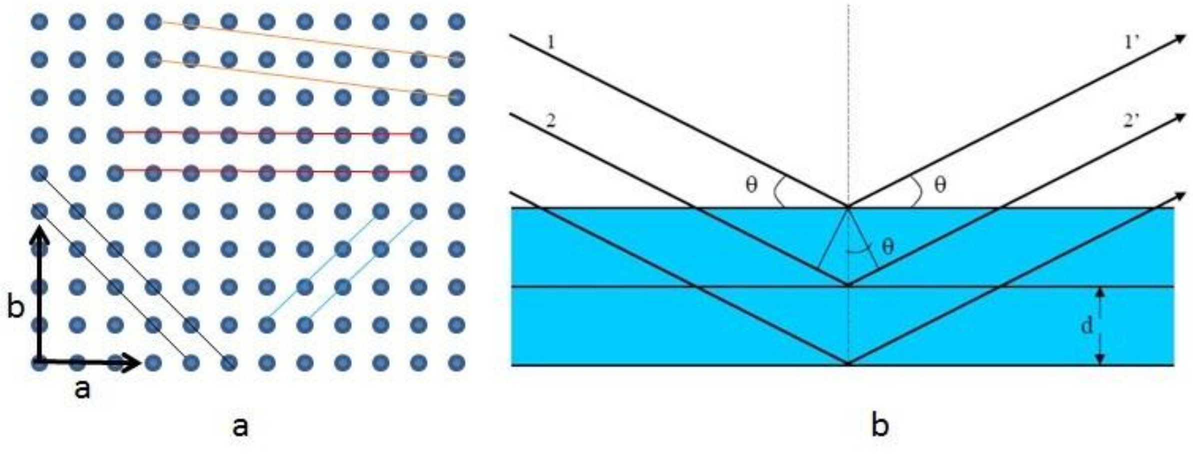

Figure 17. Princeple of X-ray diffraction. (a) Possible examples of equidistant atomic planes. (b) Constructive interference upon diffraction at two subsequent atomic planes.

Actually, many planes can be expected in a lattice, as seen from Figure 17.a, each of which would produce an X-ray reflection, the varied intensity of a spatial pattern of many reflections can be collected as a function of the glancing angle, illustrated in Figure 17.b.

$$n\lambda = 2d\sin\theta \qquad \text{Equation 12}$$

Where the variable d is the distance between a set of atomic planes in a crystal, λ is the wavelength of the incident X-ray beam, n is an integer, θ is the angle between the plane and incident beam.

A crystal consists of many sets of planes and these planes are characterized by interplannar distances d_{hkl}, which are a function of the size and the shape of the unit cell. And also other factors, including atomic numbers and the positions of the atoms in the unit cell, influence the powder pattern. In other words, a powder pattern has two characteristic features, the d spacings of the lines and their intensities.

A unit cell contains some specific atoms j of scattering factors f_j and coordinates x_j, y_j and z_j, the amplitude of a wave diffracted by an hkl plane set is given by the structure factor F_{hkl}:

$$F_{hkl} = \sum_j f_j \left[\cos(2\pi(hx_j + ky_j + lz_j)) + i\sin\left(2\pi(hx_j + ky_j + lz_j)\right)\right]$$

Equation 13

The intensities of a pattern peak are proportional to the square of F_{hkl} and also related chiefly to variations of electron and atomic scattering, interference effects, anomalous scattering and thermal motion of atoms. The intensity scattered by electrons is given by:

$$I = n\frac{I_o}{r^2}\left[\frac{e^2}{m_e c^2}\right]^2 \frac{1+\cos^2(2\theta)}{2} \qquad \textbf{Equation 14}$$

Where, n is the number of electrons of an atom, I_o is the intensity of the incident beam; e is the electron charge; m_e is the mass of the electron; c is the light speed and r is the distance from the scattering electron to the detector.

2.3.2 Synchrotron Radiation X-ray Diffraction

With the same principle of conventional X-ray diffraction, an experimental technique utilizing synchrotron radiation has been developed, offering more advantages [72]. Many orders of magnitude stronger than conventional x-rays, the intense form of radiation is the result of the deflection of highly energetic, charged particles, traveling at nearly the speed of light, accelerated in a strong magnetic field [73]. This resulting electromagnetic radiation emitted by these particles is passed through auxiliary components such as magnetic poles, called a wiggler or undulator, to further increase the x-ray intensity. This obtained electromagnetic radiation is of wide spectrum, which can be either used or monochromated to desired wavelengths for the experiments. These features made this so-called Synchrotron Radiation X-ray Diffraction (SRXRD) experiments as a highly valued research tool.

2.3.3 Rietveld refinement

When the data were collected via (SR)XRD, the next and probably the most important step is the completion of structure determination, which is the so-called Rietveld refinement. This method was named after Rietveld, who introduced and developed in late 1960s. The following paragraphs briefly demonstrate this method according to textbook [74] and review [75], by Robot Alan Young and Rietveld, H. M respectively.

The least squares approach is carried out to refine the theoretical and observed profile until the difference is minimized. This method is originally designed for neutron data due to simple peak shape by the relatively coarse resolution of neutron diffractometers [76], but now it is also widely used in both synchrotron and laboratory X-ray data.

However, if more factors are taken into consideration, the calculated intensities y_{cali} will be employed by the following equation.

$$\boldsymbol{y_{cali} = s\sum_K L_K [F_K]^2 \phi(2\theta_i - 2\theta_K) P_K A + y_{bi}}$$ **Equation 15**

where, *s* is the scale factor, *K* is the Miller indices, *hkl* for Bragg reflection, L_K presents the Lorentz, polarization and multiplicity factors, $\emptyset$ is the reflection profile function, P_K is the preferred orientation function, A is an absorption factor, F_K is the structure factor for the *K* th Bragg reflection, y_{bi} is the background intensity at the *i* th step.

The weighted difference in a Rietveld refinement between the observed y_{obsi} and the calculated y_{cali} diffraction patterns called Rietveld residual, donated as S_y.

$$\mathbf{S_y = \sum_i w_i (y_{obsi} - y_{cali})}$$ **Equation 16**

where, $\mathrm{w_i} = \frac{1}{\mathrm{y_{cali}}}$, y_{obsi} indicates the observed intensity at *i* th point, which is the raw data in the diffraction pattern.

The least squares minimization leads to a set of equations involving derivatives of the calculated intensities with some adjustable parameters x_j,x_k.

$$\boldsymbol{M_{jk} = -\sum_i 2w_i \left[(y_{obsi} - y_{cal}) \frac{\partial^2 y_{cal}}{\partial x_j \partial x_k} - \left(\frac{\partial y_{ci}}{\partial x_j}\right)\left(\frac{\partial y_{cal}}{\partial x_k}\right) \right]}$$ **Equation 17**

After deletion the first term $(y_{obsi} - y_{cal})$, an *m* by *m* matrix would be solved, where *m* is the number of parameters being refined. Because the residual function is not linear, the solution is found with an iterative procedure in which the shifts Δx_k, is gived by:

$$\boldsymbol{\Delta x_k = \sum M_{jk}^{-1} \frac{\partial S_y}{\partial x_k}}$$ **Equation 18**

The calculated shifts are subsequently used to produce an improved model and the procedure is then repeated. The relationships between the adjustable parameters and the intensities are not linear, thus the starting model must be as close as possible to the correct model or the non-linear least squares procedure will not give rise to the global minimum.

The atom positional, thermal, and site-occupancy parameters may be refined, what's more, parameters for the background, lattice, instrumental features, specimen displacement and transparence, crystallite size and microstrain are also available to be refined.

In the Equation 19, for the background, a simple phenomenological function is used to calculate the curve:

$$y_{bi} = \sum_{m=0}^{5} B_m[(2\theta_i/BKPOS) - 1]^m \quad \text{Equation 19}$$

Where *BKPOS* is the origin that is to be user-specified in the input control file.

For the angle dispersive data, the dependence of the breadth *H* of the reflection profiles, which is measured as full-width-at-half-maximum (FWHM), will be typically modeled as:

$$H^2 = Utan^2\theta + Vtan\theta + W \quad \text{Equation 20}$$

Here U, V and W are refinable parameters, can be written in terms of the angular divergence of the incoming neutrons to the monochromator, the angular aperture of a monochromator-to-sample collimator and the collimation between sample and detector.

Analytical reflection profile functions, in most programs, include two different Pseudo-Voigt functions, the Pearson VII function, Gaussian and Lorentzian function. There exist some refinement programs available, i.e. GSAS [77], TOPAS [78], and *Fullprof* [79] etc. using the above mentioned model of principles and methods.

Among these popular refinement programs, in this work, the refinement is carried out by TOPAS (TOtal Pattern Analysis Solutions) [78]. This software is a graphic based profile analysis program within a general non-linear least squares fitting system.

Typically, a refinement starts with the background and scale factors, followed by the unit cell and profile parameters. The Rietveld refinement will proceed by adjusting parameters until the residual is minimized, in other words, a best fit will be obtained. In the process, several R-values, detailed in Table 6, are developed to make the judgments of the fit. From the mathematical point of view, R_{wp}, as the most meaningful among these R-values, which best reflects the progress of the refinement.

Table 6. Some R-values of the fitting [74]

R-related funcions	Name
$R_F = \frac{\sum \left\| {I_{K(obs)}}^{1/2} - {I_{K(cal)}}^{1/2} \right\|}{\sum {I_{K(obs)}}^{1/2}}$	*R*-structure factor
$R_B = \frac{\sum \left\| I_{K(obs)} - I_{K(cal)} \right\|}{\sum I_{K(obs)}}$	*R*-Bragg factor
$R_P = \frac{\sum \left\| y_{obsi} - y_{cali} \right\|}{\sum y_{obsi}}$	*R*-pattern
$R_{wp} = \left\{ \frac{\sum w_i (y_{obsi} - y_{cali})^2}{\sum w_i {y_{obsi}}^2} \right\}^{1/2}$	*R*-weighted pattern

Here, I_K is the intensity of the K th Bragg reflection.

The goodness of the fit (GOF), x^2, is perhaps the most popular indicator.

$$\mathbf{GOF} = x^2 = {R_{wp}}/{R_{exp}} \qquad \textbf{Equation 21}$$

R_{exp} is the expected R value, reflecting the quality of the collected data.

$$R_{exp} = \left[\frac{N-P}{\sum_i^N w_i y_{obsi}^2} \right]^{1/2} \qquad \textbf{Equation 22}$$

Where N is the number of observations and P is the number of parameters. For a good fit, the x^2 should be between 1.3 and 1.7, and R_{wp} and R_p are as low as possible.

2.4 Cerimetric titration

Cerimetric titration is a well established method to determine the oxygen content of certain complex oxides containing high valent cation as iron in $LnSr_3Fe_3O_{10-\delta}$ (Ln = La, Nd). $LnSr_3Fe_3O_{10-\delta}$ occurs over a wide range of specific oxygen contents.

Cerimetric titration is of volumetric chemical analysis and was first proposed by Lange in 19th century and the systematic works started in the 1920s, while methods based on Ce (IV) sulfate as titrant were developed by Furman et al. [80] at the same time. In 1957, Kolthoff et al. described detailed procedures for cerimetric titration based on his classic work [81].

Cerimetric titration is a quantitative re-dox method where a colour change is observed at the endpoint of the titration due to complete consumption of the Fe^{2+}-1,10 phenanthroline complex (Ferroin) according to:

$$Ce^{4+}(aq) + Fe^{2+} - 1,10\ \text{phenanthroline}\ (\text{aq}) \rightarrow Fe^{3+} + Ce^{3+} \qquad \textbf{Equation 23}$$

Since cerimetry is linked to $Fe^{2+}/Fe^{3+}/Fe^{4+}$ red-ox pairs, it can be used for determining oxidation state of iron in oxides by either oxidizing Fe^{2+} to Fe^{3+} or reducing Fe^{4+} to Fe^{3+}. Fe^{3+} will not react with Ce^{4+}. It should be pointed out that Fe(IV) not is a stable aqua species, but exists in solid oxides as perovskites and Ruddlesden-Popper phases. Cerimetry for determining oxidation states of nickel and cobalt in oxides as are also reported in the literature [82]. The indicator is the same, making coloured complexes with cobalt and nickel.

In this work we have focused on determining the valence of iron in $LnSr_3Fe_3O_{10-\delta}$ (RP3 phase) to determine the oxygen content. Valence of La, Sr and O are fixed to +3, +2 and −2, respectively. We base the cerimetric titration on adding excess Fe^{2+} cations from an external salt ($Fe^{2+}_{\text{Mohr-salt}}$) to the RP-type oxide, and dissolve the mixture in an acidic solution under inert conditions. Iron in Mohr salt will react with iron from the oxide according to:

$$\mathbf{Fe^{2+}_{sample} + Fe^{2+}_{Mohr\text{-}salt} \rightarrow 2Fe^{2+}_{solution}} \qquad \textbf{Equation 24}$$

$$\mathbf{Fe^{3+}_{sample} + Fe^{2+}_{Mohr\text{-}salt} \rightarrow Fe^{3+}_{solution} + Fe^{2+}_{solution}} \qquad \textbf{Equation 25}$$

$$\mathbf{Fe^{4+}_{sample} + Fe^{2+}_{Mohr\text{-}salt} \rightarrow 2Fe^{3+}_{solution}} \qquad \textbf{Equation 26}$$

Fe(II) in the acidic solution, after being completely dissolved and fully reacted with Mohr salt, is subsequently titrated with a Ce^{4+} solution with known molarity (equation x). Based on consumed Ce^{4+}, quantity of added Mohr salt and dissolved oxide, the valence of iron in the dissolved oxide can be extracted.

Iron has average valence 3.67 in $LnSr_3Fe_3O_{10.00}$ ($\delta = 0$), 3.00 in $LnSr_3Fe_3O_{9.00}$ ($\delta = 1$) and 2.67 in $LnSr_3Fe_3O_{8.50}$ ($\delta = 1.5$). According to Equations 24-26, amount of Fe (II) titrated will be:

- less than added mole Mohr salt for $\delta < 1$
- equal to added mole Mohr salt for $\delta = 1$

- larger than added mole Mohr salt for $\delta > 1$

Since we with Mohr salt only reduce iron in the RP oxide to Fe (III) we define iron as having valence 3+x; or Fe^{3+x}. We set up the calculations according to this to find x (and δ) in Fe^{3+x} in $LaSr_3Fe_3O_{10-\delta}$:

- **mol Fe^{3+x} in sample = C = Mohr salt added – consumed mole Ce^{4+} Equation 27**
- **mol $Fe^{3+x} = 3x*(mass_{sample}/(FW_{LaSr3Fe3O9} + 3x/2*FW_O))$ Equation 28[1]**
- **$x = C*FW_{LaSr3Fe3O9} / (3mass_{sample} - 3/2*C*15.999)$ Equation 29**
- **$\delta = 5.5 - (3/2)*(3+x)$ Equation 30[2]**

In order to obtain accurate measurements it is critical to perform some few tests prior to the titration. These are:

- Find good experimental conditions to dissolve the oxide. It is optimal to dissolve the oxide in 1-3 M HCl within some minutes; however stronger acid may be necessary. Experience also show that some oxides need several hours and heating to be fully dissolved.

- Dimension/scale the experiment so you during the titration consume approximately 80% of the volume of the buret (mole Mohr salt, mole oxide versus mole Ce^{4+}).

- Determine exact formula weight of Mohr salt by gravimetry (see Chapter 3.1.3 and 4.1.1).

- Standardize the ~0.1 M $Ce(SO_4)_2$ solution by titrating it with Mohr salt with known exact formula weight.

For the calculations of cerimetric titrations, see Appendix F (Page 140).

---

[1] 3x = 3x Fe atoms per x $LaSr_3Fe_3O_{10-\delta}$ units; $3x/2*FW_O$ 3x Fe per formula unit + valence of O = -2, We need ½ O to reduce 1 Fe^{4+} to 1 Fe^{3+}.

[2] Note $\delta < 0$ imply average valence of iron > 3.67.

2.5 Thermal Analysis

Thermal analysis is a tool of studying changes in materials properties as function of temperature. Some frequently used methods are: differential thermal analysis (DTA) for temperature differences, differential scanning calorimetry (DSC) for heat differences, dilatometry (DIL) for volume changes, thermo-mechanical analysis (TMA) for change of a dimension or a mechanical property, thermo-optical analysis (TOA) for change in optical properties and thermogravimetric analysis (TGA) for mass changes [83].

As TGA is used in this work, a more detailed overview of this technique will be given in the following.

Thermogravimetric analysis (TGA), also called thermogravimetry (TG), is a technique where the mass of a sample is measured as a function of temperature (with constant heating/cooling rate) or at constant temperature (isothermally) in a well-defined atmosphere. Typically, the sample is exposed to an inert gas as N_2 or Ar, or a gas or gas-mixture containing reactive species as O_2, H_2 and CO_2.

The sample may lose or gain mass depending on the specific chemical reaction taking place in the applied atmosphere. TGA is not only a basic tool of providing information about physical phenomena, including vaporization, sublimation, absorption, and adsorption and desorption, but also a useful technique for study the chemical properties, such as chemisorption, dehydration, decomposition or oxidation and reduction etc. Typically TGA instruments are operated up to 1100-1200 ^{o}C, but certain designs allows temperatures as high as 2000 ^{o}C.

Duval, Keattch and Dollimore have fully demonstrated the origin of this method [83]. The core of the apparatus, the balance, has been through a tremendous development from the lever-arm balance to the electronic microbalance giving increasing degrees of precision. Up to now, this method allows smaller samples (~ 50 mg) to be used [83].

The design of the TGA instruments is different from supplier to supplier by means of the construction of the balance, how the gas is flowing over the sample as well as furnace system including location of the thermocouple. Figure 21 is the TG instrument used in this work, Experimental part (Page 50).

2.6 Magnetic properties

Magnetic property is a physical phenomenon that includes forces exerted by magnets. Modern study on transition metal oxide dated from the 1930s by Pauling. The magnetic susceptibility, x, is a dimensionless proportionality constant that indicates the degree of magnetization of a material response when placed in a magnetic field. These magnetic responses differ greatly in strength.

In general, materials may be classified by the response to externally applied magnetic fields. Diamagnetism is a weak property of all materials and opposes the applied magnetic fields. Paramagnetism is larger than diamagnetism and exhibits proportional magnetization in the same direction of the applied field. In addition to that, some paramagnetic materials at a certain temperature have interactions that exist in a more ordered state, can be either ferromagnetic or antiferromagnetic. Ferromagnetic effects are very large, producing magnetizations sometimes orders of the magnitude greater that the applied field and as such are much larger than either diamagnetic or paramagnetic effects. More complex behaviors can arise from the existence of locally ordered spins (FM or AFM) in a certain structural arrangement; these magnetically frustrated systems are spin glasses. These are presented schematically in Figure 18.

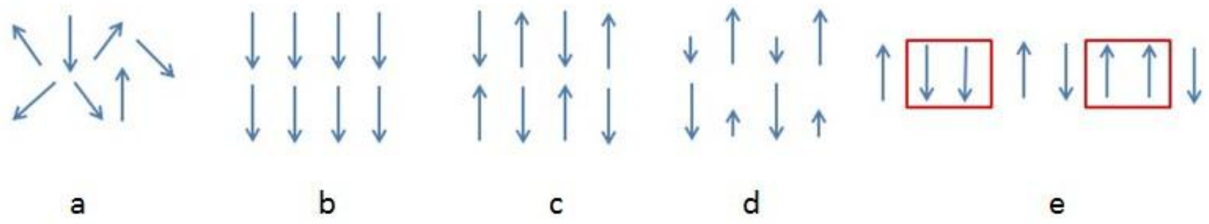

Figure 18. Schematic representations of magnetic arrangement of spins. (a) Paramagnetism. (b) Ferromagnetism. (c) Antiferromagnetism. (d) Ferrimagnetism. (e) Spin glass, the area of short-range order are highlighted by red boxes.

When perovskites incorporate magnetic transition metals, they may exhibit any of these four interaction schemes. If more additional influence of internal or/and external stimuli, such as substitution, deficiencies, temperature, impurities or pressure allow to switch between these five aforementioned magnetic states.

The magnetization M of a material is expressed in terms of density of net magnetic dipole moments u_{total} in the material.

$$M = \frac{u_{total}}{V}$$ **Equation 31**

Then the total magnetic field in the materials is gived by

$$B = \mu_o(H + M)$$ **Equation 32**

Where μ_o is the vacuum permeability, H is the applied magnetic field. The quantity $\mu_o M$ is called magnetic polarization.

And the magnetic susceptibility is defined as:

$$x = \frac{\partial M}{\partial H}$$ **Equation 33**

A volume-independent magnitude is the molar susceptibility x_{mol}, which can be deduced from the dimensionless proportionality factor x:

$$x_{mol} = xV_{mol} = x_g M_{mol}$$ **Equation 34**

V_{mol} is the molar volume, M_{mol} the molar mass and $x_g = {}^{x}/_{\rho}$ is the so-called specified mass susceptibility.

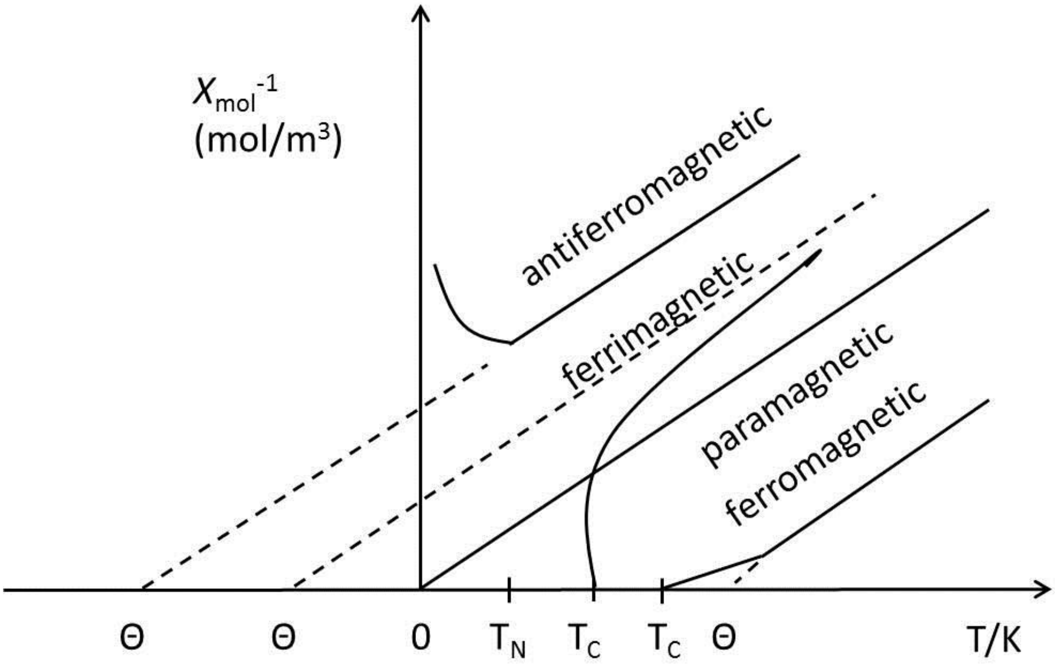

Figure 19. The reverse susceptibility as a function of temperature for magnetic materials.

The susceptibilities of a magnetic material are distinguished by their magnitude and temperature dependence. A plot of the reciprocal of the measured susceptibility x^{-1}_{mol} as a function of T is of a straight line with a slope of 1/C, and the intersect of the x axis is at T = θ and this temperature is called Weiss temperature. Curie law is applied in ideal paramagnets, $x = \frac{C}{T}$, when there is a predisposition between the adjacent spins due to a certain interaction, then the Curie-Weiss law $x = \frac{C}{T-\theta}$, where θ is called the Neel temperature. As shown in the above Figure 19, the reverse susceptibility versus temperature for an antiferromagnets, $\theta < 0$, for a ferromagnet, $\theta > 0$, means ferromagnet, in comparison an ideal paramagnet $\theta = 0$.

In Curie law, the quantitative relation is given by the Curie constant:

$$C = u_o \frac{N_A^2 u^2}{3R} \qquad \textbf{Equation 35}$$

R = gas constant, N_A is the Avogadro number and u_o is the magnetic field constant.

The term effective paramagnetic moment u_{eff} is defined as division of u by u_B, yielding the experimentally determined value of a sample, expressed as:

$$u_{eff} = \frac{u}{u_B} = \frac{1}{u_B}\sqrt{\frac{3R}{u_o N_A^2} x_{mol}(T-\theta)} \qquad \textbf{Equation 36}$$

By considering 1 mole per unit volume, n = n_A, and the molar susceptibility, we obtain:

$$u_{eff} = 2.828\sqrt{x_{mol} T} \qquad \textbf{Equation 37}$$

In the case of spin-only paramagnetic materials, we can obtain the number of unpaired electrons:

$$n = 2S = -1 + \sqrt{1 + u_{eff}^2} \qquad \textbf{Equation 38}$$

S is the spin quantum number in Equation 38.

The magnetization still exists in the materials after the sample is treated with external field. Moreover, a hysteresis curve shows this kind of behavior, see Figure 20.

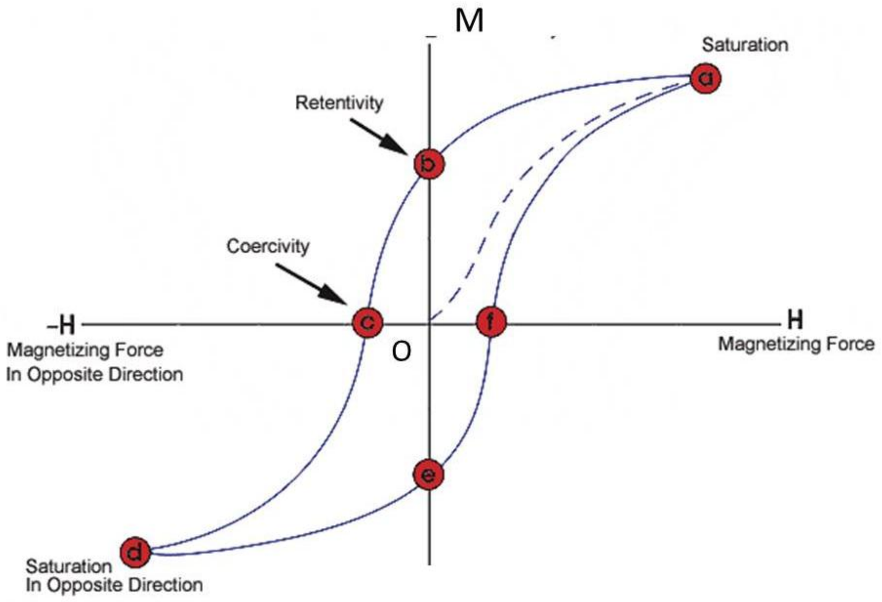

Figure 20. Typical hysteresis loop for ferromagnetic materials [84]

An increasing external field is applied to an untreated sample, causing a rising magnetization of the sample until saturation is reached (O → a). After turning off the field, the magnetization decrease to a remnant magnetization, also called Retentivity (a → b). The spin will experience a reorientation by applying opposite magnetizing force (b → c), the minimum of this is called coercivity. If the magnetizing force increases continuously, the saturation will be observed in opposite direction (c → d).By switching off the field and then reversing the force, the magnetization of the sample would experience reorientation again (d → e → f → a). Thus, the hysteresis loop is obtained.

Depending on the application, materials with large remnant magnetization are called hard ferromagnets while substances with small magnetization are called soft ferromagnets.

The magnetic behavior as a function of temperature M(T) and field M(H) will be measured by Magnetic Properties Measurement System (MPMS) and/or Physical Properties Measurement System (PPMS), Quantum design. The experimental details together with the instrument are presented in section 3.2.4.

Chapter 3

Experimental

In this chapter are the experimental work done in this Master's project is described. The experimental work includes procedures relative to sample preparation and various apparatuses for property measurements and characterization.

Firstly, all samples were synthesized using the citric acid method. Sample purity was investigated by means of powder X-ray diffraction (XRD). Phase pure powders of $LnSr_3Fe_3O_{10-\delta}$ (Ln = La, Nd) were subsequently transformed to series of oxygen deficient samples by performing different oxygen content sensitive post-treatments. The valence of the B site (Fe ion) was determined by the cerimetric titration which in turn allows us to calculate the oxygen content of these samples. In addition, thermogravimetry was utilized to study the oxygen stoichiometry as a function of heating and cooling condition in air. Synchrotron radiation X-ray diffraction (SRXRD) was carried out for some selected samples for crystal structure evaluations, and magnetic properties were investigated by MPMS and PPMS.

3.1 Synthetic experimental

3.1.1 Chemicals used in the experimental study

In order to avoid the influence of impurities, very high-purity starting materials are used, most of the main starting materials are listed in table 7.

Table 7. Overview of starting materials

Chemicals	Formula weight g/mol	Purity / Concentration	Supplier or Manufacturer
[1]Nd_2O_3	336.48	99.99%	Molycorp
[1]La_2O_3	325.81	99.99%	Molycorp
[2]$SrCO_3$	147.63	> 98%	Fluka
[2]$Fe(COO)_2 \cdot 2H_2O$	179.89	99%	Molycorp
[3]HNO_3	--	68%	VWR PROLABO
[3]HCl	--	37%	MERCK
[2]$(NH4)_2SO_4 \cdot FeSO_4 \cdot 6H_2O$	392.14	99%	SIGMA-ALDRICH
[4]Zr	91.22	99.8%	A. D. Mackay Inc
$C_3H_4(OH)(COOH) \cdot H_2O$	210.14	≥ 99.5%	SIGMA-ALDRICH
[3]Ferroin	692.52	0.025 M	Fluka
[3]$Ce(SO_4)_2$	332.24	0.1 M	Fluka
[5]Ar	--	99.999%	AGA
[5]H_2	--	99.95%	AGA
[5]O_2	--	99.95%	AGA
[5]Air	--	99.95%	AGA

1 Fired at 800 °C prior to use for removal of adsorbed CO_2 and H_2O (See section 3.1.2)

2 Exact formula weights determined by gravimetry (for results see section 4.1.1)

3 Liquid, molarity of $Ce(SO_4)_2$ determined at onset of every titration

4 In forms of chips

5 Compressed gas

Table 7 gives an overview of all chemicals used in the experimental part of this study. In addition, procedures for pre-treatment of chemicals in form of firing for removal of adsorbed humidity and carbon dioxide as well as formula weight determination are described in following subchapters.

3.1.2 Pretreatment of rare earth oxides Ln_2O_3 (Ln = La and Nd)

La_2O_3 and Nd_2O_3 were fired in a muffle furnace at 800 ^{o}C over night to prior to synthesis in order to remove water (e.g. $Ln(OH)_3$, Ln = La, Nd) and carbon dioxide (e.g. $Ln_2O_2CO_3$, Ln = La, Nd) absorbed by the powder. The fired oxides were transferred directly from 800 ^{o}C into a desiccator and cooled down to room temperature. To ensure completely dry starting materials, this procedure was repeated at least once per month.

3.1.3 Procedure for determination of formula weights

To determine the exact formula weights of $SrCO_3$, Mohr salt ($(NH4)_2SO_4\cdot FeSO_4\cdot 6H_2O$) and $Fe(COO)_2\cdot 2H_2O$, the following procedure was followed.

Generally, label four crucibles and fire them with some quartz wools overnight at 800 ^{o}C, and transfer crucibles and quartz wool into a desiccator and allow them to equilibrate to ambient conditions (room temperature). Weigh the crucibles, repeat the firing until constant weights of crucibles are obtained. Weight out approximately 2 g materials to each crucible and add known quantity of quartz wools as a blanket covering the chemicals.

Table 8. Chemicals and their maximum temperature and decomposed phases

Chemicals	Maxi. Temp.	Decomposed phases
$SrCO_3$	1100 ^{o}C	SrO
$Fe(COO)_2\cdot 2H_2O$	800 ^{o}C	Fe_2O_3
$(NH_4)_2SO_4\cdot FeSO_4\cdot 6H_2O$	800 ^{o}C	Fe_2O_3

Anneal the crucibles following the program: Ramp: 2 ^{o}C/min → temperature higher enough for the materials to be decomposed completely (see Table 8 for detail) for approximately 20 hours. Transfer hot crucibles into desiccators and allow them to equilibrate to ambient temperature.

$$SrCO_3 \xrightarrow{1100\ ℃} CO_2(g) + SrO\ (s) \qquad \text{Equation 39}$$

$$Fe(COO)_2 \cdot 2H_2O\ (s) \xrightarrow{800\ ℃} Fe_2O_3\ (s) + CO_2\ (g) + H_2O(g) \qquad \text{Equation 40}$$

$$(NH_4)_2SO_2 \cdot FeSO_4 \cdot 6H_2O\ (s) \xrightarrow{800\ ^{\circ}\mathrm{C}} Fe_2O_3\ (s) + CO_2\ (g) + NH_3\ (g) + SO_2\ (g) + H_2O(g)$$

Equation 41

Weigh the four crucibles, and repeat until constant weights are obtained. Run XRD of obtained oxides to confirm phase content (see Equations 39-41). After each step is done, the mean data of the real formula weight will be taken from the four parallel measurements (for results see section 4.1.1, Page 57).

3.1.4 Synthetic procedure

In this work, we used the citric acid method for the preparation of all RP3 oxides. The RP3 oxides can be described by the general formulas:

$La_xSr_{4-x}Fe_3O_{10-\delta}$; $0 < x < 4.0$

$Nd_xSr_{4-x}Fe_3O_{10-\delta}$; $0 < x < 4.0$

In short, the procedure starts with weighing out stoichiometric amounts of pre-treated reactants on a five digits analytical balance from Mettler Toledo. The starting materials (rare earth oxides, iron-oxalate and strontium carbonate) were dissolved in nitric acid (approx. 6M) in separate beaker until the solution became clear. Then the solutions were mixed in a large beaker together with citric acid (~100 g citric acid per 2 gram product). The obtained solution was then heated under stirring conditions for removal of water and nitrous gases. The temperature was throughout this step kept below 170 ^{o}C.

When the nitrous gases have boiled off, the clear melt was transferred to a porcelain bowel. An Al-foil was wrapped around the bowel and small holes were made in the foil to allow water and carbon dioxide from the dehydration and decarboxylation process to disappear. Dwell time of the first heating step was for 12–24 hours in an oven holding 180 ^{o}C.

The obtained crust was thereafter crushed and transferred to a muffle furnace for removal of carbon species at 450 ^{o}C for 18–24 hours giving a fine brownish powder, which in next step was pressed into 1.0 cm diameter tablets using a hydraulic tablet press (100 bar). The pellets were fired in a furnace at 1000 ^{o}C for 12 hours before increasing the temperature to 1250 ^{o}C and annealed for another 12 hours (in air). To ensure full homogeneity, the pellets were crushed to powder again and pressed into new pellets. The second annealing were done at the temperature in the range 1200-1450 ^{o}C for 12 hours in air, depending on the desired chemical composition of the Ruddlesden-Popper oxide. Details regarding the final annealing step are given in the result part, section 4.1.2 (Page 58).

To ensure fully oxidized RP3 phases, the tablets from the final annealing step were crushed and the obtained fine powder was post annealed in a 100% oxygen flow at 350 ^{o}C for 3 days.

On the contrary, different oxygen deficient samples were obtained by ***1)*** Quenching, taking the sample out at different temperatures and allow it to cool down in desiccator, or ***2)*** reduce as-synthesized samples by oxygen-getter Zr via chemical transport reaction method, see section 3.1.5.

3.1.5 Preparation of oxygen deficient samples

Oxygen content of some selected phase pure RP3 phases (as-synthesized $LnSr_3Fe_3O_{10-\delta}$, Ln = La, Nd) was selectively tuned to create series of RP3 oxides with variable oxygen stoichiometry. To carefully control the oxygen content of the reduced variants, the exact oxygen content of the corresponding as-synthesized RP3 samples were determined by cerimetric titration (see details in section 2.4). This allowed us in the next step to load the reduction reactor with exact quantities of the oxygen-getter Zr (see Figure 16, Chapter 2, Page 29).

In this study the RP3 oxides were kept at 500 ^{o}C and Zr at 750 ^{o}C. The oxide and Zr were loaded in stoichiometric quantities into quartz and Al_2O_3 crucibles, respectively (see Figure 16 Chapter 2). Distance between the oxide and Zr in the reduction reactor is given by the actual gradient in the applied furnace. Figure A-1 (refer to Appendix A, Page 125) shows a typical temperature gradient for the furnace used for these experiments. The quartz reactor was carefully evacuated after it was loaded with both the oxide and Zr using a vacuum pump before it was sealed in a H_2/O_2 torch. Vacuum was confirmed using a vacuum indicator, which gives a purple color for the pressure below 20 Torr. The reduction reactor was then located inside a furnace with a known temperature gradient.

Finally, the furnace was heated to desired temperature and kept there for 3 days. After ended experiment the furnace was switched off and the reduction reactor carefully slided out of the furnace and cooled down to ambient temperature. The reduction reactor was opened in the glove box and the Zr was inspected to check if it had become fully oxidized (white chips). For each reduced oxide, three ~50 mg batches were taken for determining oxygen content by means of cerimetric titration (refer to section 3.2.3).

3.2 Samples characterization

The crystal structure and phase purity were confirmed by (Synchrotron Radiation) X-ray diffraction.

3.2.1 X-ray diffraction

Phase assemblages were ascertained from powder X-ray diffraction. These data were obtained from Bruker Advanced D8 X-ray diffractometer running in Bragg-Brentano geometry with Cu $K_{\alpha1}$ radiation (λ = 1.540598 Å). The diffraction pattern covers a 2θ range from 2^o to 90^o with 1s count per step length of 0.021^o.

Here, there are two ways of preparing sample for the XRD.

- Powders from as-synthesized and fully oxidized samples were mixed uniformly together with a small amount of a silicon NIST standard. A very thin layer of vacuum grease was wiped on a sample holder, and then a small amount of these mixed powders was dispersed on it with sheet glass.
- The reduced sample was stored in the glove box. After the sample was prepared on the holder as described above, it would be covered by a very thin plastic foil to avoid any oxidization and hydration. The XRD will be carried out right after it is taken out from the glove box.

For this work, high resolution data from SRXRD experiments were collected with a 2-dimensional detector at Swiss-Norwegian Beam Line (SNBL) at the European Synchrotron Radiation Facility (ESRF) in Grenoble, France. The sample was loaded into a quartz-glass capillary with an outer diameter of 0.5 mm and then closed with a length of around 2 cm. The wavelength used was 0.504856 Å, and the data was collected from 2θ = 0.003^o to 36.841^o using a step length of 0.00615^o.

The experimental diffraction data were analyzed with the software DIFFRAC^{plus} EVA to confirm the phase identification with known fingerprints in the database. Further, TOPAS was used to conduct the refinement with the unit cell parameters, atomic coordinates and crystal structure of the specimen. The data will be compared with previous published literatures.

3.2.2 Thermogravimetric analysis

A Netzsch STA449 F1 Jupiter instrument was used to conduct the thermogravimetric analysis (TGA) measurements.

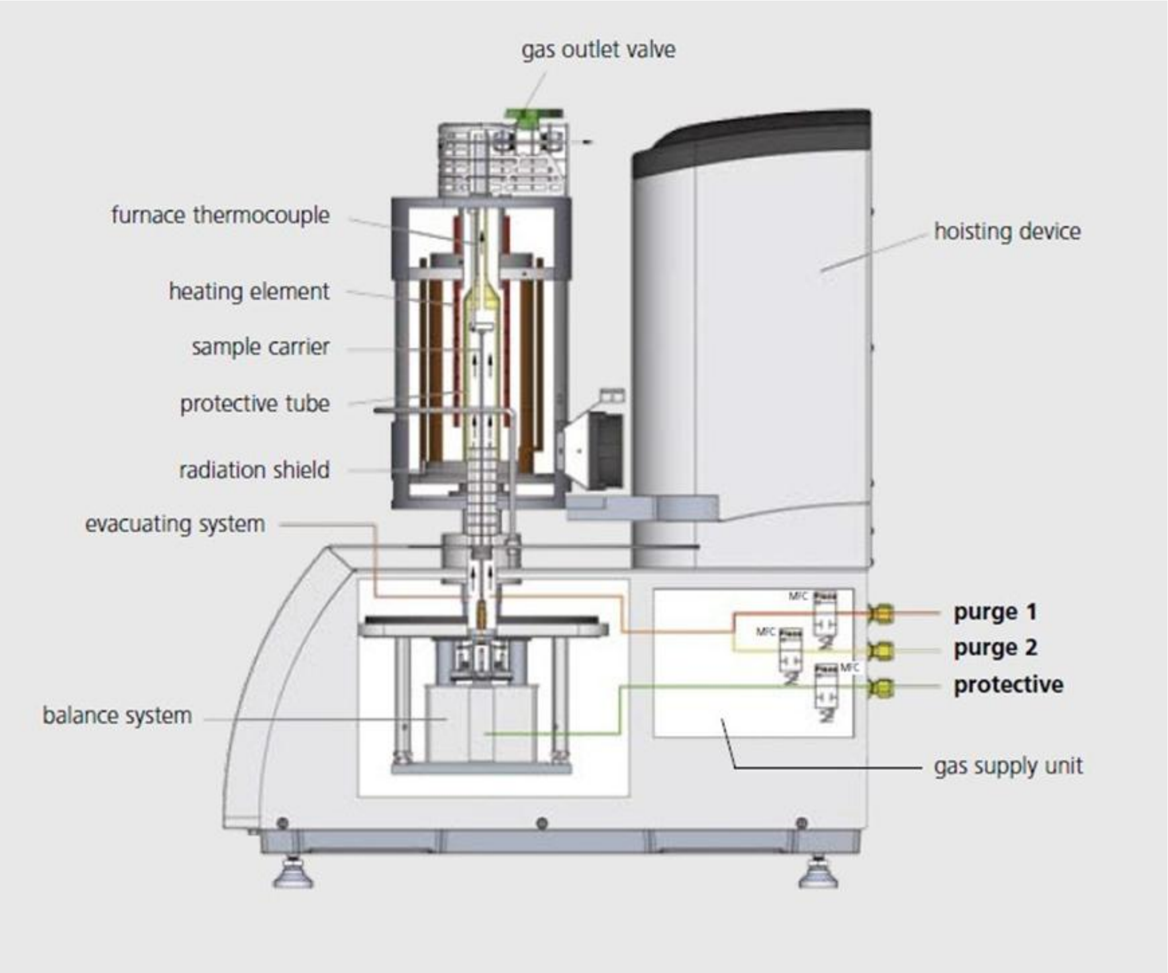

Figure 21. schematic drawing of a Netzsch STA449 F1 TG instrument [85]

In Figure 21, is a schematic drawing of a TGA presented, showing its main components. This instrument consists of an evacuating system, a high water vapor pressure furnace and a hoisting device. As shown in Figure 21, there are three gas paths (purge 1, 2 and protective path) linking to the chamber. In this work, purge 2 allows air to flow into the TG because measurement is carried out in constant atmosphere. The protective gas path flushed by the dried N_2 into the instrument has the function of protecting the system, especially when it is operated at high temperatures.

Around 50 mg sample was evenly distributed in a clean Pt crucible. The measurements were conducted using a 50 ml/min synthetic air-flow above the sample, and a N_2 flow of 25 ml/min over the balance. Measurements were done in temperature range from 30 ^{o}C to 1200 ^{o}C with a heating and a cooling rate of 10 ^{o}C/min. An isothermal step of 10 minutes at 1200 ^{o}C was included between the heating and cooling steps. See flow diagram of the used temperature program in Figure 22.

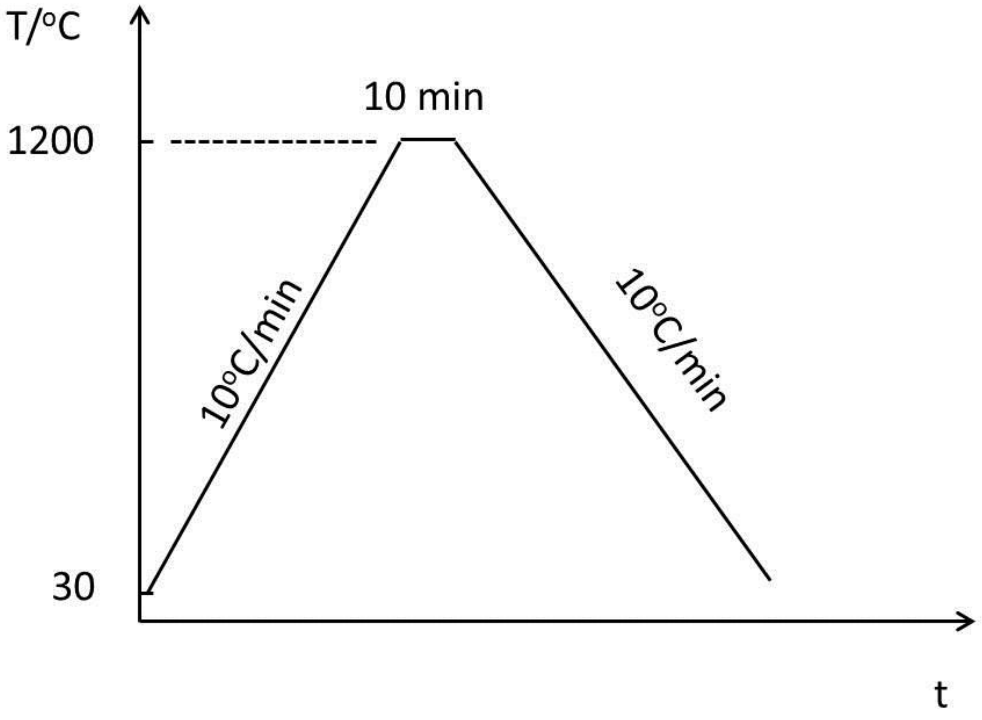

Figure 22. Temperature profile in TG measurement

To correct for the buoyancy effect, all experiments were run with a so-called background. The background curve was obtained running an empty Pt crucible at exactly the same conditions as the experiments. In addition, the instrument is routinely calibrated with respect to temperature and weight by instrument responsible.

3.2.3 Cerimetric titration

The experimental procedure used in this work started with preparing degassed acidic solution of HCl (1 M, adaptable to the solvability of the sample). Degassing was performed by bubbling inert gas (He) through boiling water, which subsequently was used to dilute the HCl. Further, the diluted HCl was kept under an inert N_2/Ar blanket throughout the procedure.

Next step was to add a known amount (~0.35 g, depending on the composition) of Fe^{2+} (in excess to the amount of high valent cations in the sample) in the form of $(NH_4)_2.Fe(SO_4)_2·6H_2O$ (known as "Mohr's salt") into 100 ml ~1 M HCl. Then the stable Fe^{2+} salt was allowed to dissolve before the fixed amount (~50 mg) of oxide sample was added to the solution. The solution with the salt and sample was throughout the procedure kept under an inert atmosphere to avoid O_2 from air to oxidize Fe^{2+} in the solution to Fe^{3+}, giving false high valence of iron in the oxide (see the color as Figure 23.a).

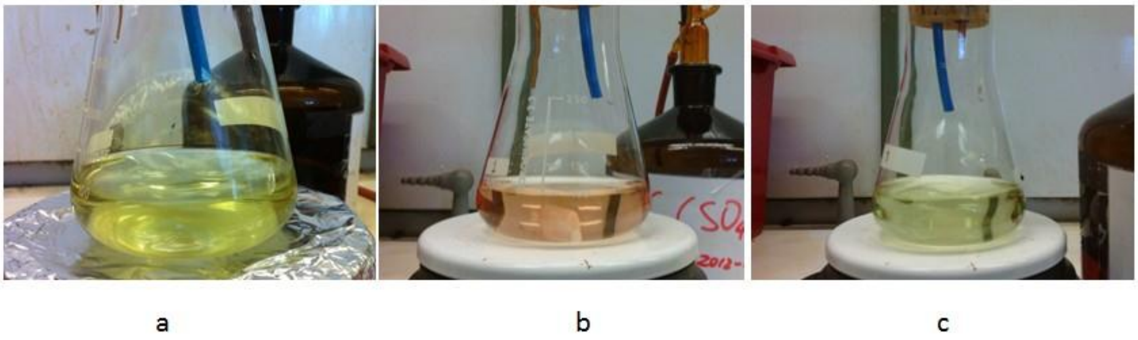

a b c

Figure 23. Color changes within titration. (a) The color of fully dissolved $LnSr_3Fe_3O_{10-\delta}$ sample. (b) The color change to light red when Ferroin added into the solution. (c) The color returns to light green after titrating.

Finally, before titrating the mixture by the standardized solution of $Ce(SO_4)_2$ (the color of mixed Fe^{3+} and Ferroin, see Figure 23.b), the red-ox indicator (Ferroin) was added to the solution (one drop was enough, the color of the solution is as shown in Figure 23.c).

$Ce(SO_4)_2$ was standardized against Mohr salt, and the exact formula weight of the Mohr salt is achieved from gravimetry (see section 3.1.2 for more details).

3.2.4 Magnetic properties

The low-to-room temperature (5K~300K) magnetic properties of RP3 oxides were determined using a “Magnetic Property Measurement System” (MPMS). This Quantum-designed instrument is based on a “Superconducting Quantum Interference Device” (SQUID). Measurements included in this work were: Magnetization Vs Temperature (particularly zero field cooled (ZFC) and field cooled (FC)); Magnetization Vs Field.

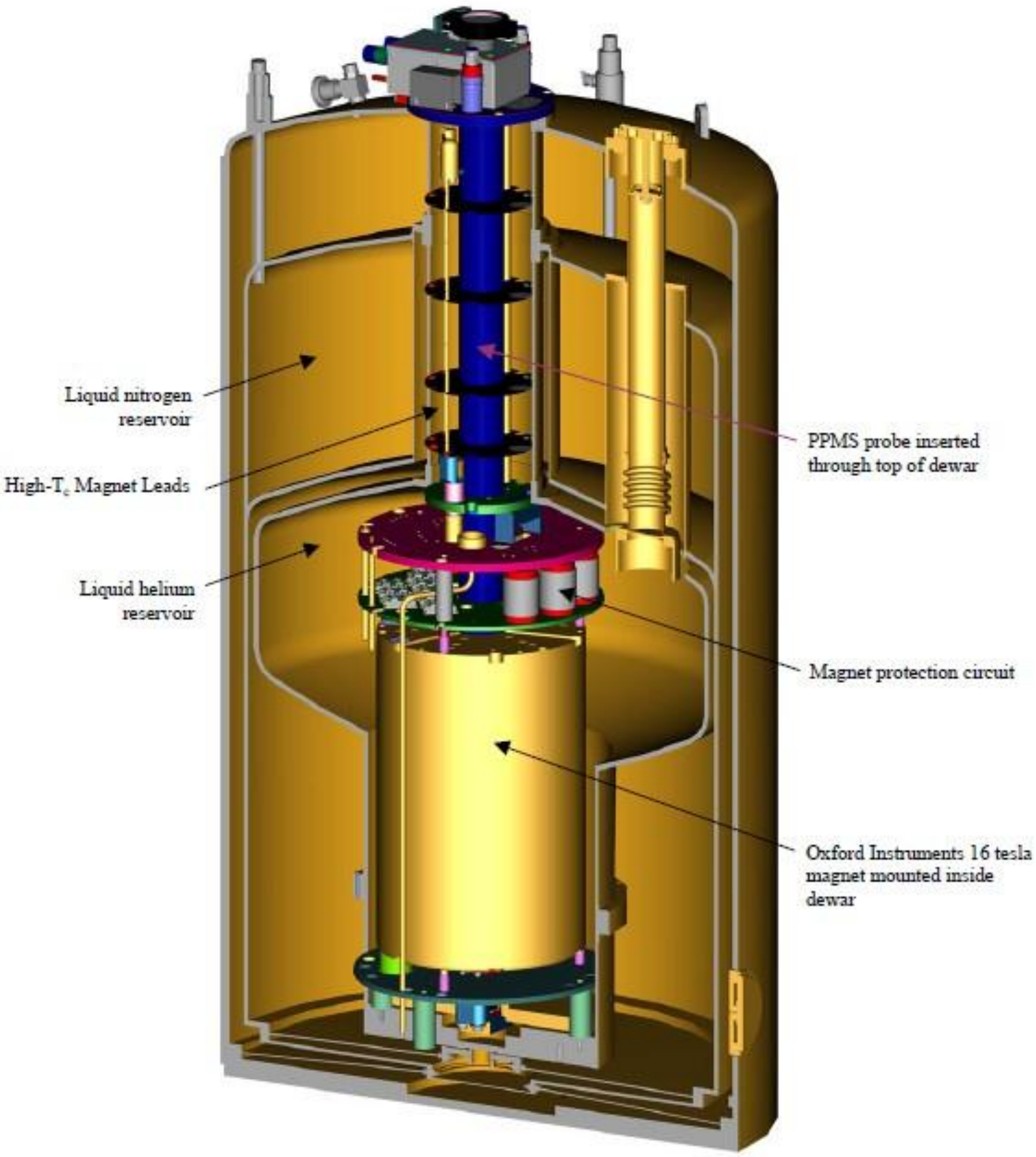

Figure 24. Cutaway view of PPMS-16, Quantum Design[86].

Figure 24 is a cutaway drawing of a PPMS presented, showing its main components. Moving a magnetized sample (up and down) through a coil of superconducting wire induces a voltage in the detection coil set. The amplitude of this signal is proportional to the magnetic moment and can be detected by the SQUID.

In the zero field-cooled experiment, the sample is cooled at low temperatures, usually 5K, and then the magnetization is monitored under an applied magnetic field as a function of temperature. In the field-cooled measurement, the sample is cooled down under an applied field from room temperature to low temperature and magnetization is monitored as the sample is warming up in field.

For the Magnetization-Field measurement, it is conducted at fixed temperature, ranging from 5 K to room temperature.

There are two ways of preparing the samples:

- For the high oxygen content samples ($\delta < 0.1$), the preparation starts with weighing around 50 mg powders. And filled around 50 mg powders in a capsule and tried to keep it fixed. Moreover, this capsule was loaded inside a plastic straw. To make it 100% fixed, some tapes were wound around the capsule to increase the diameter.
- Caution must be taken for the preparation of the oxygen deficient samples ($\delta > 0.1$). These samples were stored in glove box ($pO_2 \leq 6$ ppm, $H_2O \leq 1$ ppm). Loaded known amount of about 50 mg into a glass tube and used enough quartz wools to make the powders fixed at the bottom of the tube. Kept the tube airtight and took it outside of glove box. The tube was evacuated using a vacuum pump carefully. Vacuum was ascertained with a vacuum indicator, purple color was given for the pressure below 20 Torr. Then then tube was sealed in a H_2/O_2 torch. Same procedure was taken to load the closed tube inside a plastic straw.

3.3 Errors and uncertainties

Inevitably some errors and uncertainties are introduced more or less in the current experimental work. Thus it is necessary to reveal the main factors and if possible find measures to reduce or even eliminate errors and uncertainties.

During the synthesis, introduction of slight contamination of the samples might happen, as well may errors be introduced that affects the actual stoichiometry of the aimed products. When using the analytical balance, slight errors are estimated to ±0.0001g of weighing of the starting materials [87]. When transferring the weighed materials into the beaker, a very small amount may be lost due to stickiness to the weighing boat. However, these uncertainties are considered negligible.

There are several systematic errors in the XRD characterization. Firstly, there could be minor error in determination of each peak position over the entire measuring angles owing to zero point and height errors for the sample [88]. In addition, preferred orientation of the specimen may lead to some errors in the intensities for the XRD pattern. An internal Si standard was added into the specimen to minimize the systematic errors with respect to peak positions.

There exists variable factors attributing to errors in the cerimetric titration. Some treatments are carried out to minimize the errors, such as determining the practical formula weight of Mohr’ salt (see chapter 4.1) and the real molarity of $Ce(SO_4)_2$. Considering these factors together with the obtained results from each group of three parallel measurements, it is estimated that the real value of the oxygen content (10–δ) of the sample with a standard deviation ± 0.05 for $LnSr_3Fe_3O_{10-\delta}$ (Ln = La, Nd) series.

The obtained crystallographic data from the Rietveld refinement have certain errors limited by the quality of collected pattern. The obtained results were found to vary slightly with the refinement setting, such as 2θ range, presence of impurities etc. There exist larger challenges in fitting of SRXRD than lab XRD due to low background as well as a highly improved signal to noise ratio. This is of course beneficial with respect to quality of derived crystallographic data, however, it appeard more challenging to describe observed peak profiles correctly for the synchrotron XRD data.

For the thermogravimetry measurement, the buoyancy varies under different atmosphere and at different temperatures. The uncertainties of the thermo balance are ±0.05 mg that is too small to represent any real source of error. The weight and the style of amounting the sample could also be a source of error. Therefore, around 50 mg specimen are weighed and amounted. It is therefore necessary to measure a blank background of the crucible prior to the targeted measurement. However, such crucible calibration runs were not performed for all experiments.

The oxygen content is calculated via TGA method assuming that the oxygen stoichiometry of the post-TGA sample is $O_{9.90}$. This anticipated value is, however, quite rough due to many possible factors, i.e. the sample weight and how the sample is distributed in the crucible etc.

Some magnetization FC and ZFC curve were found to quite noisy. This is most likely due to a slight shift in sample position during measurement, i.e. on approaching room temperature. A given data point represent an average of 3-6 measurements, with typically a standard deviation $\sigma \approx 0.0005$ emu for the measured magnetization. The calculated Curie-Weiss temperature, u_{eff} and number of unpaired electrons depend on the quality of the fit of the temperature dependence of the inverse magnetic susceptibility to straight line in the paramagnetic region.

Chapter 4

Results

In this chapter will experimental results obtained in this study be presented and explained. In the first section are the results from the exact formula weight determinations of some of the starting materials used in the synthetic work and the cerimetric titration reported. The following section describes the compounds we attempted to obtain in this study together with their synthesis conditions. For the two phase-pure compounds $LaSr_3Fe_3O_{10-\delta}$ and $NdSr_3Fe_3O_{10-\delta}$, a wide series of oxygen deficient compositions were obtained by means of full oxidation at low temperatures, quenching from high temperatures and Zr-reduction. The oxidation state of the B-site cation (Fe) of fully oxidized-, as-synthesized- and reduced samples was thereafter determined by cerimetric titration and thermogravimetric analysis. Structural aspects of the fully oxidized and reduced samples were also evaluated with basis in collected XRD and SRXRD data using Rietveld refining programs as TOPAS. Finally, in the last subchapter are the magnetic susceptibility M(T) and hysteresis M(H) data of $LaSr_3Fe_3O_{10-\delta}$ and $NdSr_3Fe_3O_{10-\delta}$ presented.

4.1 Synthesis

4.1.1 Determination of formula weight of starting materials

In order to carefully control the exact addition of certain elements to a synthesis or as a titrant/reducing agent in the cerimetric titration, accurate formula weights of the starting materials must be determined. The real formula weights of specific starting materials were for the reason determined at the onset of the experiments by means of quantitative gravimetry. Other starting materials were used “as-received” or after a firing at high temperatures. Table 9 shows the experimentally determined formula weights of $SrCO_3$, $Fe(COO)_2 \cdot 2H_2O$ and $(NH_4)_2SO_4 \cdot FeSO_4 \cdot 6H_2O$. The reported values are the mean value of four parallels.

Table 9. Experimentally determined formula weights of some starting chemicals

Chemicals	Decomposed Oxides	Theoretical formula weight g/mol	Purity %	Determined formula weight g/mol	[1]Comparative ratio %
$SrCO_3$	SrO	147.63	> 98	145.9 ± 0.3	98.80
$Fe(COO)_2 \cdot 2H_2O$	Fe_2O_3	179.89	99	178.2 ± 0.6	99.04
$(NH_4)_2SO_4 \cdot FeSO_4 \cdot 6H_2O$	Fe_2O_3	392.14	99	391.8 ± 0.4	99.91

[1] Comparative ratio = Mean determined value / Theoretical number

The formula weight determinations were only conducted at the onset of usage. Each decomposed chemical listed in Table 9 were confirmed from XRD to only contain their expected corresponding oxides SrO and Fe_2O_3. (for equations and firing temperature, see section 3.1.3, Page 46). The powder X-ray diffraction patterns of the calcination products are presented in Appendix B (Page 126).

Experimental formula weights of each chemical show values similar to the theoretical values (obtained directly from the product information, as shown in Table 9). The XRD pattern of decomposed $SrCO_3$, only show presence of SrO. As the experimental formula weight of $SrCO_3$ is lower than the theoretical one it may imply that it contains small quantities of SrO_2 or $Sr(OH)_2$ (not detectable with XRD), which would lead to a lower formula weight.

The formula weight of $Fe(COO)_2 \cdot 2H_2O$ is also slightly lower than the theoretical one, and this is assumed to be due to loss of some crystal water. For the Mohr salt, the experimental formula weight is the same as the theoretical within uncertainty of the work. The values used in this work are the mean determined formula weights, reported in Table 9.

4.1.2 Synthesis conditions for $Ln_xSr_{4-x}Fe_3O_{10-\delta}$ (Ln = La, Nd)

Synthesis of new materials has long been recognized as the most essential element for chemists within the field of materials science. The discovery of new compounds have mostly happened serendipity, especially for the “first-discovery-structure” phases. However, the same methods make it possible to synthesize similar compounds taking same/similar crystal structure as the “first-discovery-structure” phases.

All the RP3 compounds being defined by the formulas $La_xSr_{4-x}Fe_3O_{10-\delta}$ and $Nd_xSr_{4-x}Fe_3O_{10-\delta}$, were made with the citric acid method. The heat treatment started with drying the sol-gel solution from the wet synthesis step at 180 °C overnight resulting in a fine powder that subsequently was calcined at 450 °C for 18-24 hours for every synthesis.

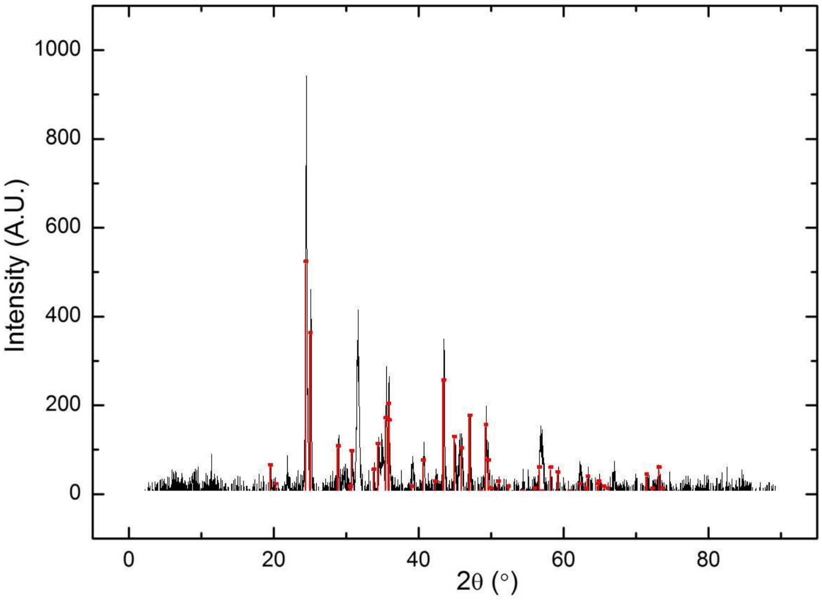

Figure 25. Powder X-ray diffraction pattern of fine $LaSr_3Fe_3O_{10}$ powder calcined at 450 °C for 18-24 hours. Powder X-ray diffraction pattern was collected using monochromatic Cu $K\alpha_1$ (λ = 1.540598 Å) radiation. Phase attribution: red vertical bars $SrCO_3$.

Figure 25 displays the XRD pattern of the fine powder obtained for $LaSr_3Fe_3O_{10}$, after being calcined at 450 °C overnight. The resulting compound shows presence of a large amount of strontium carbonate $SrCO_3$ together with a mixture of La-Sr-Fe-O and $La_2O_2CO_3$. The other samples synthesized in this work , most likely also contain carbonate containing phases after the step of calcining at 450 °C. Nature of the carbonates will most likely depend on x in the composition $Ln_xSr_{4-x}Fe_3O_{10-\delta}$ (Ln = La, Nd). The presence of $SrCO_3$ or other carbonates phases (e.g. $Ln_2O_2CO_3$, Ln = La, Nd) could make it difficult to form the desired RP3 phase, see section 5.1.1 on Page 104, discussion part.

The following annealing programs for $Ln_xSr_{4-x}Fe_3O_{10-\delta}$ (Ln = La, Nd) powders calcined at 450 °C are reported in Tables 10 and 11. The most common approach to develop optimal conditions for preparing phase pure compounds is to try different temperature-time-atmosphere firing condition. The annealing programs reported in Tables 10 and 11 are the recipies that gave the most well defined samples for the two series.

Table 10. Best conditions for synthesizing compounds in the La$_x$Sr$_{4-x}$Fe$_3$O$_{10-\delta}$ series

Compounds and its synthesis conditions[1]		Confirmation from XRD
x = 0.25	1000 °C×12 h followed by 1150 °C × 12 h × 2[2]	Close to pure phase RP2 phase and perovskite (see Figure 26 and Table 14)
x = 0.50	1000 °C × 12 h followed by 1150 °C × 12 h × 2	Close to pure phase RP2 phase and perovskite (see Figure 26 and Table 14)
x = 0.75	1000 °C × 12 h followed by 1200 °C × 12 h × 2	Pure phase (see Figure 26 and Table 14)
x = 1.0	1000 °C × 12 h followed by 1250 °C × 12 h × 2	Pure phase (See Figure 26 and Table 14 Appendix C.1 for details)
	1100 °C × 12h (Ar)× 2	
x = 1.25	1000 °C × 12 h followed by 1300 °C × 12 h × 2	Close to pure phase perovskite (See Appendix C.3 for details)
x = 1.5	1100 °C × 12 h (Ar) × 2	RP3 phase RP1 and Perovskite (See Appendix C.4 for details)
	1000 °C×12 h followed by 1150°C × 12 h × 2	
x = 2.0	1100 °C × 12 h (Ar) × 2	RP3 phase RP1 or RP2 Perovskite (See Appendix C.5 for details)
	1000 °C × 12 h followed by 1200 °C × 12 h × 2 or 1250 °C × 12 h × 2 or 1300 °C × 12 h × 2	
x = 3.0	1000 °C × 12 h followed by 1200 °C × 12 h × 2 or 1250 °C × 12 h × 2 or 1300 °C × 12 h × 2	RP3 phase RP1 or RP2 Perovskite (See Appendix C.6 for details)

[1] All starting materials are pellets of the powders calcined overnight at 450 °C. The heating and cooling speed is 5 °C/min. For the pure-phase (and close to) compounds, only successful synthesis conditions are shown.

[2] E.g. 1150 °C × 12 h × 2 means that the sample was fired in air at 1150 °C for 12 hours twice within one intermediate grounding and pelletizing.

Table 11. Best conditions for synthesizing compounds in the $Nd_xSr_{4-x}Fe_3O_{10-\delta}$ series

Compounds and its synthesis conditions[1]		Confirmation from XRD
x = 0.25	1000 °C × 12 h followed by 1300 °C × 12 h × 2[2]	Pure phase (see Figure 27 and Table 15)
x = 0.50	1000 °C × 12 h followed by 1300 °C × 12 h × 2	Close to pure phase RP2 phase and perovskite (see Figure 27 and Table 15)
x = 0.75	1000 °C × 12 h followed by 1300 °C × 12 h × 2	Pure phase (see Figure 27 and Table 15)
x = 1.0	1000 °C × 12 h followed by 1350 °C × 12 h × 2	Pure phase (see Figure 27 and Table 15)
x = 1.25	1000 °C × 12 h followed by or 1200 °C × 12 h × 2 or 1250 °C × 12 h × 2 or 1300 °C × 12 h × 2 or 1350 °C × 12 h × 2	RP3 phase RP1 Perovskite (See Appendix C.8 for details)
x = 2.0	1050 °C × 15 h followed by 1250 °C × 25 h or 1350 °C × 25 h or 1400 °C × 25 h or 1450 °C × 25 h or 1350 °C × 25 h and 1350°C × 24 h	RP3 phase RP1 Perovskite (See Appendix C.9 for details)
x = 3.0	1000 °C × 12 h followed by 1250 °C × 12 h × 2 or 1300 °C × 12 h × 2 or 1350 °C × 12 h × 2	RP3 phase RP2 Perovskite (See Appendix C.10 for details)

---

[1] All starting materials are pellets of the powders calcined overnight at 450 °C. The heating and cooling speed is 5 °C/min. For the pure-phase (and close to) compounds, only successful synthesis conditions are shown.

[2] E.g. 1300 °C × 12 h × 2 means that the sample was fired in air at 1300 °C for 12 hours twice within one intermediate grounding and pelletizing.

Our synthesis strategy was to start with $LaSr_3Fe_3O_{10-\delta}$ and $NdSr_3Fe_3O_{10-\delta}$ (i.e. x = 1.0 compositions), as recipes for these two phases already are reported in the literature [44, 56, 59]. Some of initial trial synthesis of $LnSr_3Fe_3O_{10-\delta}$ (Ln = La, Nd) was hydrated to some degree, most of these compounds were not phase pure, see Appendix C.2 (Page 128) and C.7 (Page 134). Ln-Sr-Fe-O RP3 phases tend to undergo hydration or carbonization reactions at ambient condition. The reactivity toward water and carbon dioxide is more aggressive for oxides with higher oxygen vacancy concentration $\delta \sim 1$ as water and carbon dioxide occupy the vacant sites in the structure [67].

Some measures were taken to conquer this trouble, i.e. pellets put into and/or taken out of furnace at annealing temperatures. These resulting as-synthesized and "quenched" samples produced in this work cover a range of oxygen vacancies ($\delta < 0.5$), see Table 13. This measures would accelerate the hydration or carbonization. Therefore, a dry preparation instead of using isopropanol for the XRD measurement was developed, see subchapter 3.2.1 on Page 49. The measurement was conducted right after finishing the preparation. In order to avoid further hydration or carbonization, the as-synthesized powder was stored in Schlenk tubes filled with Argon. The reduced powder was well kept in glove box ($pO_2 < 6$ ppm, $pH_2O < 1$ ppm).

Optimal synthesis conditions for $LaSr_3Fe_3O_{10-\delta}$ and $NdSr_3Fe_3O_{10-\delta}$ were found to be pelletizing powders (calcined at 450 ^{o}C overnight) and firing them at 1000 ^{o}C for 12 hours, followed by twice 12-hour annealings at 1250 ^{o}C ($LaSr_3Fe_3O_{10-\delta}$) and 1350 ^{o}C ($NdSr_3Fe_3O_{10-\delta}$) in air, respectively with intermediate grinding and pelleting. In addition, $LaSr_3Fe_3O_{10-\delta}$ was also successfully prepared as single phase was in an Ar atmosphere at 1100 ^{o}C (two firing steps of 12 hours periods each with intermediate grindings), refer to Appendix C.1 on Page 127 for XRD. Based on the optimized conditions and experience for the two x = 1.0 phases, the solid solution series were tried to be expanded in both directions; i.e. $0 < x < 4.0$.

Figures 26 and 27 are the powder X-ray diffractograms of the nominal compositions of the two series presented ($0 < x \leq 1.0$) together with its annealing temperature. The powder X-ray diffraction patterns present in both figures represent the most successful samples of these two series.

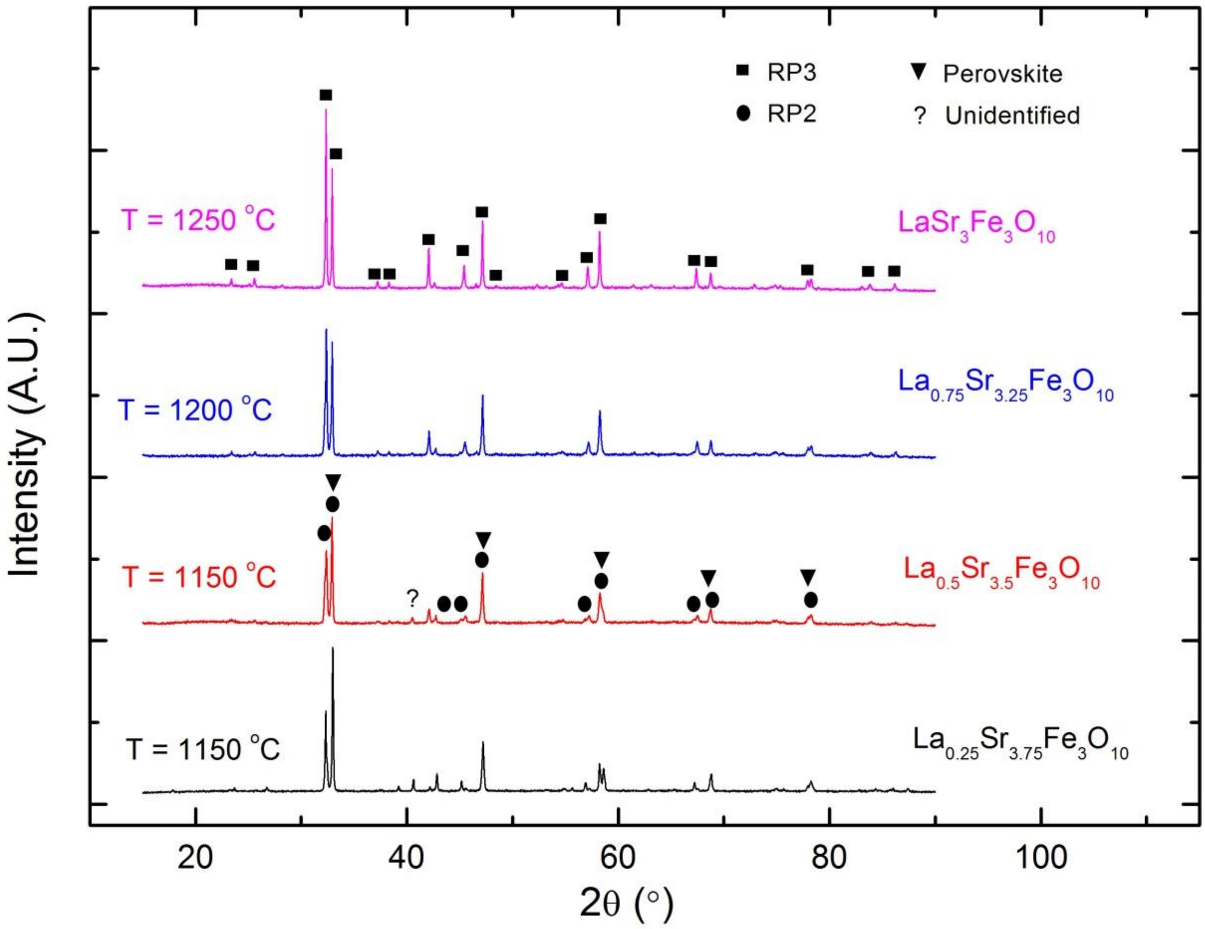

Figure 26. XRD patterns of the series $La_xSr_{4-x}Fe_3O_{10}$ for x = 0.25, 0.5, 0.75 and 1.0. Powder X-ray patterns were collected using monochromatic Cu $K_{\alpha1}$ (λ = 1.540598 Å) radiation.

Figure 26 displays the XRD patterns of $La_xSr_{4-x}Fe_3O_{10}$ (x = 0.25, 0.5, 0.75, 1.0) series compounds synthesized at different temperatures (for the refined data including phase fraction and evaluation factor, see Table 14 section 4.3). For x = 0.25 and 0.5, there is observed one small unidentified peak marked with "**?**" in the diffractograms. This small peak does not fit the diffraction pattern of any of RP phases and it also seems that the peak not can be ascribed to any other known phase. In EVA, there is not a PDF-card (Powder diffraction file) for $0 < x \leq 1.0$ in $La_xSr_{4-x}Fe_3O_{10}$. Specifically, the $LaSr_3Fe_3O_{10}$ and $La_{0.75}Sr_{3.25}Fe_3O_{10}$ crystallize in the RP3 structures ($Sr_4Fe_3O_{10-x}$). A large amount secondary phase (RP2, $Sr_3Fe_2O_7$ and perovskite) was found from the two XRD patterns in $La_{0.5}Sr_{3.5}Fe_3O_{10}$ and $La_{0.25}Sr_{3.75}Fe_3O_{10}$ compounds synthesized at 1150 °C.

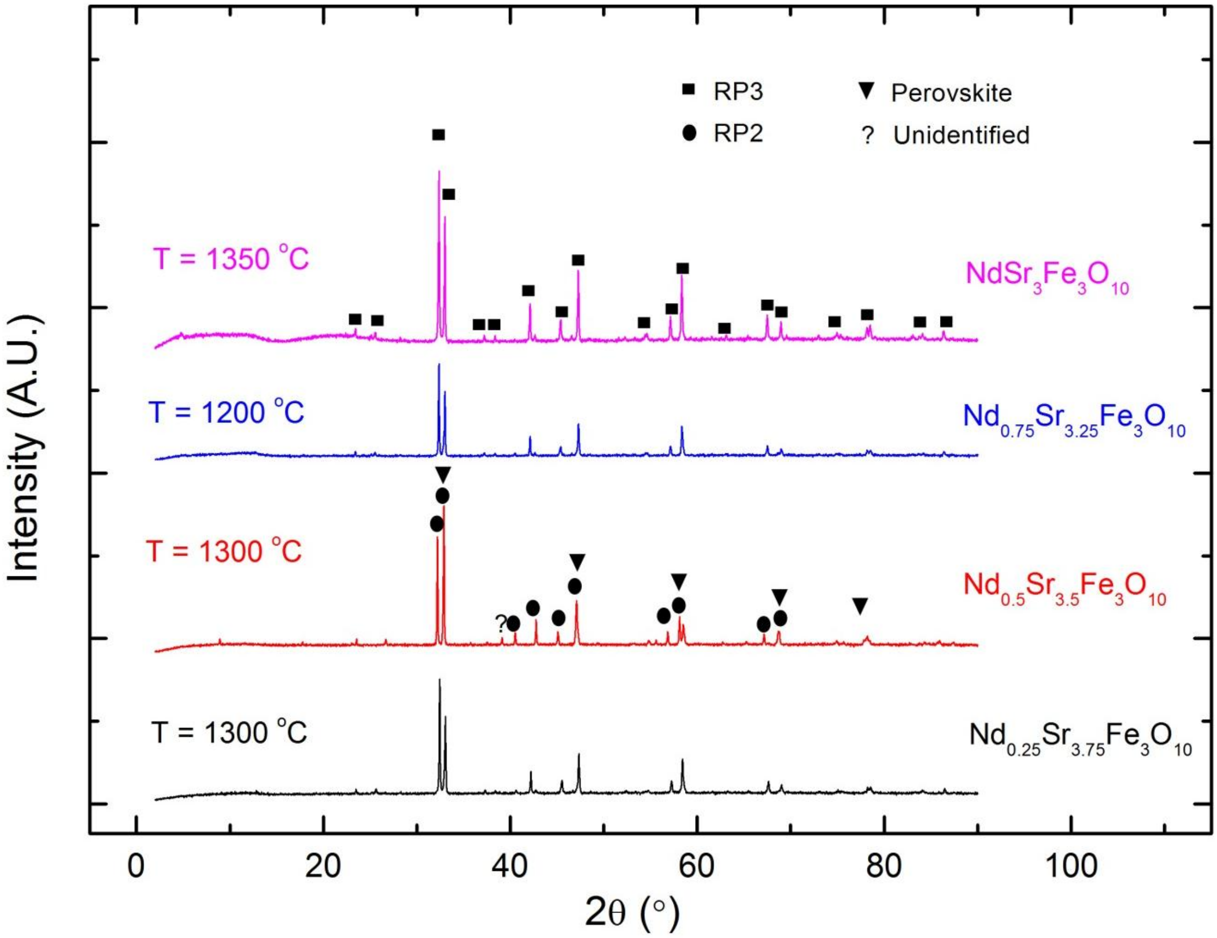

Figure 27. XRD patterns of the series $Nd_xSr_{4-x}Fe_3O_{10}$ series for x = 0.25, 0.5, 0.75 and 1.0. Powder X-ray patterns were collected using monochromatic Cu $K_{\alpha1}$ ($\lambda = 1.540598$ Å) radiation.

The collected powder X-ray diffraction patterns of $Nd_xSr_{4-x}Fe_3O_{10}$ series are shown in Figure 27 (for the refined data including phase fraction and evaluation factor, see Table 15, section 4.3). Powder X-ray analysis indicate that x = 0.25, 0.75, 1.0 members are phase pure. However, using the same sintering program as for the other members, the powder X-ray diffractogram of $Nd_{0.5}Sr_{3.5}Fe_3O_{10}$ sample includes some unexpected peaks of $SrFeO_3$ (perovskite) and $Sr_3Fe_2O_7$ (RP2 phase). The amount of the RP2 phase is most likely higher than that of perovskite, see Table 15 on Page 73, section 4.3.

To the best to our knowledge, recipies for making phase pure samples $La_{0.75}Sr_{3.25}Fe_3O_{10}$, $Nd_{0.75}Sr_{3.25}Fe_3O_{10}$ and $Nd_{0.25}Sr_{3.75}Fe_3O_{10}$ are reported for the first time in this study.

Attempt for expanding $Ln_xSr_{4-x}Fe_3O_{10-\delta}$ (Ln = La, Nd) series for $x > 1.0$ was conducted. Unfortunately, no single phase compounds were only proved. The synthesis conditions we used in this study and the results from the phase content analyses for these two series are summarized in Tables 10 and 11. For XRD and phase content analysis, see Appendixes C.3–6 (Pages 130-133) and C.8–10 (Pages 135-137). For both series, powder X-ray diffraction always showed presence of a RP2 $(Ln,Sr)_3Fe_2O_{7-\delta}$ or RP1 $(Ln,Sr)_2FeO_{4-\delta}$ type phases together with small quantities of a perovskite type phase $(Ln,Sr)FeO_{3-\delta}$. The main contaminants depend on the composition as well as annealing condition.

In the following experiments, we focused on the two phase-pure compounds $LaSr_3Fe_3O_{10-\delta}$ and $NdSr_3Fe_3O_{10-\delta}$.

4.2 Tuning of oxygen content in $LnSr_3Fe_3O_{10-\delta}$ (Ln = La, Nd)

To fill up the RP3 oxygen lattice to a value as close as possible to 10.00, the as synthesized powders were oxidized under a flow of oxygen at approximately 350 °C for 3 days. On the other hand, in order to obtain compounds with large oxygen deficiency ($\sim 0.5 < \delta < \sim 1.5$), the following two methods were applied in this work:

- “Quenching” method, by taking the sample out of the furnace at high temperature and allow it to cool down to ambient temperature in the desiccator.
- Reduction by Zr via the “chemical transport reaction” method.

The oxygen content of these obtained powders was subsequently determined with cerimetric titration method. The obtained oxygen contents are reported in Tables 12 and 13, where each reported value is the mean value obtained from the 3 parallel measurement. In addition, oxygen content of some selected compounds were checked by TGA, see Table 22 on Page 93, section 4.4.

An evaluation of the obtained oxygen contents of La and Nd ($Ln_xSr_{4-x}Fe_3O_{10-\delta}$) are described in section 4.2.1 and 4.2.2 whereas the results of corresponding evaluation of the XRD data is presented in section 4.2.3.

4.2.1 Oxygen content of $LnSr_3Fe_3O_{10-\delta}$ (Ln = La, Nd) prepared by the full oxidation and "quenching" method

The oxygen contents of fully oxidized- and as-synthesized $LnSr_3Fe_3O_{10-\delta}$ (Ln = La, Nd) as well as the powders obtained by quenching from high temperatures are reported with its quenching temperature (200, 1250 and 1350 °C) in Table 12.

Table 12. Oxygen-content of fully oxidized, as-synthesized and quenched sample

Post treatment		Fully oxidized	[1]As-synthesized	[2]200 °C	[2]1250 °C for La– series [2]1350 °C for Nd– series
Oxygen content $10-\delta$	$LaSr_3Fe_3O_{10-\delta}$	9.96 ± 0.01	9.93 ± 0.02	9.92 ± 0.01	9.76 ± 0.01
	$NdSr_3Fe_3O_{10-\delta}$	9.98 ± 0.01	9.87 ± 0.01	9.67 ± 0.02	9.55 ± 0.03

[1] As-synthesized samples were cooled down in the muffle furnace to ambient temperature with a rate of 5 °C/min. The pellets were crushed into powder and the cerimetric titrations were carried out right after.

[2] 200 °C, 1250 °C and 1350 °C means that the pellets were taken out of furnace at given temperature and cooled down to ambient temperature in desiccator where the pellets were crushed into powder immediately.

As illustrated in Table 12, cerimetric titration gave an oxygen content of $10-\delta = 9.96 \pm 0.01$ and 9.98 ± 0.01 for the fully oxidized $LaSr_3Fe_3O_{10-\delta}$ and $NdSr_3Fe_3O_{10-\delta}$ respectively. The obtained results are quite close to what Jantsky et al. published results ($10-\delta = 9.910(4)$ for the fully oxidized $PrSr_3Co_{1.5}Fe_{1.5}O_{10-\delta}$) [67]. The cerimetric titration of the former oxidized sample $LaSr_3Fe_3O_{10-\delta}$ was also conducted by Boklund [89], and she reported a similar result $10-\delta = 9.96 \pm 0.03$. For the as-synthesized $LaSr_3Fe_3O_{10-\delta}$ under Ar atmosphere, whose oxygen content was determined to be 9.92 ± 0.01 (not included to Table 12). This value is quite close to the as-synthesized sample cooling down (5 °C/min) in air.

Concerning as-synthesized sample and the sample being quenched to ambient temperature from 200 °C or even higher temperatures, $NdSr_3Fe_3O_{10-\delta}$ series shows larger oxygen deficiencies than that of $LaSr_3Fe_3O_{10-\delta}$ compounds. The range of oxygen content obtained from full oxidized-, as-synthesized and quenching methods lies in $10-\delta > 9.5$.

4.2.2 Oxygen content of $LnSr_3Fe_3O_{10-\delta}$ (Ln = La, Nd) prepared by Zr-reduction

$LnSr_3Fe_3O_{10-\delta}$ (Ln = La, Nd) do exist over a wide range of oxygen stoichiometries [15, 56]. Thus, the reduced oxides with lower oxygen content $\sim 8.5 < 10-\delta < \sim 9.5$ were prepared by the chemical transport reaction as described in detail in subchapter 2.2 (Page 2.2) and 3.1.5 (Page 48). Size of δ was tuned from added quantities of Zr and RP3 oxide (as-synthesized samples, the phase contents were conformed as phase pure RP3 by powder X-ray diffraction). In the reduction reactor, Zr and RP3 oxide were kept at 750 °C and 500 °C, respectively for 3 days. The reactor was opened in the glove box and the oxygen content of each reduced sample was subsequently determined by cerimetric titration.

Table 13. Oxygen content of $LnSr_3Fe_3O_{10-\delta}$ produced by Zr reduction

Sample	Oxygen content $10-\delta$				
$LaSr_3Fe_3O_{10-\delta}$	8.68 ± 0.01	8.81 ± 0.02	9.00 ± 0.03	9.25 ± 0.01	9.46 ± 0.02
$NdSr_3Fe_3O_{10-\delta}$		8.78 ± 0.01	9.00 ± 0.02	9.21 ± 0.01	9.39 ± 0.01

According to Table 13 the oxygen content of $LaSr_3Fe_3O_{10-\delta}$ and $NdSr_3Fe_3O_{10-\delta}$ were found to be in the range $0.54 \leq \delta \leq 1.32$ and $0.61 \leq \delta \leq 1.22$, respectively.

Figure 28 displays the mean value, maximum and minimum (calculated from titration) of each reduced oxide, in comparison with the theoretical value (calculated in advance assuming that Zr reacts completely with RP3 oxides).

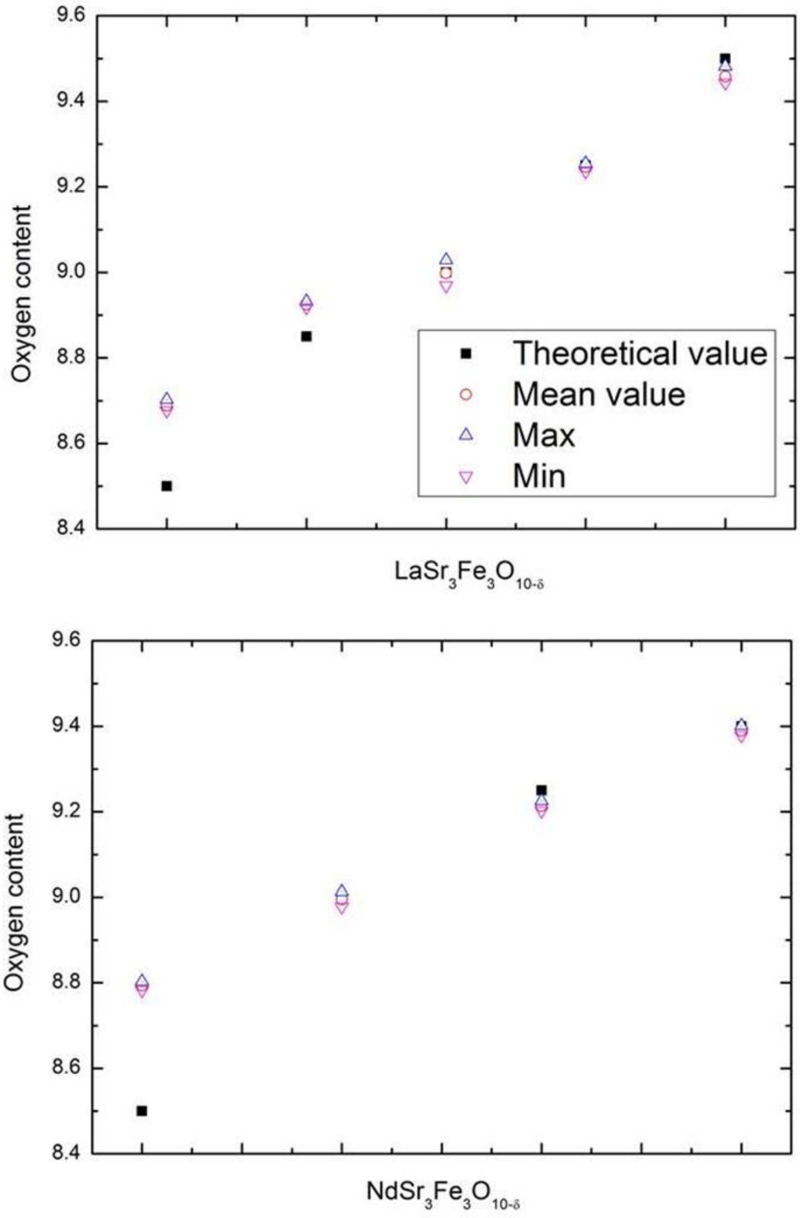

Figure 28. Maximum, minimum, average and theoretical value of the titration data

As shown, this method worked very well when the oxygen content was reduced to the range ~9.00 < 10–δ < 9.50. For the lower oxygen content (~8.50 < 10–δ < ~9.00), the real value deviated the calculated value for the oxide and Zr did not react completely (86.8% and 78.34% Zr were consumed to reduce as-synthesized $LaSr_3Fe_3O_{9.92}$ and $NdSr_3Fe_3O_{9.87}$ to $O_{8.69}$ and $O_{8.78}$ respectively). The approaches to higher oxygen deficiencies in RP3 oxides are presented in section 5.2.2 on Page 109, discussion.

For the following expression of the composition, the mean titrated data are donated the "real" value of the oxygen content. A discussion of the titrated values and the data calculated from TGA (section 4.4) is presented in section 5.2.1 (Page 109).

4.2.3 Powder XRD for the series $LnSr_3Fe_3O_{10-\delta}$ (Ln = La, Nd)

From Tables 12 and 13, it can be seen that a wide range of oxygen nonstoichiometries for the two series $LnSr_3Fe_3O_{10-\delta}$ (Ln = La, Nd) can be obtained using the oxidation-, quenching- and Zr-reduction method. For the La-series and the Nd-series the ranges are $8.68 \leq 10-\delta \leq 9.96$ and $8.78 \leq 10-\delta \leq 9.98$. Figures 29 and 30 display the powder X-ray diffraction patterns of these two series.

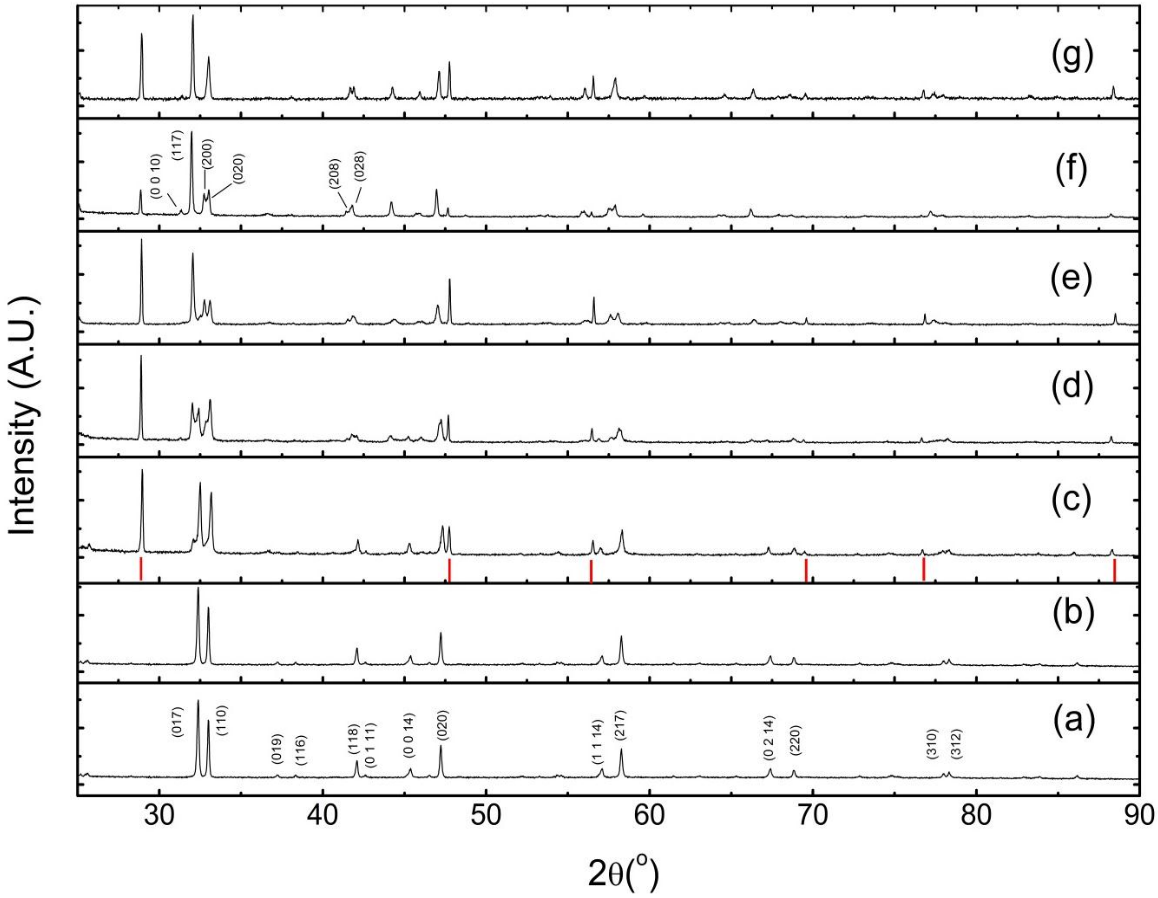

Figure 29. Powder X-ray diffraction patterns of $LaSr_3Fe_3O_{10-\delta}$ solid solution at room temperature. (a) Fully oxidized $LaSr_3Fe_3O_{9.96}$. (b) $LaSr_3Fe_3O_{9.76}$. (c) $LaSr_3Fe_3O_{9.46}$. (d) $LaSr_3Fe_3O_{9.25}$. (e) $LaSr_3Fe_3O_{9.00}$. (f) $LaSr_3Fe_3O_{8.81}$. (g) $LaSr_3Fe_3O_{8.68}$. Peaks denoted with vertical red bars (see ((c)) are due to Si internal standard. Miller indices are given for selected Bragg reflections in (a) and (f). Powder X-ray diffraction patterns were collected using monochromatic Cu $K_{\alpha 1}$ ($\lambda = 1.540598$ Å) radiation.

As can be seen from Figure 29, all the peaks of $LaSr_3Fe_3O_{9.96}$ (a) and $LaSr_3Fe_3O_{9.76}$ (b) can be ascribed to RP3 phase. The variation in oxygen stoichiometry ($10-\delta = 9.46, 9.25$) in the composition $LaSr_3Fe_3O_{10-\delta}$ leads to growth and disappearance of some peaks, these growth Bragg reflections comes from a $NdSr_3Fe_3O_9$ type phase. If the oxygen content in the samples are less than $O_{9.0}$ ($10-\delta$ = 9.00, 8.81, 8.68), the structure is the same as $NdSr_3Fe_3O_9$ [57]. For more details regarding the crystal structural analysis see section 4.3.

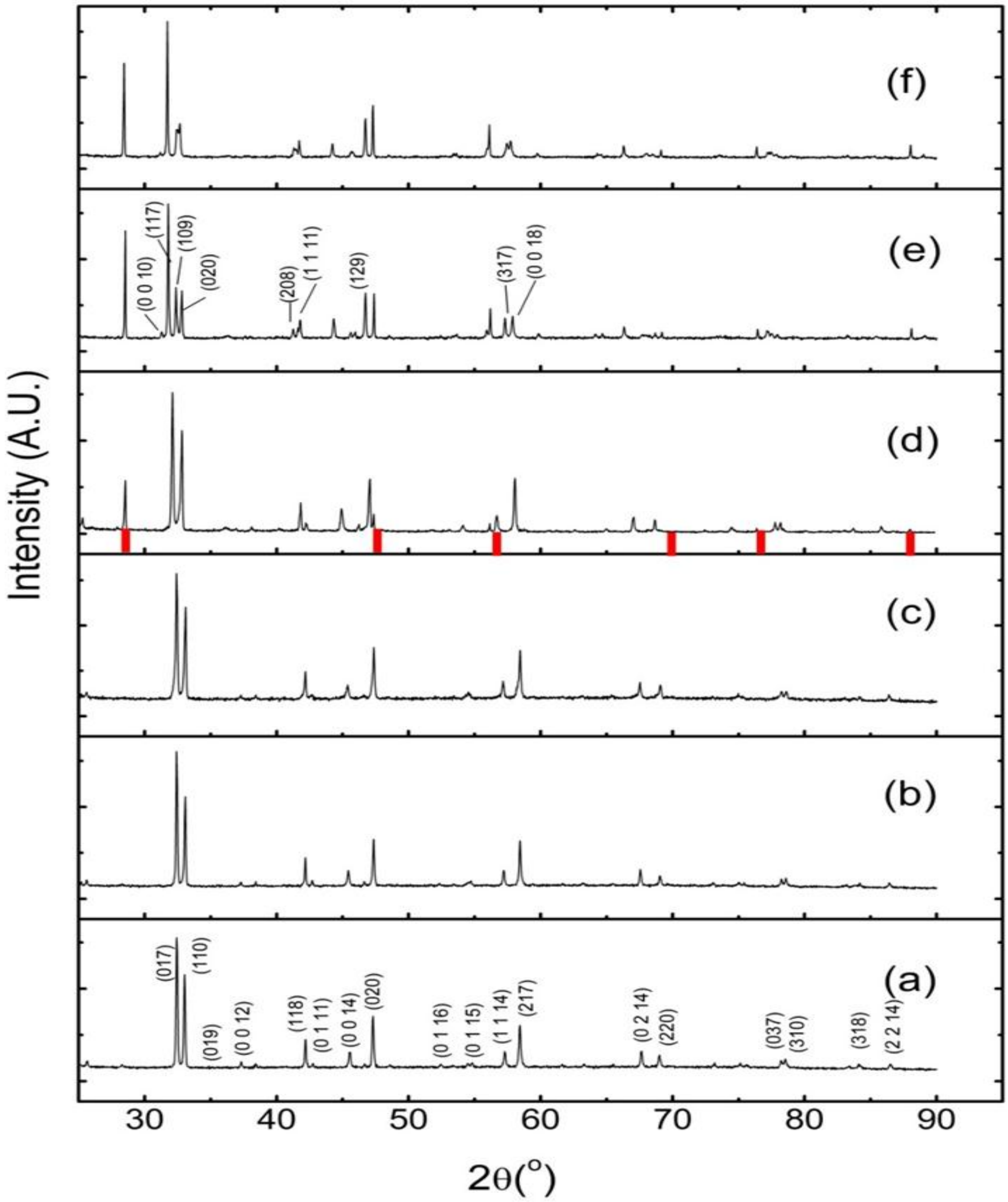

Figure 30. Powder X-ray diffraction patterns of $NdSr_3Fe_3O_{10-\delta}$ solid solution at room temperature. (a) Fully oxidized $NdSr_3Fe_3O_{9.98}$. (b) As-synthesized $NdSr_3Fe_3O_{9.87}$. (c) $NdSr_3Fe_3O_{9.39}$. (d) $NdSr_3Fe_3O_{9.21}$. (e) $NdSr_3Fe_3O_{9.00}$. (f) $NdSr_3Fe_3O_{8.78}$. Peaks donated with vertical red bars are due to Si internal standard. Miller indices given for selected Bragg reflection in (a) and (e). Powder X-ray diffraction patterns were collected using monochromatic Cu $K_{\alpha 1}$ (λ = 1.540598 Å) radiation.

As shown in Figure 30, powder X–ray diagrams for the $NdSr_3Fe_3O_{10-\delta}$ series are almost unchangeable for the composition $9.21 \leq 10-\delta \leq 9.98$ and these peaks were indexed with a tetragonal cell and space group I4/mmm, normally used for describing the tetragonal RP3 phases. $NdSr_3Fe_3O_{9.00}$ and $NdSr_3Fe_3O_{8.78}$ were found to be well described in an orthorombic supercell ($\sqrt{2}a_p \times \sqrt{2}a_p \times 28$ Å^3) crystallizing in the *Bbmm* space group. For more details regarding the crystal structural analysis see section 4.3

4.3 Crystal structure refinement

The lattice parameters of each of the fully oxidized, as-synthesized as well as reduced compounds were carefully determined by means of Profile fitting or by the Rietveld method of conventional X-ray diffraction and Synchrotron radiation X-ray diffraction data using the program TOPAS. Among the various possibilities of RP3 phases found in ICSD database, the $LaSr_3Fe_3O_{9.9}$ (Ccode: 72608), $LaSr_3Fe_3O_{9.52}$ (Ccode: 72609) and $NdSr_3Fe_3O_9$ (Ccode: 172509) were considered as the best choice staring parameters on the basis of atomic structure considerations.

4.3.1 $Ln_xSr_{4-x}Fe_3O_{10-\delta}$ (Ln = La, Nd; $0 < x \leq 1.0$) series

It is highly relevant to calculate how the lattice parameters vary with different A-site cations in the RP3 compounds. These parameters were obtained by Rietveld refinements of the conventional X-ray diffraction data of the as-synthesized samples (without silicon as standard) using the software TOPAS.

As earlier works show, the $Ln_xSr_{4-x}Fe_3O_{10-\delta}$ (Ln = La, Nd; $0 < x \leq 1.0$) series most probably adopt the space group *I*4/mmm as $LaSr_3Fe_3O_{9.9}$ with lattice parameters, a = b ≈ 3.86 Å, c ≈ 28.00 Å for as-synthesized compounds [56]. The Rietveld refinements were carried out with the atomic positions of previously studied $LaSr_3Fe_3O_{9.9}$ [56]. For the A and B site, the occupancy of each atom was in accordance with the chemical formula. Based on the results from the titrated as-synthesized $LaSr_3Fe_3O_{10-\delta}$ with $O_{9.92}$, the oxygen content of each as-synthesized sample was fixed as $O_{9.9}$ per formula unit. The refined unit cell parameters together with their refinement evaluation factor (R-factors) are given in Tables 14 and 15 for these two series $La_xSr_{4-x}Fe_3O_{10-\delta}$ ($0 < x \leq 1.0$) and $Nd_xSr_{4-x}Fe_3O_{10-\delta}$ ($0 < x \leq 1.0$) respectively.

Table 14. Refined lattice parameters, phase fraction and reliability factor of $La_xSr_{4-x}Fe_3O_{10}$ (x = 0.25, 0.5, 0.75, 1.0) series

$La_xSr_{4-x}Fe_3O_{10}$	Space group	Phase fraction	Unit cell parameters		*GOF*	R_{exp}	R_{wp}	R_p
			a = b	c				
x = 0.25	I4/mmm (RP3)	7.51%	3.868	28.271	1.77	3.19 %	5.65 %	3.82 %
	I4/mmm (RP2)	68.41%	3.870	20.170				
	Pervoskite	24.08%	3.873	3.873				
x = 0.5	I4/mmm (RP3)	69.33%	3.863	27.985	1.26	3.74%	4.72%	3.63%
	I4/mmm (RP2)	18.17%	3.867	20.181				
	Pervoskite	12.50%	3.872	3.872				
x = 0.75	I4/mmm (RP3)	100 %	3.865	27.999	1.73	3.71%	6.43%	4.55%
x = 1.0	I4/mmm (RP3)	100 %	3.867	28.059	1.32	3.76%	4.97%	3.83%
Published results	$LaSr_3Fe_3O_{9.9}$[1]		3.886	28.041	-	-	-	-
	$LaSr_3Fe_3O_{10}$[2]		3.87	28.03	-	-	-	-
	$LaSr_3Fe_3O_{9.9}$[3]		3.865	27.996	-	-	-	-

Note: The refinement was carried with 2θ ranging from 15° to 90°.

1 Lattice parameters for $LaSr_3Fe_3O_{9.9}$ are taken from Lee et al. [56]

2 Lattice parameters for $LaSr_3Fe_3O_{10}$ are taken from K. Kuzushita et al. [65]

3 Lattice parameters for $LaSr_3Fe_3O_{9.9}$ are taken from Cui et al. [90]

Table 15. Refined lattice parameters, phase fraction and reliability factor of $Nd_xSr_{4-x}Fe_3O_{10}$ (x = 0.25, 0.5, 0.75, 1.0) series

$Nd_xSr_{4-x}Fe_3O_{10}$	Space group	Phase fraction	Unit cell parameters (Å)		*GOF*	R_{exp}	R_{wp}	R_p
			a = b	c				
x = 0.25	I4/mmm (RP3)	100 %	3.855	27.998	1.25	5.03 %	6.27%	4.80%
x = 0.5	I4/mmm (RP3)	12.14%	3.875	26.990	1.28	4.83%	6.19%	4.60%
	I4/mmm (RP2)	70.54%	3.868	20.158				
	Pervoskite	17.31%	3.868	3.868				
x = 0.75	I4/mmm (RP3)	100 %	3.853	28.044	1.27	5.59%	7.09%	5.35%
x = 1.0	I4/mmm (RP3)	100 %	3.856	28.046	1.16	4.20 %	4.87 %	3.84 %

Note: The refinement was carried with 2θ ranging from 15° to 90°.

As can be seen in these two tables, the evaluation factor GOF, R_{exp}, R_{wp} and R_p suggest that the result is valid. The calculated unit cell parameters for $LaSr_3Fe_3O_{9.92}$ are a = b = 3.867 Å, c = 28.059 Å, these values agree with previously reported data, which depending on the synthesis conditions and the oxygen content of the sample lie in the range: a = b = 3.865 – 3.886 Å, and c = 27.996 – 27.041 Å [56, 65, 90].

More specifically, graphs were plotted with RP3 phase unit cell parameters as a function of x in the composition (see Figure 31) being in accordance with Tables 14 and 15, and for the powder X-ray diffraction patterns for these two series, see Figures 26 and 27 (Pages 63 and 64 respectively), in section 4.1.2.

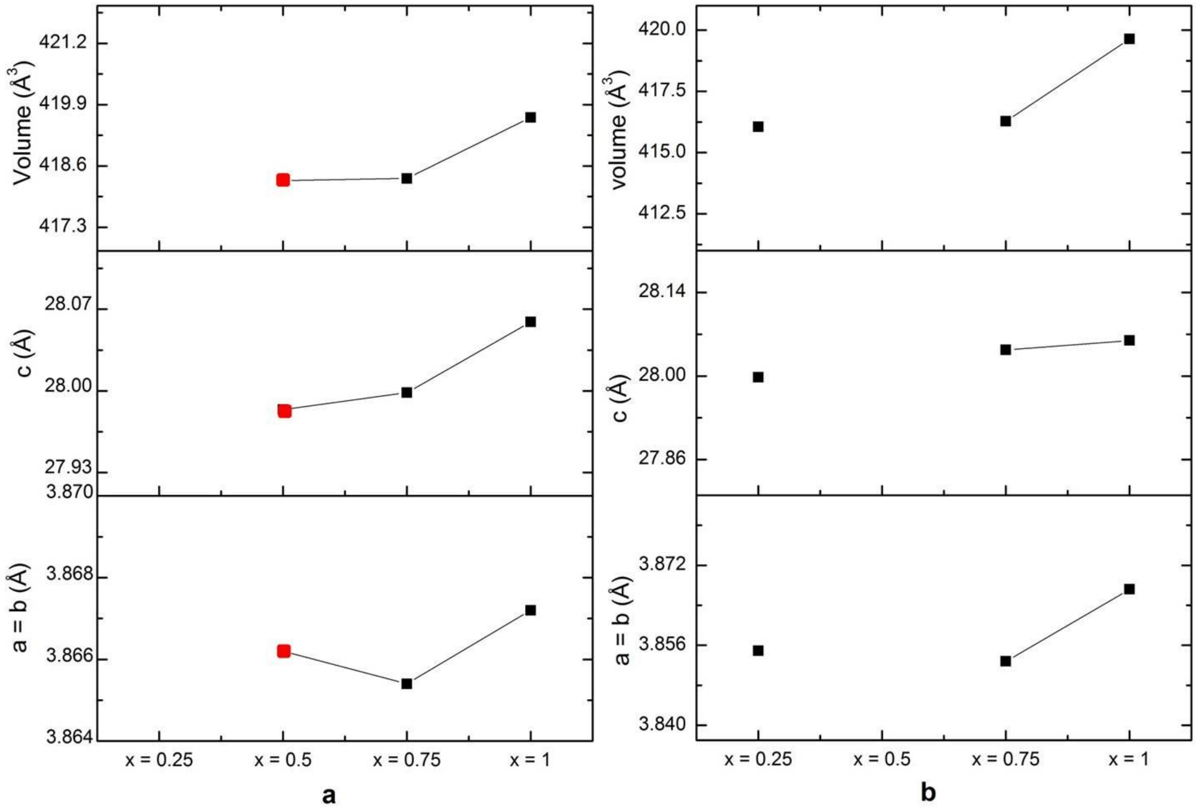

Figure 31. Unit cell parameter of the $Ln_xSr_{4-x}Fe_3O_{10}$ (x = 0.25, 0.5, 0.75, 1.0) series. (a) $La_xSr_{4-x}Fe_3O_{10}$ (x = 0.5, 0.75, 1.0) series. (b) $Nd_xSr_{4-x}Fe_3O_{10}$ (x = 0.25, 0.75, 1.0) series. Red filled square dots present the corresponding compound contains secondary phases.

As plotted in Figure 31, for phase pure compounds, a and b axis parameters of La– and Nd–series are in the range 3.850 – 3.870 Å while c axis parameters of these two series are in the range 27.999 – 28.059 Å and 27.998 – 28.046 Å respectively.

It should be pointed out that the real phase fraction of a mixture probably is not as the value given by TOPAS, there are many peaks overlapping thus it is not certain. For $La_xSr_{4-x}Fe_3O_{10}$ (x = 0.5), the refined lattice parameters of the RP3 phase are quite close to the value for x = 0.75, 1.0 composition, see red dots in Figure 31.a. TOPAS suggests that the main phase of sample $La_{0.5}Sr_{3.5}Fe_3O_{10}$ is RP3 structure with 18.17% RP2 phase and 12.50% perovskite phase as contaminant.

Large variation exists in the sample with high amount of secondary phase. As for $Nd_xSr_{4-x}Fe_3O_{10}$ (x = 0.5), the synthesized sample is a mixture of 12.14% RP3 phase, 17.31% perovskite phase and the main phase is RP2 $(Nd,Sr)_3Fe_2O_7$ phase. The calculated lattice parameter (see Table 15) for RP3 phase $Nd_{0.5}Sr_{3.5}Fe_3O_{10}$ deviates strongly with that of other phase-pure sample in $Nd_xSr_{4-x}Fe_3O_{10}$ (x = 0.25, 0.75, 1.0). The same phenomenon is observed in $La_xSr_{4-x}Fe_3O_{10}$ (x = 0.25), see Table 14 on Page 72. One reason is that the sample containing more than 50% secondary phases, the unit cell information seems less reliable. Moreover, the most likely reason is that these phases are of other structures.

4.3.2 $LnSr_3Fe_3O_{10-\delta}$ (Ln = La, Nd; $0 < \delta < 1.5$) series

The focus has been given to the composition $LnSr_3Fe_3O_{10-\delta}$ (Ln = La, Nd). Among these oxygen deficient $LnSr_3Fe_3O_{10-\delta}$ RP3 phases ($\sim 8.5 < 10-\delta < 10$), it is reported that the *I*4/mmm symmetry ($a_p \times a_p \times \sim 28$ Å^3, a_p is the parameter of the perovskite unit cell) of the $LaSr_3Fe_3O_{10-\delta}$ is retained for the reduced samples ($\sim 9.2 < 10-\delta < 9.9$) [56]. With larger oxygen deficiencies ($\delta \sim 1$), the phases have a reduced symmetry and are well described with $NdSr_3Fe_3O_9$ as an example from literature, with a distorted orthorhombic lattice [57]. The variation in the unit cell dimensions was currently evaluated for a supercell ($\sqrt{2}a_p \times \sqrt{2}a_p \times 28$ Å^3) crystallizing in the *Bbmm* space group.

4.3.2.1 Conventional XRD analysis

4.3.2.1.1 $LaSr_3Fe_3O_{10-\delta}$ ($8.68 \leq 10-\delta \leq 9.96$) series

The XRD patterns for $LaSr_3Fe_3O_{10-\delta}$ series ($\sim 8.68 \leq 10-\delta \leq 9.96$) were plotted in Figure 29. Meanwhile the Rietveld refinement was first carried out with fixed atomic positions according to the previous study ($LaSr_3Fe_3O_{9.9}$ [56] and $NdSr_3Fe_3O_9$ [57]). These two published atomic data were used to refine $LaSr_3Fe_3O_{10-\delta}$ ($\sim 9.2 < 10-\delta < 9.9$) and $LaSr_3Fe_3O_{10-\delta}$ ($8.68 \leq 10-\delta < \sim 9.2$), respectively.

The refinement is in very good agreement with expected results, especially when the oxygen stoichiometry is close to that of the earlier studied compounds (see Figure 32). The refined unit cell parameters and the reliability factors are illustrated in Table 16.

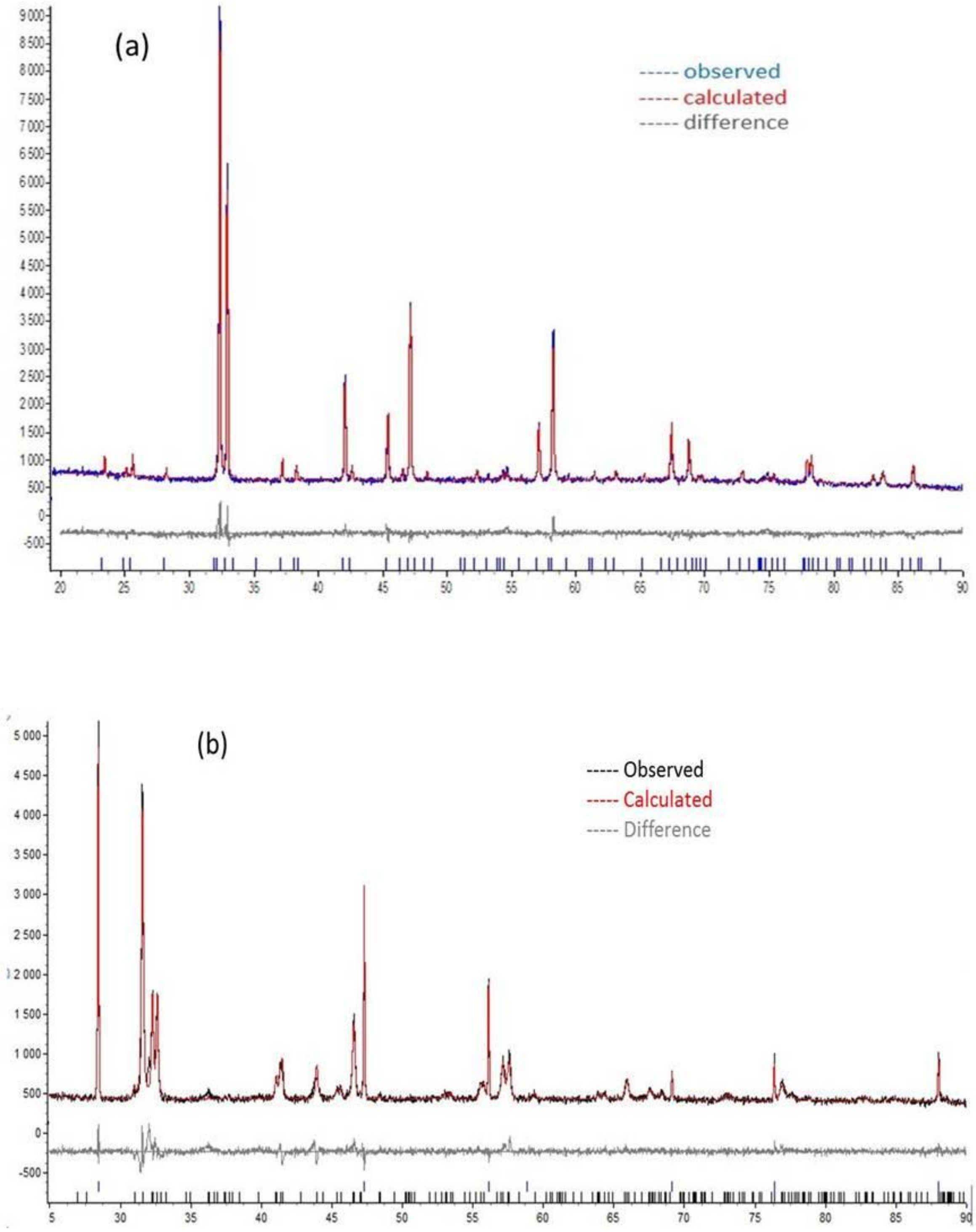

Figure 32. Refined pattern of the $LaSr_3Fe_3O_{10-\delta}$. The refinement was conducted in the 2θ range 26–90°. (a) $LaSr_3Fe_3O_{9.96}$. The vertical blue bars mark the Bragg peaks according to the I4/mmm space group. (b) Reduced sample $LaSr_3Fe_3O_{9.00}$. The vertical bars mark the Bragg peaks according to the Bbmm space group and the vertical blue ones mark the Silicon (internal standard) peaks. The grey line is the difference between the calculated pattern (red line) and observed pattern (blue line in a and black line in b).

Table 16. Refined lattice parameters and reliability factors for $LaSr_3Fe_3O_{10-\delta}$

Oxygen content 10-δ	Space group	Phase fraction	Unit cell parameters (Å)			*GOF*	R_{exp}	R_{wp}	R_p
			a	b	b				
9.96	I4/mmm	100 %	3.867	3.867	28.059	1.32	3.76%	4.97%	3.83%
9.76	I4/mmm	100 %	3.866	3.866	28.122	1.48	3.99%	5.9%	4.44%
9.00	Bbmm	100 %	5.541	5.485	28.835	1.83	4.52%	8.25%	6%
8.81	Bbmm	100 %	5.537	5.495	28.935	1.26	11.28%	1.42%	11.08%
8.68	Bbmm	100 %	5.501	5.501	28.946	1.09	8.76%	9.58%	7.61%

Note: Some patterns used Silicon as internal standard and the refined phase fraction only show the refined phases.

It is reported that $LaSr_3Fe_3O_{10-\delta}$ is of ideal I-type tetragonal RP3 structure without distortions even though the oxygen nonstoichometry is as high as δ~0.8 [56]. When the I4/mmm (RP3phase) was used to refine the $LaSr_3Fe_3O_{9.46}$ and $LaSr_3Fe_3O_{9.25}$, the refined pattern contains some extra peaks. As can be seen from the XRD pattern, some peaks grow (see Figure 29.c and d on Page 69) when the oxygen stoichiometry decrease to ~$O_{9.46}$ and ~$O_{9.25}$. These peaks can be ascribed to the reduced structure ($NdSr_3Fe_3O_9$), thus two structures were required to refine the two compounds two phases coexisting, see Table 17.

Table 17. Refined lattice parameters and reliability factors for $LaSr_3Fe_3O_{9.46}$ and $LaSr_3Fe_3O_{9.25}$

Sample	$LaSr_3Fe_3O_{9.46}$			$LaSr_3Fe_3O_{9.25}$		
Space group	I4/mmm	Bbmm	I/4/mmm	I4/mmm	Bbmm	I/4/mmm
Unit cell parameters (Å)	a = b = 3.878 c = 28.301	a = 5.497 b = 5.512 c = 28.838	a = b= 3.878 c = 28.307	a = b = 3.883 c = 28.367	a = 5.497 b = 5.513 c = 28.838	a = b = 3.888 c = 28.651
Phase fraction	79.19%	20.81%	100%	55.84%	44.16%	100%
GOF	1.3		1.52	1.48		2.12
R_{exp}	11.48%		11.50%	11.37%		11.40%
R_{wp}	14.96%		17.49%	16.86%		24.12%
R_p	11.82%		13.80%	13.34%		18.59%

The evaluation factors (R-values) show a major improvement for the refinement when these two compounds being refined with two phases. This is further obvious from visual inspection of observed, calculated and difference curve of the Rietveld refined fit, i.e. $LaSr_3Fe_3O_{9.46}$ see Figure 33.

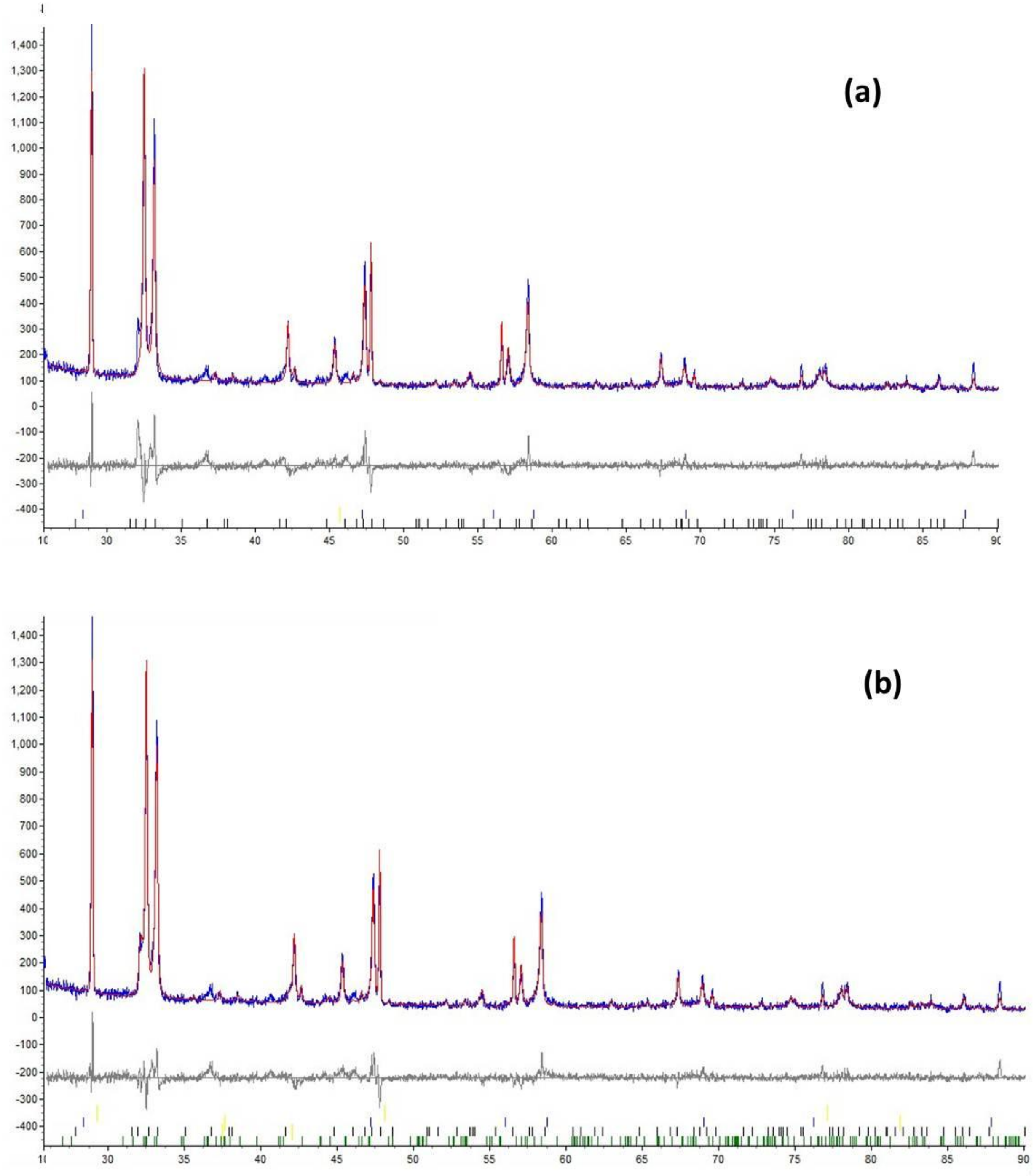

Figure 33. Refined XRD patterns for $LaSr_3Fe_3O_{9.46}$, silicon as internal standard. (a) The XRD pattern is the phase $LaSr_3Fe_3O_{9.46}$ refined by one structure ($LaSr_3Fe_3O_{9.9}$). (b) The XRD pattern is the phase $LaSr_3Fe_3O_{9.46}$ refined by two structures, $LaSr_3Fe_3O_{9.9}$ and $LaSr_3Fe_3O_9$.

The trend of lattice parameters for $LaSr_3Fe_3O_{10-\delta}$ as a function of oxygen content 10-δ is plotted in Figure 34 according to the data listing in Tables 16 and 17 on Page 77.

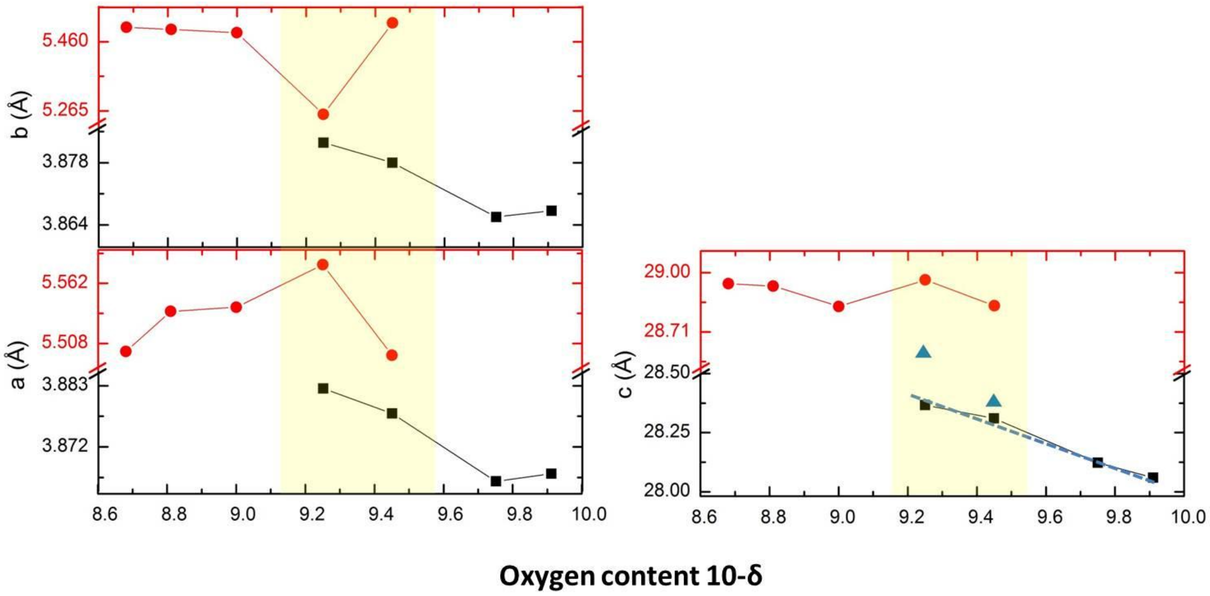

Figure 34. Lattice parameters for $LaSr_3Fe_3O_{10-\delta}$ as a function of oxygen content 10–δ. Red lines are unit cell parameters obtained by refining with Bbmm space group while black lines are from I4/mmm space group. Blue triangle dots are obtained via being refined this compound only using I4/mmm space group.

The unit cell parameters a and b for $LaSr_3Fe_3O_{10-\delta}$ series is slightly changing (less than 1.5% for single RP3 phase) with the oxygen stoichiometry. As it shows that Bbmm structure has the a and b axis parameters $\sqrt{2}$ times more than that of I4/mmm space groups, thus the red data in a and b unit cell dimensions is ~$\sqrt{2}$ times over the black data in Figure 34.a and b. A linear relationship between the c-axis parameter and oxygen content is obtained if the c parameter was obtained from the RP3 phase (see blue dashed line). This trend of c axis parameters matches the published results well.

Therefore, it is certain that the reduced compounds with oxygen content ranging from ~$O_{9.10}$ to ~$O_{9.50}$ (as yellow area shows in Figure 34) are two phases coexisting.

4.3.2.1.2 $NdSr_3Fe_3O_{10-\delta}$ ($8.78 \leq 10-\delta \leq 9.98$) series

As shown in Figure 30, the XRD diagram for the $NdSr_3Fe_3O_{10-\delta}$ series are almost unchangeable, adopting the I4/mmm space group even when the oxygen stoichiometry was reduced as low as $O_{9.21}$. Single-phase structure was used to refine unit cell dimensions from the XRD data. For the phase $O_{9.00}$ and $O_{8.78}$, the refinement were carried out with the atom position of $NdSr_3F_3O_9$ [57].

Table 18. Refined lattice parameters and reliability factors for $NdSr_3Fe_3O_{10-\delta}$

Oxygen content 10–δ	Space group	Unit cell parameters (Å)			Quality factor			
		a	b	c	*GOF*	R_{exp}	R_{wp}	R_p
9.98	I4/mmm (RP3)	3.855	3.855	27.972	1.29	3.86%	5%	3.84%
9.87	I4/mmm (RP3)	3.856	3.856	28.047	1.22	4.21%	5.13%	4.04%
9.67	I4/mmm (RP3)	3.854	3.854	28.051	1.3	3.9%	5.07%	3.9%
9.55	I4/mmm (RP3)	3.854	3.854	28.095	1.38	4.05%	5.56%	4.16%
9.39	I4/mmm (RP3)	3.860	3.860	28.204	1.39	13.77%	19.07%	14.44%
9.21	I4/mmm (RP3)	3.864	3.864	28.243	1.53	13.55%	20.76%	15.67%
9.00	Bbmm	5.538	5.468	28.630	1.38	4.27%	5.91%	4.41%
8.78	Bbmm	5.512	5.479	28.660	1.65	4.41%	7.29%	5.35%

Table 18 shows all the refined lattice parameters for this $NdSr_3Fe_3O_{10-\delta}$ series as well as its quality factors. The unit cell parameters of the composition $NdSr_3Fe_3O_{9.00}$ are slightly different from previous published data with a = 5.541 Å, b = 5.499 Å and c = 28.811 Å [57]. The dependence of the lattice parameters on the oxygen content are shown in Figure 35.

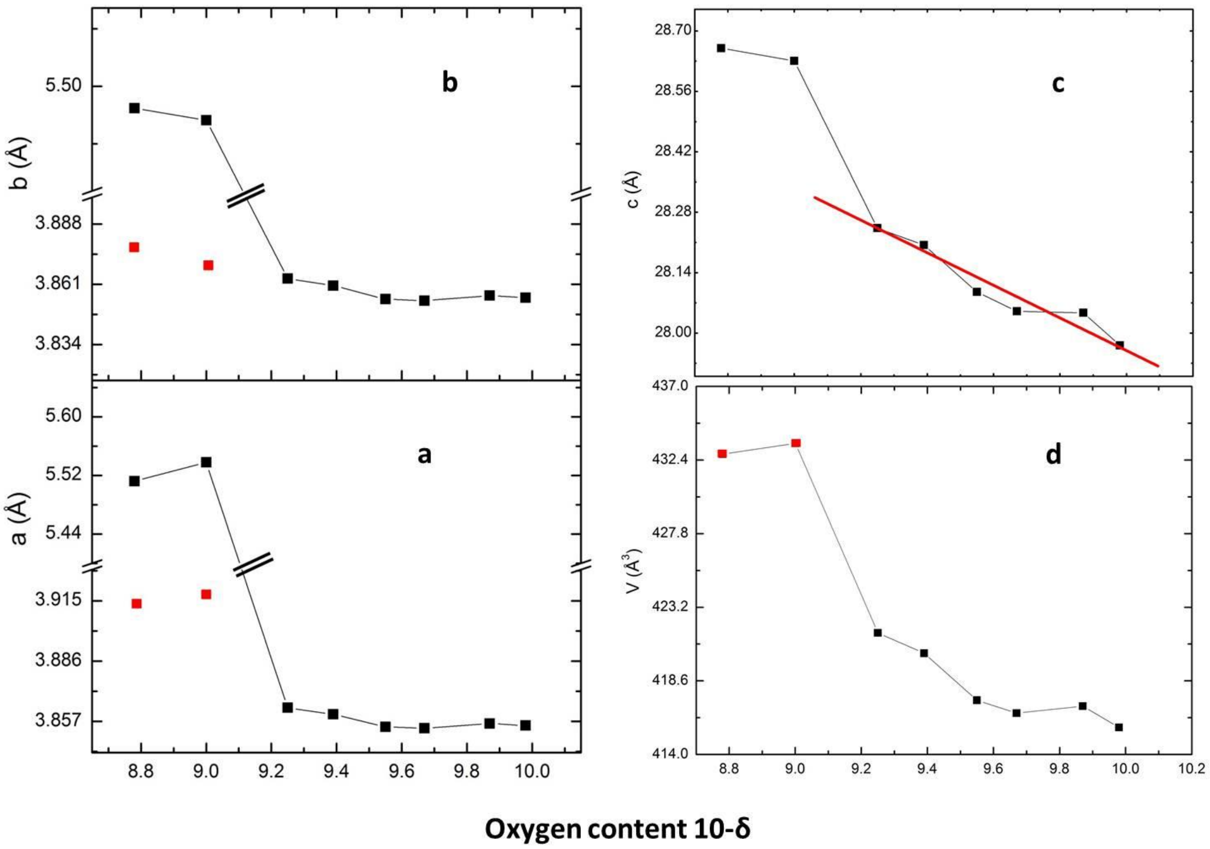

Figure 35. Lattice parameters for $NdSr_3Fe_3O_{10-\delta}$ as a function of oxygen content 10-δ. Red dot data in figure (a) and (b) are the value $\frac{a}{\sqrt{2}}$ and $\frac{b}{\sqrt{2}}$, where a and b are the refined value for the phase $NdSr_3Fe_3O_{9.00}$ and $NdSr_3Fe_3O_{8.78}$, while red data in figure (c) are the volume $\frac{V}{2} = \frac{a \times b \times c}{2}$, where unit cell parameter are for the phase $NdSr_3Fe_3O_{9.00}$ and $NdSr_3Fe_3O_{8.78}$.

It is shown that a- and b- axis parameters slightly increase in the range 3.855–3.905 Å with less oxygen content in these two phases. However, it shows a linear relationship between c parameters and oxygen stoichiometry in the I-type structure (see red trend line in Figure 35.c). Specifically, c-axis parameters decrease linearly from 28.243 Å to 27.972 Å when the phase containing $O_{9.21}$ is oxidized to $O_{9.98}$. The c parameter of ideal I-type RP3 structure is smaller than that of distorted orthorhombic lattice.

The calculated volume of this series also increases with less oxygen content (10–δ) in the composition $NdSr_3Fe_3O_{10-\delta}$. This phenomenon is expected since the oxidation state is higher for I-type than for the reduced orthorhombic.

4.3.2.2 Synchrotron XRD analysis

Some selected samples were analyzed with Synchrotron radiation XRD to investigate the atomic position, oxygen vacancies as well as interatomic bond lengths as a function of the oxygen stoichiometry.

4.3.2.2.1 $LaSr_3Fe_3O_{10-\delta}$ (10–δ = 9.96, 8.68) series

It is found that some weak peaks near 10.4^o (see Figure 36, red circle) and 13.5^o (see Figure 36, blue circle) in the SRXRD pattern due to the second phases. K.Kuzushita [65] ascribed these peaks correspond to $SrFeO_3$ and RP1 phase ($LaSrFeO_4$), respectively. Thus, perovskite, RP1, RP2 as well as other possible phases in composition (La-Sr-Fe-O) were attempted included in order to refine this pattern. No single phase could fit all these observed peaks. However, intensities of these two peaks were so weak that they were ignored for the structure analysis.

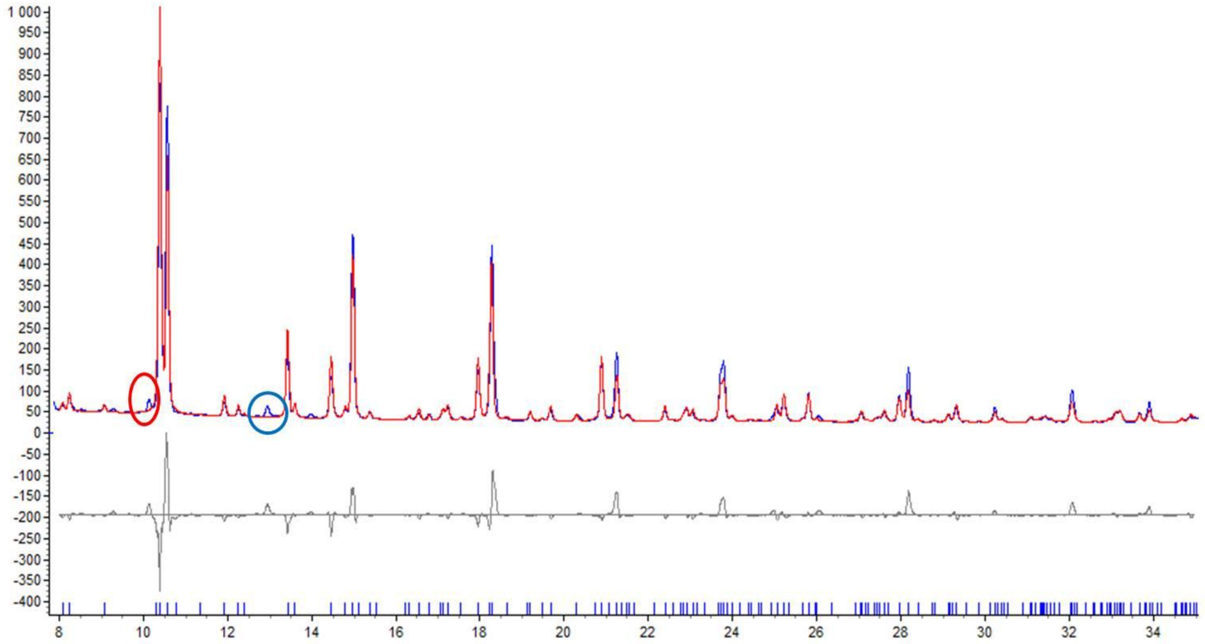

Figure 36. SRXRD pattern of Rietveld refinement of $LaSr_3Fe_3O_{9.96}$. The refinement was carried out in the range 2θ = 8–35^o. Powder X-ray patterns were collected using monochromatic Cu $K_{\alpha 1}$ (λ = 1.540598 Å) radiation. Space group I4/mmm, a = b = 3.872 Å, c = 28.063 Å, GOF = 0.88, R_{exp} = 14.12%, R_{wp} = 12.37%, R_p = 8.42%.

The atomic positions, occupancy and thermal parameters for $LaSr_3Fe_3O_{9.92}$ and $LaSr_3Fe_3O_{8.68}$ obtained from the Rietveld refinement are summarized in Table 19.

Table 19. Refined atomic coordinates and thermal parameters from SRXRD data for $LaSr_3Fe_3O_{9.96}$ and $LaSr_3Fe_3O_{8.68}$ at room temperature

Site	Atom	x	y	z	Occupancy	Beq
$LaSr_3Fe_3O_{9.96}$						
B1	Fe$^{+3.67}$	0	0	0	1	0.002
B2	Fe$^{+3.67}$	0	0	0.1406	1	0.002
A1	La^{+3}	0	0	0.5692	0.25	0.323
	Sr^{+2}	0	0	0.5692	0.75	0.323
A2	La^{+3}	0	0	0.7007	0.25	0.323
	Sr^{+2}	0	0	0.7007	0.75	0.323
O1	O^{-2}	-0.5	0.0661	0.1362	1	1.171
O2	O^{-2}	0	0	0.0646	1	1.171
O3	O^{-2}	0	0	0.2110	1	1.171
O4	O^{-2}	0.1291	0	-0.0178	0.91	1.171
Space group I4/mmm, a = b = 3.872 Å, c = 28.063 Å						
GOF = 0.88, Rexp = 14.12%, Rwp = 12.37%, Rp = 8.42%						
$LaSr_3Fe_3O_{8.68}$						
B1	Fe$^{+2.79}$	0.2700	0.7504	0.1469	1	0.015
B2	Fe$^{+2.79}$	0.2635	0.7376	0.0102	1	0.015
A1	La^{+3}	-0.2493	0.7139	0.2009	0.25	0.885
	Sr^{+2}	-0.2493	0.7139	0.2009	0.75	0.885
A2	La^{+3}	-0.2506	0.71560	0.0794	0.25	0.885
	Sr^{+2}	-0.2506	0.7160	0.0794	0.75	0.885
O1	O^{-2}	0.1799	0.3515	0.1489	0.90	0.212
O2	O^{-2}	0.4108	0.9685	0.1320	0.67	0.212
O3	O^{-2}	0.2153	0.8316	0.1977	1	0.212
O4	O^{-2}	0.2246	0.7827	0.0570	1	0.212
O5	O^{-2}	0.3543	0.1368	0	1	0.212
Space group: Bbmm, a = 5.515 Å, b = 5.503 Å, c = 28.905 Å						
$GOF = 0.84, R_{exp} = 14.12\%, R_{wp} = 11.89\%, R_p = 8.64\%$						

These data agree well with those published $LaSr_3Fe_3O_{9.96}$ (Ccode: 72608) [56] and $NdSr_3Fe_3O_9$ (Ccode: 172509) [57] respectively, see Tables 5 and 6 on Page 17, subchapter 1.5.1. Nevertheless, it should be noted that the result from the Rietveld refinement reveal information about the crystal structure, but limited by the quality of SRXRD pattern. In practice, the uncertainty of thermal parameters might be large, i.e. Fe ion on the B site. For the $LaSr_3Fe_3O_{8.68}$ specimen, the oxygen vacancies in the distorted orthorhombic structure are mainly located on the O2 site of the equatorial layer between the perovskite slabs.

4.3.2.2.2 $NdSr_3Fe_3O_{10-\delta}$ ($9.00 \leq 10-\delta \leq 9.87$) series

The unit cell parameters, oxygen occupancy, bond length and bond valence sum (BVS) in the series $NdSr_3Fe_3O_{10-\delta}$ ($10-\delta$ = 9.00, 9.21, 9.39, 9.67, 9.87) were investigated by means of SRXRD. Some weak extra peaks exist in the SRXRD patterns in this series; however, endeavor of ascribing these low intensity peaks failed.

Table 20. Refined data for $NdSr_3Fe_3O_{10-\delta}$ series obtained from SRXRD patterns

Oxygen content 10-δ	Lattice parameters			Quality factor			
	a = b (Å)	c (Å)	V ($Å^3$)	*GOF*	R_{exp}	R_{wp}	R_p
9.87	3.857	27.980	416.235	0.64	15.49%	9.92%	6.9%
9.67	3.860	28.073	418.285	0.71	14.97%	10.58%	7.25%
9.39	3.865	28.215	420.927	0.89	13.97%	12.46%	8.6%
9.21	3.862	28.243	421.144	1.42	13.66%	19.45%	11.74%
Space group I/4mmm							
9.00	a = 5.539 b = 5.471	28.637	867.812	0.49	14.32%	6.96%	5.01%
Space group Bbmm							

The refinement was carried out in the range 2θ = 8 - 36°

The lattice parameters and quality factors for $NdSr_3Fe_3O_{10-\delta}$ ($10-\delta$ = 9.00, 9.21, 9.39, 9.67, 9.87) are listed in Table 20. When compared these data being refined with XRD and SRXRD data, in Tables 18 (Page 80) and 20 respectively. They both show the same unit cell parameters apart from that SRXRD have larger qualify factor.

It is evidenced that the oxygen vacancies in these tetragonal phases are predominantly located to the FeO_2 layers in the middle of the triple perovskite block [56, 91]. The occupancy of O1, O2 and O3 site as well as B site was fixed at 1.0. Due to similar scattering lengths for La Nd and Sr, the composition ratio was not refined and was fixed to 0.25/0.75 as the known composition.

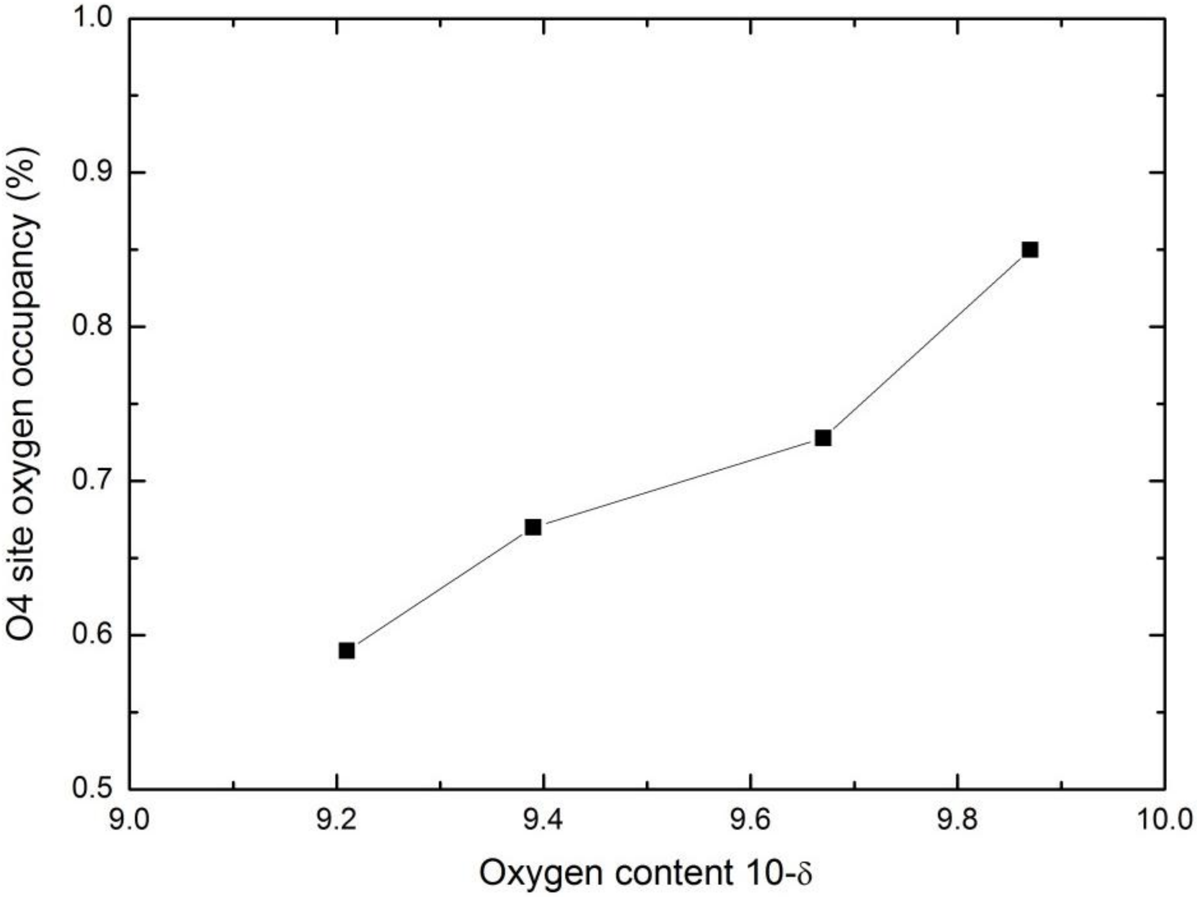

Figure 37. Refined O4 occupancy as function of oxygen content ($9.21 \leq 10–\delta \leq 9.87$). The occupancy of O1, O2 and O3 site was fixed at 1.0.

The refined occupancy of O4 site is decreasing stably from 85% to 59% for the phase $O_{9.87}$ and $O_{9.21}$, as shown in Figure 37. It is noticeable that the TOPAS software has certain errors. With lower oxygen occupancy on the O4 site, the hypothetical compound $LnSr_3Fe_3O_9$ might have a structure in which two octahedral layers are connected by a tetrahedral layer.

Table 21. Selected interatomic bond length (Å) and angles (°) resulting from Rietveld refinement of SRXRD data of various $NdSr_3Fe_3O_{10-\delta}$ compounds

Composition	$NdSr_3Fe_3O_{10-\delta}$						
Oxygen content 10-δ	9.87	9.67	9.39	9.21	9.00		
Space group	I4/mmm				Bbmm		
Bond	Bond length (Å)					Bond	Bond length (Å)
(Fe1-O2) × 2	1.892	1.855	1.768	1.778	Tetrahedra	(Fe2-O4) × 2	1.736
(Fe1-O4) × 2	1.854	1.952	1.753	1.626		Fe2-O5	1.875
(Fe1-O4) × 2	2.012	1.963	2.113	2.283		Fe2-O5	2.101
(Fe2-O1) × 2	1.930	1.925	1.904	1.933	Octahedra	(Fe1-O1) × 2	1.956
(Fe2-O1) × 2	1.931	1.939	1.970	1.937		(Fe1-O2) × 2	1.960
Fe2-O2	2.026	2.096	2.241	2.243		Fe1-O3	1.979
Fe2-O3	2.016	1.993	2.005	1.959		Fe1-O4	2.495
(La/Sr1-O1) × 2	2.694	2.693	2.651	2.655		(La/Sr1-O1) × 2	2.674
(La/Sr1-O1) × 2	2.728	2.694	2.689	2.675		(La/Sr1-O2) × 2	2.735
(La/Sr1-O2) × 4	2.728	2.731	2.744	2.744		La/Sr1-O3	2.383
(La/Sr1-O4) × 2	2.615	2.507	2.748	2.601		La/Sr1-O3	2.726
(La/Sr1-O4) × 2	2.664	2.548	2.752	2.695		La/Sr1-O3	2.848
						(La/Sr1-O3) × 2	2.753
						(La/Sr2-O1) × 2	2.584
(La/Sr2-O1) × 2	2.623	2.643	2.633	2.651		(La/Sr2-O2) × 2	2.559
(La/Sr2-O1) × 2	2.658	2.643	2.671	2.675		La/Sr2-O4	2.591
(La/Sr2-O3) × 4	2.743	2.744	2.751	2.749		(La/Sr2-O4) × 2	2.805
La/Sr2-O3	2.419	2.435	2.410	2.399		La/Sr2-O4	3.078
						(La/Sr2-O5) × 2	2.472
Bond	Bond angle (°)						
O2-Fe1-O2	180	180	180	180			
O4-Fe1-O4	87.64	86.79	87.47	87.88			
O4-Fe1-O4	93.96	93.21	92.52	92.12			
O1-Fe2-O1	88.48	89.82	88.18	88.93			
O1-Fe2-O1	91.52	93.13	91.24	90.55			
O2-Fe2-O3	180	180	180	180			

The bond lengths and bond angles from the SRXRD refinement are shown in Table 21, these data are in agreement with published results [56]. The bond length and angle between cation (La/Sr, Fe) and O4 site anion significantly changes and strongly depends on the oxygen content. The apical Fe1-O2 bond lengths are significantly shorter than the equatorial values (Fe2-O2/O3).

Along the stacking direction c, the Fe1-O2 bond length of the apical octahedra decrease from 1.892 Å to 1.778 Å for the phase $O_{9.87}$ and $O_{9.21}$, and the Fe2-O2 bond length of the equatorial octahedra increase from 2.026 Å to 2.243 Å respectively for the two phases. Interestingly, the other bond length of Fe2-O3 in the equatorial octohedra is stable around 2 Å.

The (La/Sr)1 is in a dodecahedral site with relatively stable values except the bond with O4 site, depending on the oxygen vacancies. The other (La/Sr)2 is in ninefold coordination, a monocapped square antiprism with oxygen bond distances varying from 2.410 to 2.751 Å.

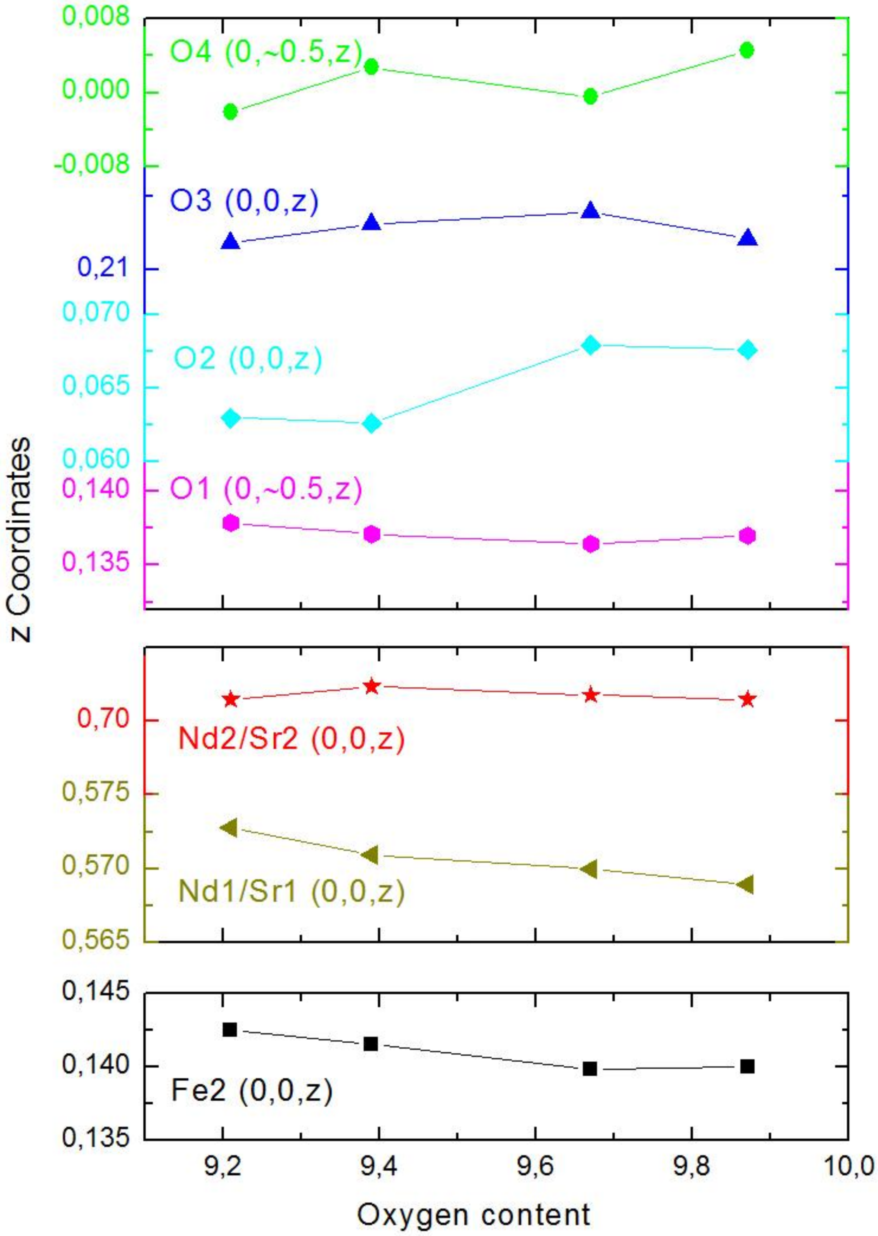

Figure 38. Variation of z fractional coordinates with oxygen content. Fe1 is fixed at the origin (0,0,0).

As shown in Figures 34 and 35 (Pages 79 and 81 respectively), the variation of c-axis increases linearly with the oxygen nonstoichometry of the sample. This phenomenon can be evidenced by the fact that the z fractional coordinates of cation increase slightly with the nonstoichometry.

Brown and Altermatt proposed the term Bond Valence Sum (BVS) [92, 93], which can be calculated by the following equation for all the cation sites:

$$\boldsymbol{V_{ij}} = \mathbf{exp}(\frac{\boldsymbol{R_{ij}-D_{ij}}}{\boldsymbol{b}}) \qquad \textbf{Equation 42}$$

R_{ij} is the empirically determined distance for a given cation-anion pair, D_{ij} is a function of atomic coordinates (x, y, z) and unit cell parameters (a, b, c, α, β, γ) and b is an empirical constant 0.37. Values of R_{ij} that give bond valence sums of its oxidation state and its anion have been tabulated.

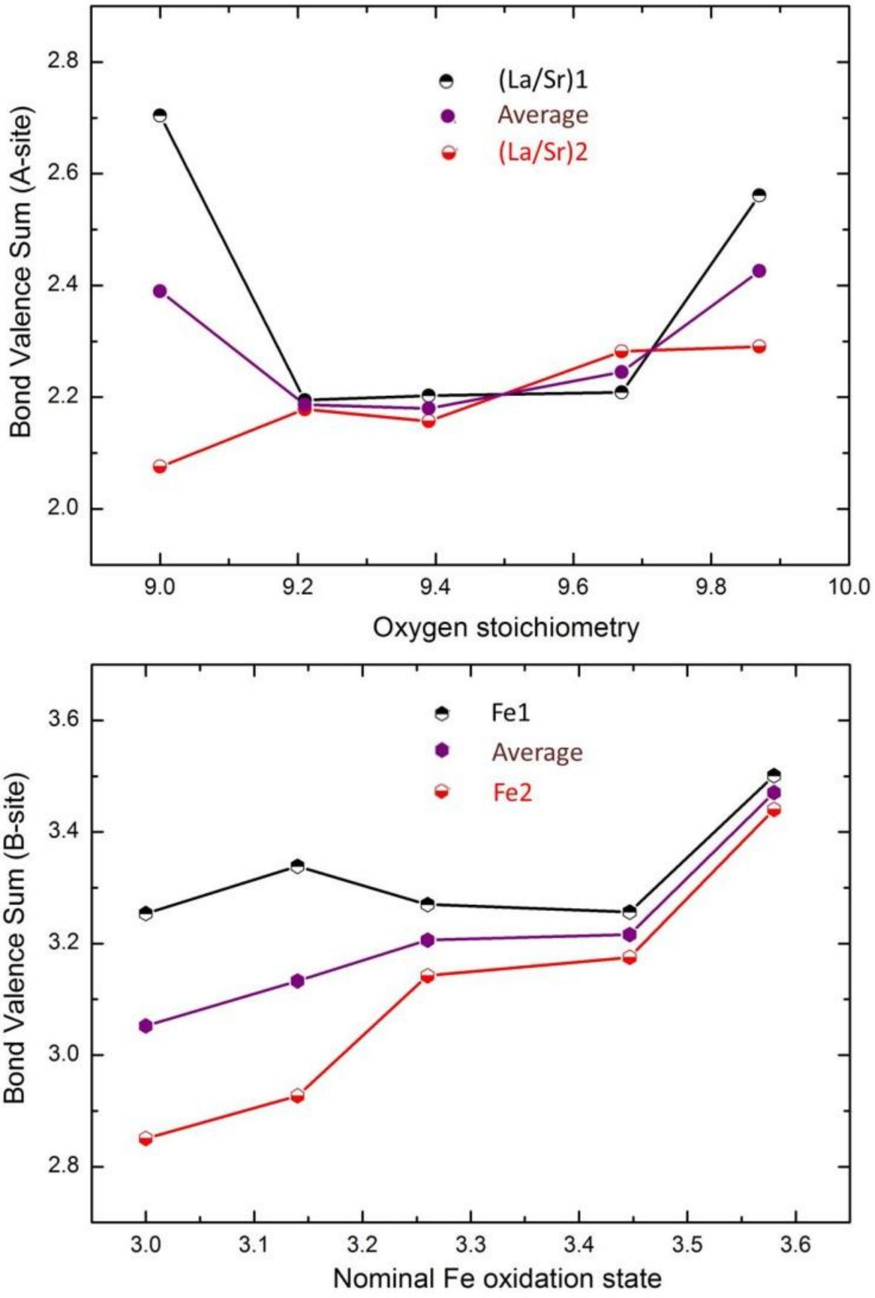

Figure 39. Bond Valence Sum for the A-site (upper graph) and B-site (lower graph). Filled symbols correspond to the average of the A and B sites.

As seen in Figure 39, The value on the A2-site and B2-site is smaller than that of A1 and B1 site due to the oxygen vacancies is coordinated by the A2-/B2-site. Bond-Valence calculations for the $O_{9.87}$ phase using the expression (Equation 42) and $R_{Oj}(Fe^{3+}) = 1.759$, $R_{Oj}(0.25La^{3+} + 0.75Sr^{2+}) = 0.25 \times 2.172 + 0.75 \times 2.118 = 2.132$, yield +3.44 for Fe1 and +3.50 for Fe2. And this value decrease to +2.85 and +3.25 for the phase containing 9 oxygen atoms per formula unit respectively. The bond valence sums for La/Sr site are equal to the value for the site occupant in the phase containing $O_{9.87}$ to $O_{9.21}$, except in the $O_{9.00}$ phase.

4.4 Thermogravimetric investigation

Some selected samples were investigated by monitoring the relative weight change by thermogravimetric (TG) measurements as a function of temperature in the range from 30 ^{o}C to 1200 ^{o}C in air. Previous work shows that the weight change of the moisture-free samples in air attributes to oxygen loss and gain upon heating and cooling. In this work, the oxygen content of the RP3 compound is plotted versus temperature assuming that all mass changes are due to loss and gain of/from to the oxygen lattice of the RP3 compounds (for calculation see Appendix C). In the TGA measurements, the flow speed of air is 50 ml/min while the protective gas N_2 is 25 ml/min, thus the calculated pO_2 is 14% (Air is of 21% oxygen and 78% Nitrogen).

4.4.1 Oxidized samples

The thermal behavior of the oxidized sample with $LaSr_3Fe_3O_{9.96}$ and $NdSr_3Fe_3O_{9.98}$ were investigated in air, as displayed in Figure 40.

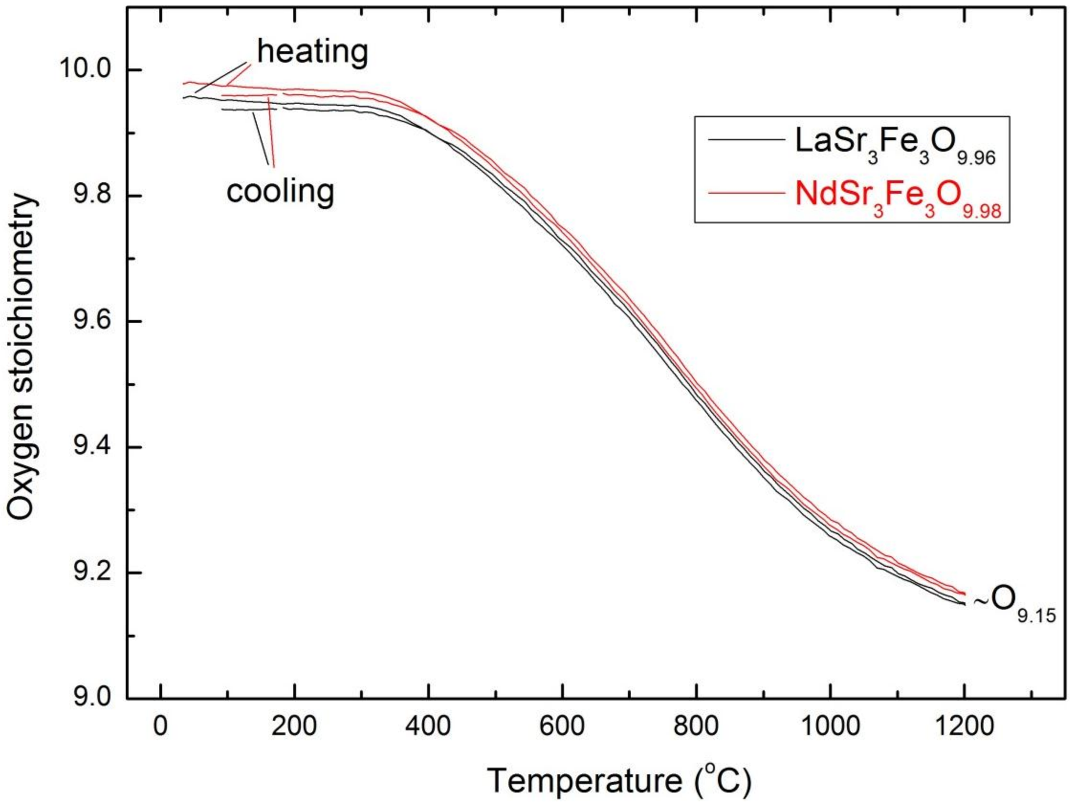

Figure 40. Oxygen content of fully oxidized $LnSr_3Fe_3O_{10-\delta}$ (Ln = La, Nd) series as a function of temperature.

The TGA results clearly show that these two samples display the same behavior under the same heating and cooling condition. Upon heating, no net mass change was observed from room temperature to around 300 ^oC. Above 300 ^oC, both $LaSr_3Fe_3O_{9.96}$ and $NdSr_3Fe_3O_{9.98}$ start to release oxygen gradually, reaching $O_{9.15}$ and $O_{9.18}$ at 200 ^oC. Cooling the same samples in air reversibly intercalates oxygen into the structure with final composition of $O_{9.92}$ and $O_{9.96}$ at room temperature.

4.4.2 Reoxidation of reduced samples

For the $LaSr_3Fe_3O_{10-\delta}$ series, the nominal composition with $LaSr_3Fe_3O_{9.46}$, $LaSr_3Fe_3O_{9.00}$ and $LaSr_3Fe_3O_{8.68}$ were reoxidized in the TGA in air. As TOPAS gives, nominal composition $LaSr_3Fe_3O_{9.46}$ is of 79.19% RP3 $LaSr_3Fe_3O_{10-\delta}$ phase and 20.81% $LaSr_3Fe_3O_9$ type structure. The oxygen content of each measured sample is consistent with titrated data and then this value is change with elevated temperature due to mass loss and gain, for calculations see Appendix D.

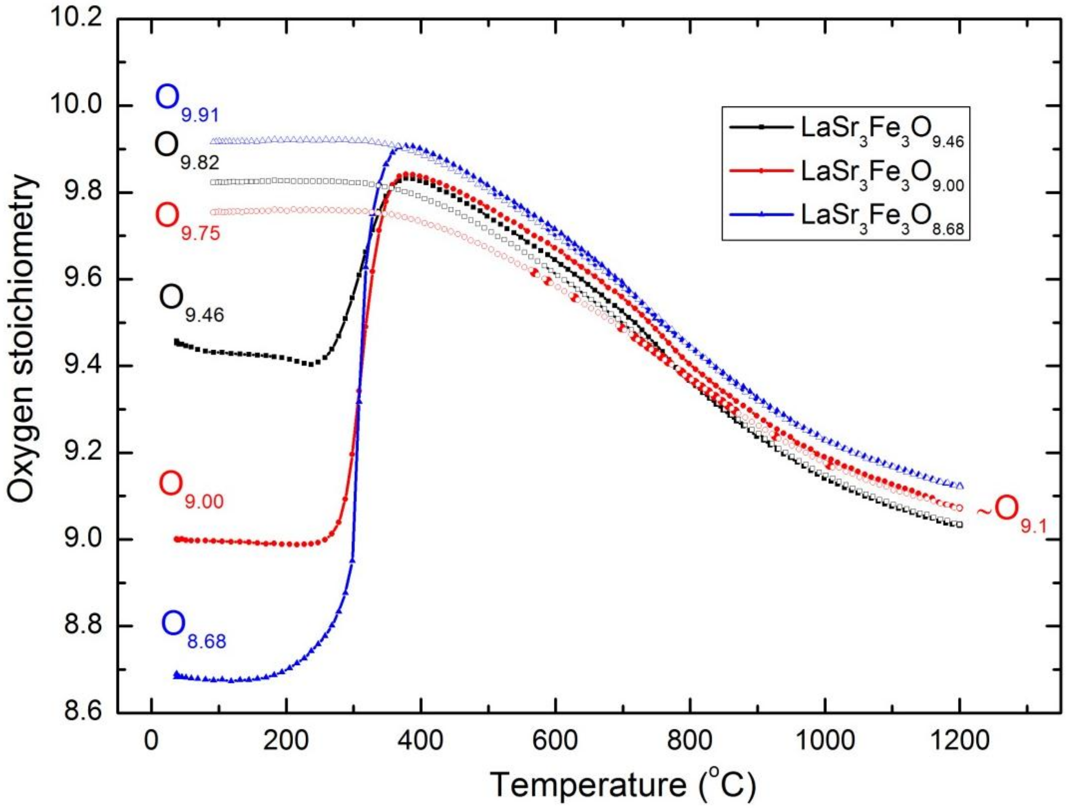

Figure 41. Oxygen content of some oxygen deficient $LaSr_3Fe_3O_{10-\delta}$ series as a function of temperature. Closed symbols are the data being obtained by heating, while open symbols are from cooling.

Figure 42 displays how the oxygen content changes for phase pure $NdSr_3Fe_3O_{9.39}$ and $NdSr_3Fe_3O_{9.00}$ upon heating and cooling.

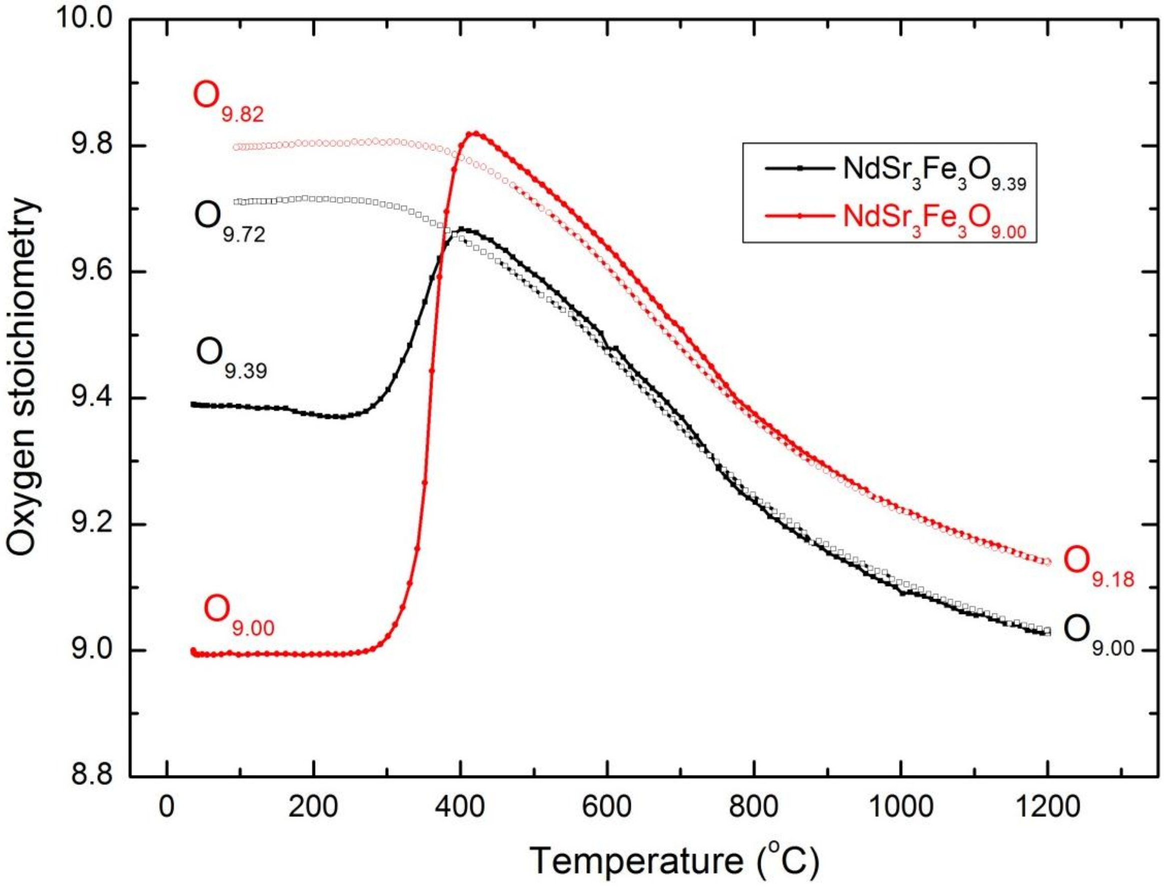

Figure 42. Oxygen content of some oxygen deficient $NdSr_3Fe_3O_{10-\delta}$ series as a function of temperature. Closed symbols are the data being obtained by heating, while open symbols are from cooling.

As can be seen from Figures 41 and 42, the variation in oxygen stoichiometry in air (pO_2 = 14%) with temperature for these two series has the similar trend. The compounds are very stable until the temperature reaches 280 °C. Above that temperature, the first initial oxygen uptakes begins and reaches its maximum at about 400 °C for the different oxygen deficient samples. The so-calculated maximum oxygen stoichiometry at about 400 °C is around $O_{9.80}$ per formula unit. And thereafter the intercalated oxygen in the lattice is lost continuously up to 1200 °C, reaching different oxygen value, around $O_{9.10}$. With their specific oxygen contents at the maximum temperature, the oxygen content losses until certain value obtained when the temperature is decreasing to room temperature in air.

The calculated oxygen content of these samples via TGA together with titration are listed in Table 22, see calculation in Appendix E on Page 139.

Table 22. Calculated oxygen content obtained by cerimetric titration and TGA

	$LaSr_3Fe_3O_{10-\delta}$			$NdSr_3Fe_3O_{10-\delta}$	
Cerimetric titration	9.46	9.00	8.68	9.39	9.00
TGA	9.53	9.13	8.67	9.55	9.09

It can be seen that some difference exist in these two methods, especially for these compounds whose oxygen stoichiometry higher than $O_{9.0}$. The discussion is presented in 5.2.1 on Page 109.

4.5 Magnetic property

The magnetic properties of low temperature ranging from 5 K to 300 K were measured with an MPMS (Magnetic Property Measurement System) and PPMS (Physical Property Measurement System), Quantum Design. Magnetization measurements were carried out with the DC-extraction method for both Field-Cool (FC) and Zero-Field-Cool (ZFC) samples between 5 and 300 K, while M(H) data were measured at 5 K or 300 K.

4.5.1 $LaSr_3Fe_3O_{10-\delta}$ series

4.5.1.1 M(T) behavior

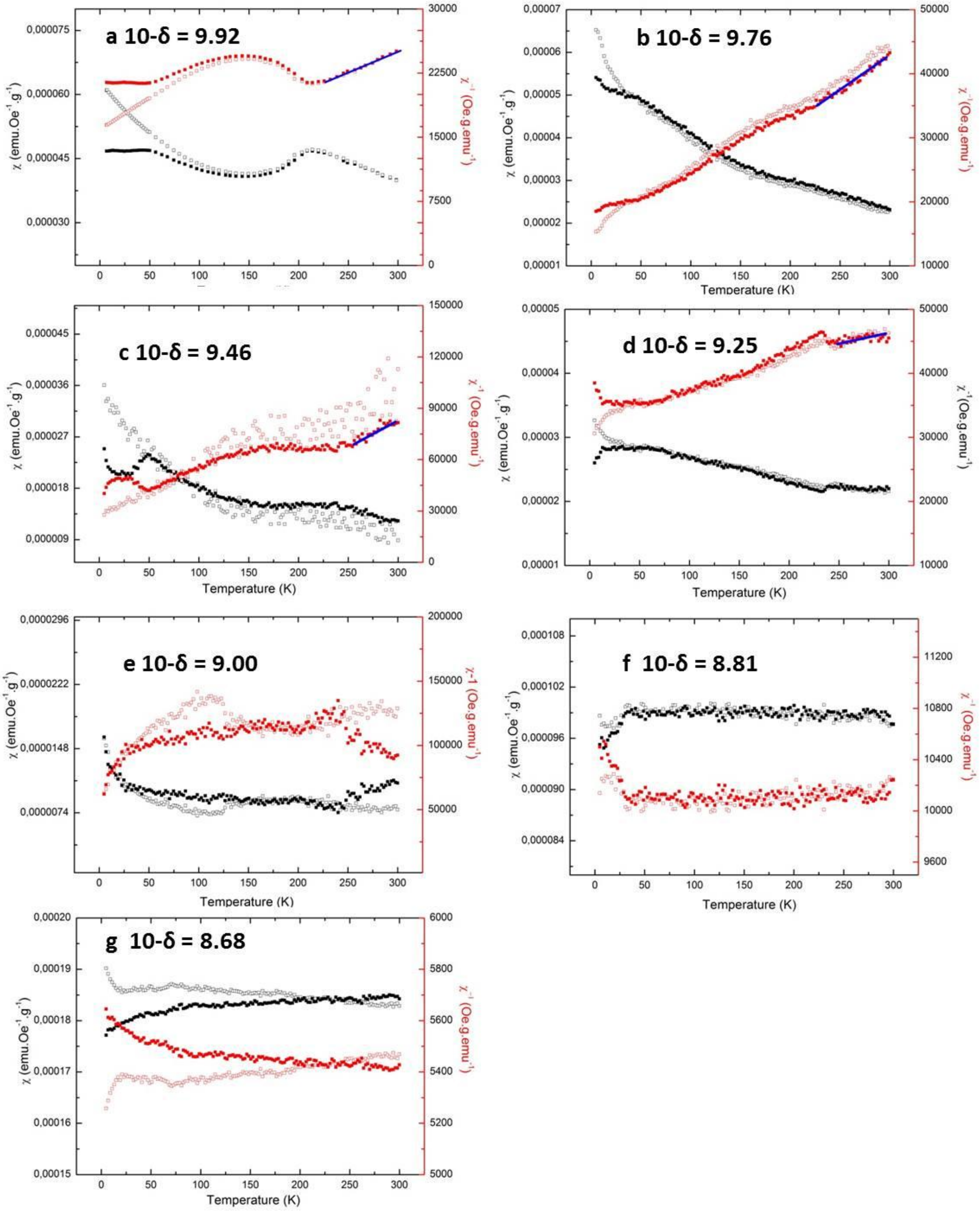

Figure 43. Zero Field Cooled (ZFC, open symbols) and Field Cooled (FC, filled symbols) evolution of the gram susceptibility (black symbols) and inverse gram susceptibility (red symbols) collected by MPMS (a) and PPMS (b→g) in the $LaSr_3Fe_3O_{10-\delta}$ series for the oxygen content $10-\delta$ = a) 9.92, b)9.76, c)9.46, d) 9.25, e)9.00, f)8.81, g)8.68.

The temperature dependences of the magnetic gram susceptibility and also the inverse gram susceptibility measured under ZFC and FC conditions are plotted in Figure 43. The FC and ZFC susceptibilities for the fully oxygen enriched $LaSr_3Fe_3O_{9.92}$ was measured in a field of 0.05 T, as shown in Figure 43.a. The ZFC curve shows an anomaly around 200 K and that indicates onset of antiferromagnetic order below some 200 K. This results is good agreement of previous study [65]. At high temperatures, the inverse susceptibility follows the Curie Weiss law.

Once small amount of oxygen deficiencies ($\delta = 0.24$) are introduced the FC-ZFC curves for $LaSr_3Fe_3O_{9.76}$ samples increase monotonously and exhibit Curie-Weiss behavior at high temperatures.

Concerning $LaSr_3Fe_3O_{9.46}$, the M(T) behavior suggests paramagnetism at temperature higher than 250 K. The FC curve is quite noisy, most likely due to a slight shift in sample position during measurement. The ZFC curve indicates a transition temperature from one AF to another AF structure or a spin glass transition around 50 K. More detailed studies are required, and measurements using AC-option on the PPMS would be helpful for clarifying the possible existence of a spin-glass state.

For the more oxygen deficient $LaSr_3Fe_3O_{9.25}$, a jump at 220 K is indicative of an AF to PM transition. The M(T) curve is consistent with Curie-Weiss paramagnetism above that ordering temperature.

The observed behavior for $LaSr_3Fe_3O_9$ appears to be antiferromagnetic with an ordering transition at 250 K. For the samples with a nominal Fe oxidation state lower than +3, i.e. $LaSr_3Fe_3O_{8.81}$ and $LaSr_3Fe_3O_{8.68}$, the M(T) curve is close to temperature independent. The latter sample shows the higher susceptibility.

Based on a fit of the best straight line of the data at high temperatures for the various $LaSr_3Fe_3O_{10-\delta}$ ($10-\delta = 9.96, 9.75, 9.46, 9.25$, see blue line) as shown in Figure 43, values of Curie-Weiss temperature, u_{eff} and unpaired electrons per iron atom are derived. The derived results are summarized in Table 23.

Table 23. Magnetic parameters for $LaSr_3Fe_3O_{10-\delta}$ ($10-\delta$ = 9.96, 9.75, 9.46, 9.25) series

Oxygen content $10-\delta$	Weiss temperature (K)	u_{eff} (B.M.)	Number of unpaired electrons
$O_{9.96}$	-204.75	6.26	5.34
$O_{9.75}$	-189.03	5.95	5.04
$O_{9.46}$	-31.76	2.47	1.66
$O_{9.25}$	-476.13	5.58	4.67

However, it is still seen that the Weiss temperature and the unpaired electrons per Fe decrease with less oxygen stoichiometry in the composition with $O_{9.46}$. Concerning that there are two phases coexisting in the phase containing $O_{9.25}$ and $O_{9.25}$, it is not feasible to obtain the precise magnetic parameters for each phase. The effective moments of $O_{9.96}$, $O_{9.75}$ and $O_{9.25}$ phase are close to the value for high spin (HS) Fe.

4.5.1.2 M(H) behavior

The field dependency of the magnetization for $LaSr_3Fe_3O_{10-\delta}$ at 5 K is shown for six compositions in Figure 44.

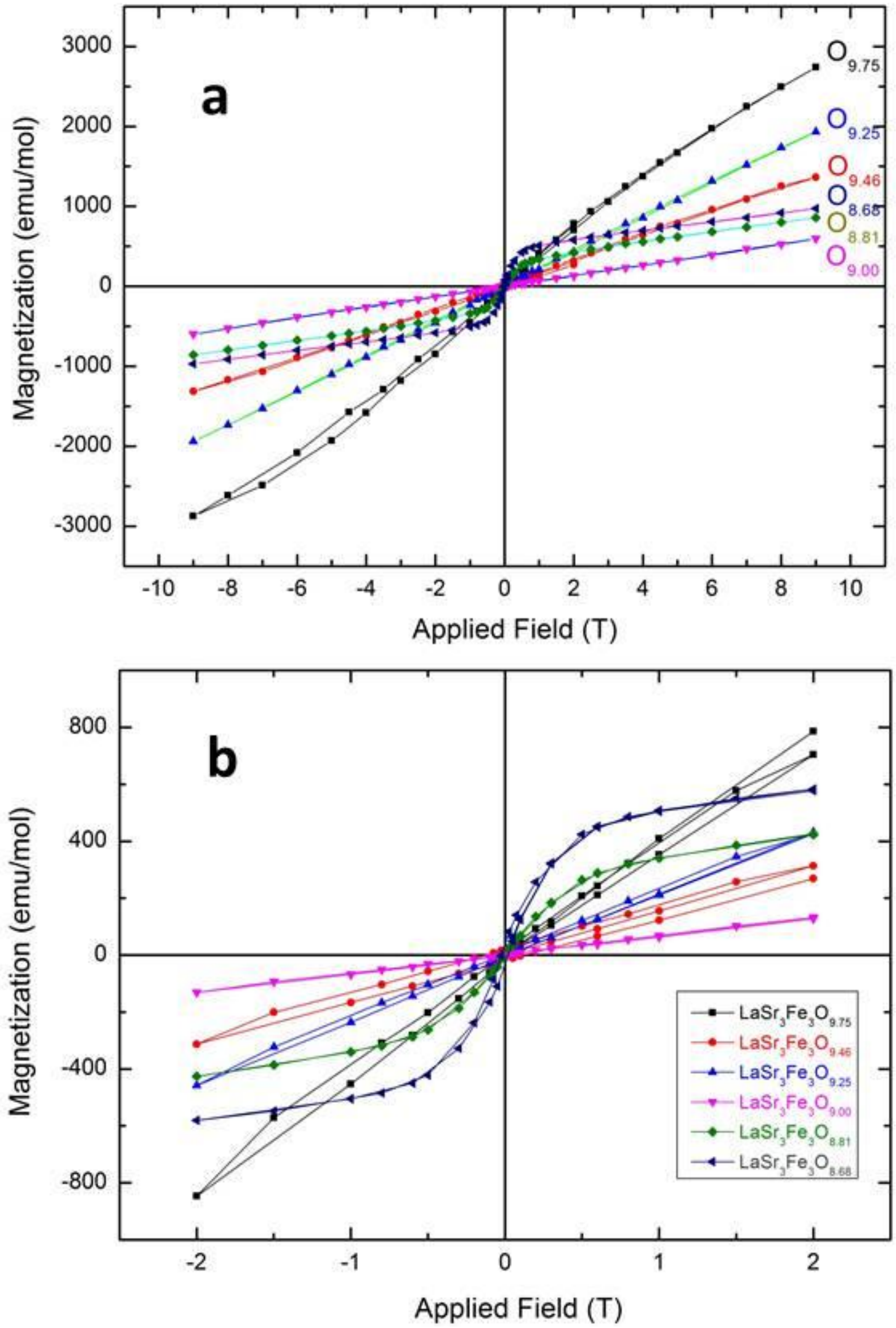

Figure 44. Molar magnetization as a function of applied field (-9 T ~ 9 T) for the $LaSr_3Fe_3O_{10-\delta}$ series (10–δ = 9.75, 9.46, 9.25, 9, 8.81, 8.68) at 5 K. Figure b is the enlargement of Figure a between -2 T and 2 T.

As can be seen from Figure 44, $LaSr_3Fe_3O_{8.81}$ and $LaSr_3Fe_3O_{8.68}$ both have an S-form at low-to-moderate fields (T < 1 T, see Figure 44.b) where a ferromagnetic component appears to saturate. Thereafter their magnetization increase linearly with applied field (1 < T < 9 T), indicating antiferromagnetism. These two samples may possibly approach a saturation value at higher fields. The calculated magnetization saturation is calculated by extrapolating the linear M(H) part to where it crosses the y-axis. The derived values are 0.19 and 0.29 u_B for $LaSr_3Fe_3O_{8.81}$ and $LaSr_3Fe_3O_{8.68}$ respectively. These ordered components are small and the samples are probably best described as ferrimagnetic at 5 K.

Most of these samples, $LaSr_3Fe_3O_{10-\delta}$ (10–δ = 9.76, 9.46, 9.25) have a hysteresis, indicating that these have a ferromagnetic component at 5 K. For $LaSr_3Fe_3O_9$, the M(H) curve is quite linear which would be consistent with antiferromagnetism.

Among these samples, $LaSr_3Fe_3O_{8.68}$ was selected to measure its M(H) behavior at room temperature. The field dependence of the magnetization is shown for temperature 5 K and 300 K respectively.

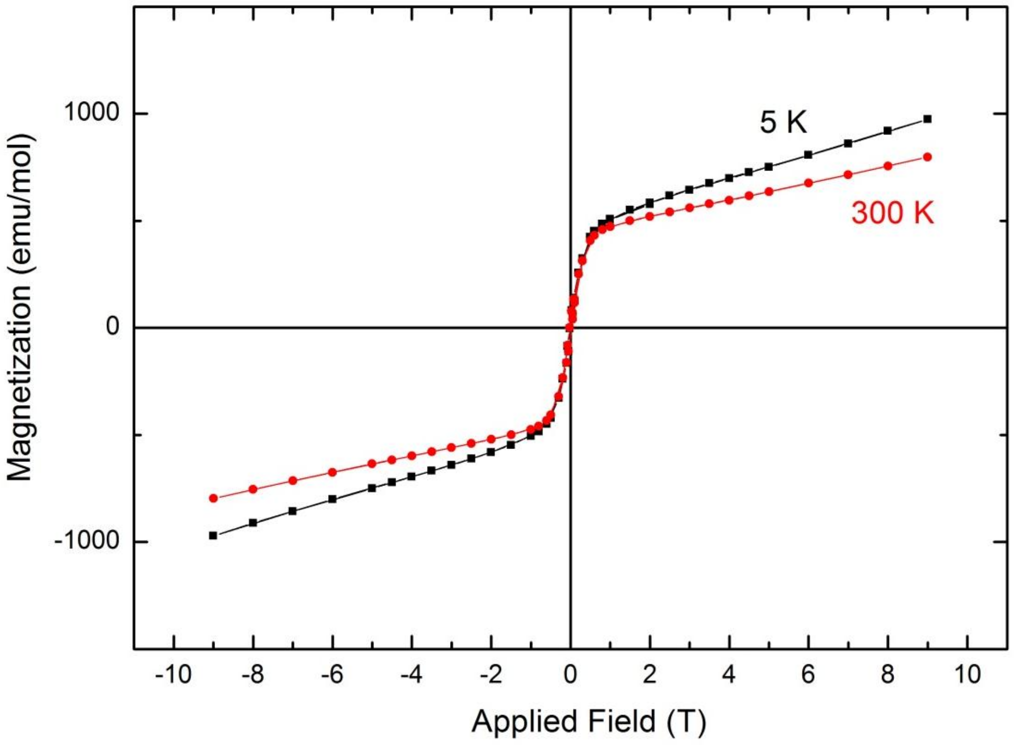

Figure 45. Field dependency of the magnetization for $LaSr_3Fe_3O_{8.68}$ at 5 K and 300 K

As shown in Figure 45, no complete saturation of the sample was observed for the fields of 9 T either at 5 K or 300 K. At 5 K, the saturation magnetization of $LaSr_3Fe_3O_{8.68}$ is higher than that of 300 K, corresponding values are 0.29 u_B and 0.26 u_B per unit of transition metal, respectively. These data are important due to either ***1)*** ordering is well above room temperature and the magnetic properties of the material remain rather constant or ***2)*** there are small amounts of magnetic impurities i.e. magnetite introduced during the reduction.

4.5.2 $NdSr_3Fe_3O_{10-\delta}$ series

4.5.2.1 M(T) behavior

FC and ZFC susceptibility vs temperature measurements were performed on the series of $NdSr_3Fe_3O_{10-\delta}$ ($8.78 \le 10-\delta \le 9.98$) from 5 K to 300 K, as displayed in Figure 46.

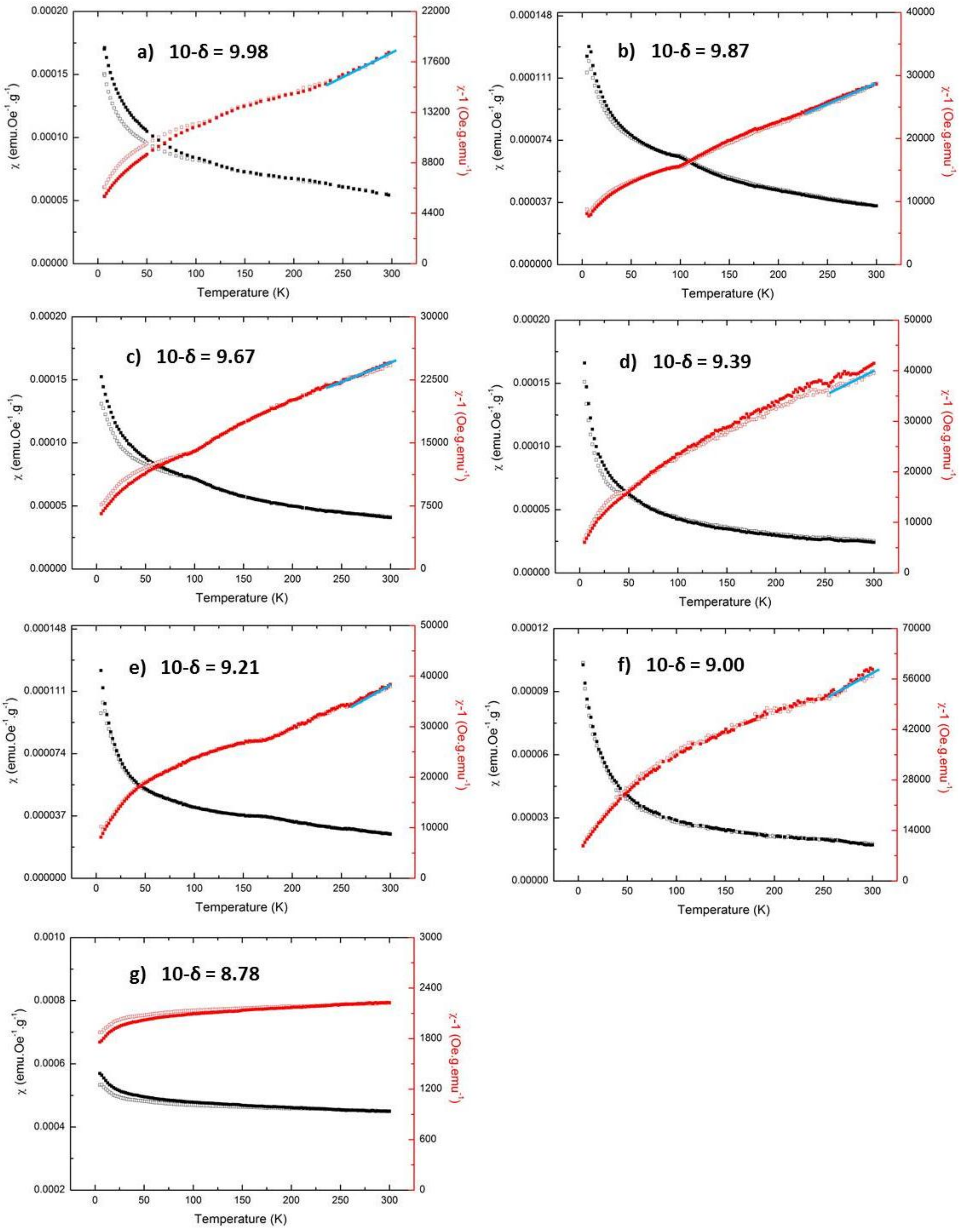

Figure 46. Zero Field Cooled (ZFC, open symbols) and Field Cooled (FC, filled symbols) evolution of the gram susceptibility (black symbols) and inverse gram susceptibility (red symbols) collected by MPMS (a) and PPMS (b→g) in the $NdSr_3Fe_3O_{10-\delta}$ series for the oxygen content 10–δ = a) 9.98, b)9.87, c)9.67, d) 9.39, e)9.21, f)9.00, g)8.78.

Most of the samples with oxygen content 10–δ ≥ 9.39 are found to be antiferromagnetic at low temperatures and a Curie-Weiss paramagnetic region is observed at high temperatures (Figure 46.a–d). The ZFC and FC curves of $NdSr_3Fe_3O_{9.21}$ and $NdSr_3Fe_3O_{9.00}$ are identical; both are paramagnetic above some 250 K and exhibit Curie-Weiss behavior (Figure 46.e and f). For the more oxygen deficient compound $NdSr_3Fe_3O_{8.78}$, a temperature independent M(T) curve is observed.

For the Nd– series, the FC gram susceptibility has no obvious difference for the compositions (9 ≤ 10–δ < 10) except that $NdSr_3Fe_3O_{8.78}$ has a much larger value.

Certain errors exist in the measurement of $NdSr_3Fe_3O_{9.39}$ and $NdSr_3Fe_3O_{9.00}$ due to a slight movement of the sample during measuring (refer to respective Figure 46.d and f). A linear fit of inverse gram susceptibility for the composition $NdSr_3Fe_3O_{10-\delta}$ (9.00 ≤ 10–δ ≤ 9.98, see blue line in Figure 46) was performed in the paramagnetic region. The obtained negative value for the Weiss temperature and the Curie constant per iron atom along with the corresponding effective paramagnetic moment are listed in Table 24.

Table 24. Magnetic parameters for $NdSr_3Fe_3O_{10-\delta}$ (10–δ = 9.98, 9.87, 9.67, 9.39, 9.21, 9.00)

Oxygen content 10–δ	Weiss temperature (K)	u_{eff} (B.M.)	Number of unpaired electrons
$O_{9.98}$	-167.93	7.05	6.12
$O_{9.87}$	-158.58	5.58	4.67
$O_{9.67}$	-243.06	6.55	5.63
$O_{9.39}$	-300.11	5.42	4.51
$O_{9.21}$	-168.33	4.88	3.98
$O_{9.00}$	-56.02	3.41	2.55

It is seen that u_{eff} (B.M.) decreases with increasing amounts of oxygen vacancies of the samples from c.a 7 to 3.5 u_B except for $NdSr_3Fe_3O_{9.67}$ with a value of 6.5 u_B. The calculated Weiss temperatures decrease for the phase $O_{9.98}$ to $O_{9.39}$ but an increase is seen for further more oxygen nonstoichiometry. It should be pointed out that the phase $O_{9.00}$ is ordered-different crystal structure and magnetism is expected to be somewhat different, e.g. as seen in Weiss temperature.

4.5.2.2 M(H) behavior

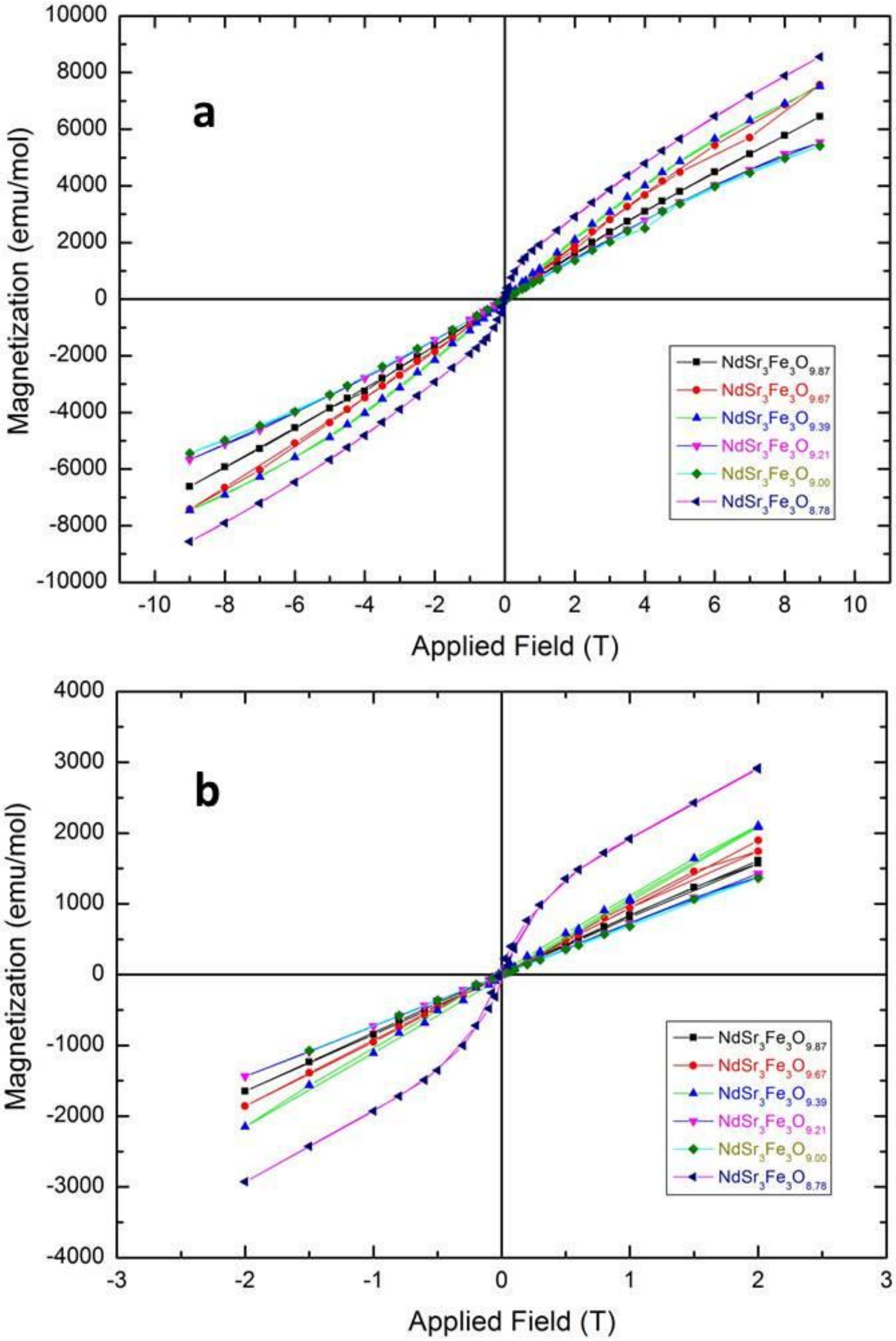

Figure 47. Molar magnetization as a function of applied field (-9 T ~ 9 T) for the $NdSr_3Fe_3O_{10-\delta}$ series ($10-\delta$ = 9.87, 9.67, 9.39, 9.21, 9.00, 8.78) at 5 K. Figure b is the enlargement of Figure a between -2 T and 2 T.

This series M(H) behaviour were measured at 5 K, displayed in Figure 47. Only $NdSr_3Fe_3O_{8.78}$ has an S-form (T < 1 T, see Figure 47.b) with a ferromagnetic component that saturates. Its magnetization increase linearly with applied field (1 < T < 9 T), indicating antiferromagnetism. A saturation value may possibly be obtained if significantly higher fields were available. A hypothetical line of the linear M(H) region crossing y axis gives a small ordered ferromagnetic components of 0.93 u_B per iron.

The samples, $NdSr_3Fe_3O_{10-\delta}$ ($10-\delta = 9.67, 9.39$) have a very small, yet observable hysteresis, indicating that these have a ferromagnetic component at 5 K. A quite linear M(H) curve of the rest three compounds was observed. This suggests antiferromagnetic order under these conditions.

Chapter 5

Discussion

In this section, the experimental results presented in chapter 4 are discussed in view of the published literature. The main discussion covers the results obtained from synthesis, cerimetric titration, TGA, crystal structure refinement as well as magnetic properties.

5.1 Synthesis

Successful synthesis recipes for obtaining phase pure RP3 (Ln-Sr-Fe-O, Ln = La, Nd) were obtained after careful consideration of the annealing conditions and subsequent handling of the samples at ambient conditions after completed synthesis. The former factor is of great importance to obtain the single phases while the latter parameter is essential to avoid degradation of the formed samples due to wrong storing conditions or post treatment during e.g. sample preparation for powder X-ray diffraction.

5.1.1 Preparation of $Ln_xSr_{4-x}Fe_3O_{10-\delta}$ (Ln = La, Nd)

The gels obtained after the complexation step were dried at 180 ^oC overnight, followed by a calcination done at 450 ^oC in a muffle furnace for approximately 18-24 hours. As Figure 25 (Page 59) displays, the XRD pattern of the $LaSr_3Fe_3O_{10}$-precursor after calcining at 450 ^oC overnight, the compounds show presence of a large amount of carbonate i.e. $SrCO_3$, $Ln_2O_2CO_3$ (Ln = La, Nd) together with La-Sr-Fe-O mixture.

Velinov et al. [58] investigated the TG and DTA of a $LaSr_3Fe_3O_{10}$ precursor after drying at 200 ^oC for 2 hours (see Figure 8 on Page 19, section 1.5.2). It is observed several exothermal effects together with significant mass loss due to a stepwise burning off the organic matter between 400 ^oC and 600 ^oC. Considering that we calcined the $LaSr_3Fe_3O_{10}$ precursor at 450 ^oC and it stabilizes $SrCO_3$, may make complicate the formation of the desired RP3 phase. At the end of experimental work of this Master thesis we discovered in a different project that applying a much shorter calcination time (2-3 hours) at 450 ^oC is preferred, followed by a fast heating to 800 - 850 °C for 1 hour to fully remove C/CO_3^{2-} without crystallizing to binary oxides.

The role of annealing condition plays the most important role in obtaining the phase pure product in every synthesis. Atmosphere (e.g. O_2, N_2, Ar etc) annealing is often used. There is a clear trend of lower annealing temperature if atmosphere is involved.

In this work, $LaSr_3Fe_3O_{10}$ was successfully synthesized in air and a Ar atmosphere, with annealing temperatures of 1250 °C and 1100 °C, respectively. Specifically, for the pellets of the fine powder (after calcining at 450 °C), good conditions for annealing in air was found to be 12 hour annealing at 1000 °C and then twice 12 hours annealing at 1250 °C with intermediate grounding and pelletizing. On the other hand, the same compound could be synthesized in an Ar atmosphere at 1100 °C (2 repeating 12 hours annealing steps). Annealing in an Ar atmosphere could be of help to remove C/CO_3^{2-} of the pellets with temperature increasing from room temperature to 1100 °C of the first annealing. As the TGA data of $LnSr_3Fe_3O_{10}$ (Ln = La, Nd) show large oxygen deficient with $O_{9.1}$ at 1200 °C. The use of atmosphere is also a helpful tool to “pick out” oxygen at lower temperatures thereby forming RP3 phases.

5.1.2 Solid solution range for $Ln_xSr_{4-x}Fe_3O_{10-\delta}$ (Ln = La, Nd; x >1.0)

In this work, higher Ln–content than $LnSr_3Fe_3O_{10}$ (Ln = La, Nd) phase pure compounds were not observed due to a large amount of RP1, RP3 and perovskite phase as main contaminants.

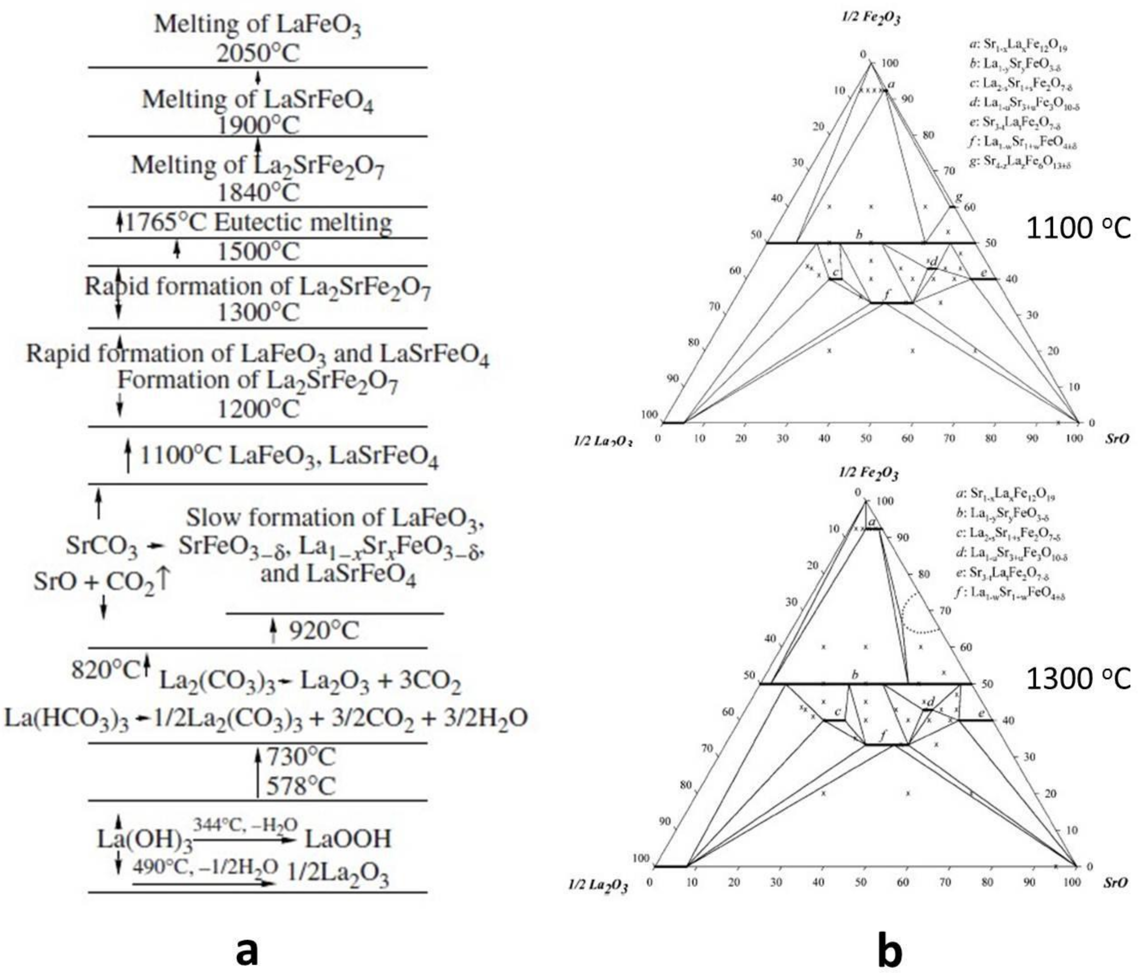

Figure 48. Phase transition schemes. (a) Phase transition schemes of La_2O_3, SrO and Fe_2O_3 mixtures [94]. (b) Isothermal section of the La_2O_3–SrO–Fe_2O_3 system at 1100 °C and 1300 °C. Triangles are given as solid lines and bold lines correspond to solid solutions [95].

Figure 48 displays the phase transition schemes of a La_2O_3–SrO–Fe_2O_3 mixture. Tugova et al. [94] aimed to synthesize RP2 $La_2SrFe_2O_7$ phase as shows in Figure 48.a. A traditional solid state method was applied for both synthesises with La_2O_3 or $La(OH)_3$, Fe_2O_3 and $SrCO_3$ as initial reactants.

Figure 48 clearly shows that it is rather difficult to obtain phase pure RP3 compounds, due to formation of RP2, RP1 and perovskite phase. Further, according to the presented phase diagram, making RP3 phases with x > 1.0 $Ln_xSr_{4-x}Fe_3O_{10}$ (Ln = La, Nd) is possible. This may then very well explain why we in this study not were able to prepare any phase pure $Ln_xSr_{4-x}Fe_3O_{10}$ (Ln = La, Nd) for x > 1.0. The stability scheme of RP phases in binary SrO-Fe_2O_3 is retained at low La levels. Intermediate or higher La level RP1 phase are more stable than RP2 phase.

It is reported that RP1 and RP3 phase for $Sr_{n+1}Fe_nO_{3n+1}$ only are stable at lower temperatures than n = 2 members [61, 96]. Considering the presence of RP1, PR2 and perovskite phase, the annealing temperature was not the right to form RP3 phases for x > 1.0 in $Ln_xSr_{4-x}Fe_3O_{10}$ (Ln = La, Nd). On the other hand, the solid solution range in $Ln_xSr_{4-x}Fe_3O_{10}$ is narrow, especially for x > 1.0. These may be reasons why we successfully obtained some phase pure compounds in $0 < x \leq 1.0$ $Ln_xSr_{4-x}Fe_3O_{10}$ (Ln = La, Nd) but failed in x > 1.0.

For further synthesis of $Ln_xSr_{4-x}Fe_3O_{10}$ (Ln = La, Nd; x > 1.0), more careful and critical annealing conditions e.g. 1050-1200 °C, N_2 or O_2 atmosphere sintering than that of involved sintering programs will preferably be tried to get RP3 form.

5.1.3 Comparison of synthesis condition $Ln_xSr_{4-x}Fe_3O_{10}$ (Ln = La; x = 1.0)

Solid-state method of synthesizing the series $LaSr_3Fe_3O_{10}$ series are reported in some scientific reports [44, 56,]. Of course, citric acid method has been successfully used to synthesize $LnSr_3Fe_3O_{10}$ (Ln = La; x = 1.0) series compounds. The following Table 25 summarizes this method with their specific experimental details.

Table 25. Experimental detail in synthesis $LaSr_3Fe_3O_{10}$ using citric acid method

Experimental details	Velinov et al. [58]	Zhang et al. [62]	In this study
Starting materials	La_2O_3 $Sr(NO_3)_2$ $Fe(NO_3)_3 \cdot 9H2O$	$La(NO_3)_3 \cdot 6H_2O$ $Sr(NO_3) \cdot H_2O$ $Fe(NO_3)_3 \cdot 9H_2O$	La_2O_3 $SrCO_3$ $Fe(COOH)_2 \cdot 2H_2O$
Gelation	200 °C	120 °C	180 °C over night
Calcination	Self-combustion	Sand bath	450 °C over night
Annealing	1100 °C × 2 h	1000 °C × 12 h 1200 °C × 8 h	1000 °C × 12 h 1250 °C × 12 h × 2

Velinov et al. [58] used the experimental detail as described in Table 25 to synthesize $LaSrFeO_4$, $La_2SrFe_2O_7$ and $LaSr_3Fe_3O_{10}$. He claimed that the formation of $LaSrFeO_4$ phase begins at 900 °C and after treatment at 1000 °C for 2 hours there are no additional phases in the sample. $La_2SrFe_2O_7$ was calcined at 700 °C, 800 °C, 900 °C, 1000 °C and 1100 °C for 2 h, at 1250 °C for 5 hours and at 1400 °C for 1 hour respectively. The powder X-ray diffraction patterns show that a formation of the single layer $LaSrFeO_4$ perovskite occurs at 1100 °C and at 1250 °C begins to form double layer $La_2SrFe_2O_7$ phase. The sample calcined at 1400 °C for 1 hour is a mixture of 80% $La_2SrFe_2O_7$ phase and 20% RP1 $LaSrFeO_4$ phase. For $LaSr_3Fe_3O_{10}$, the precursor powders were calcined at 700 °C, 800 °C, 900 °C, 1000 °C and 1100 °C for 2 hours. The author believed that a thermal treatment at temperature not lower than 1100 °C is necessary for synthesis $LaSr_3Fe_3O_{10}$ phase [58].

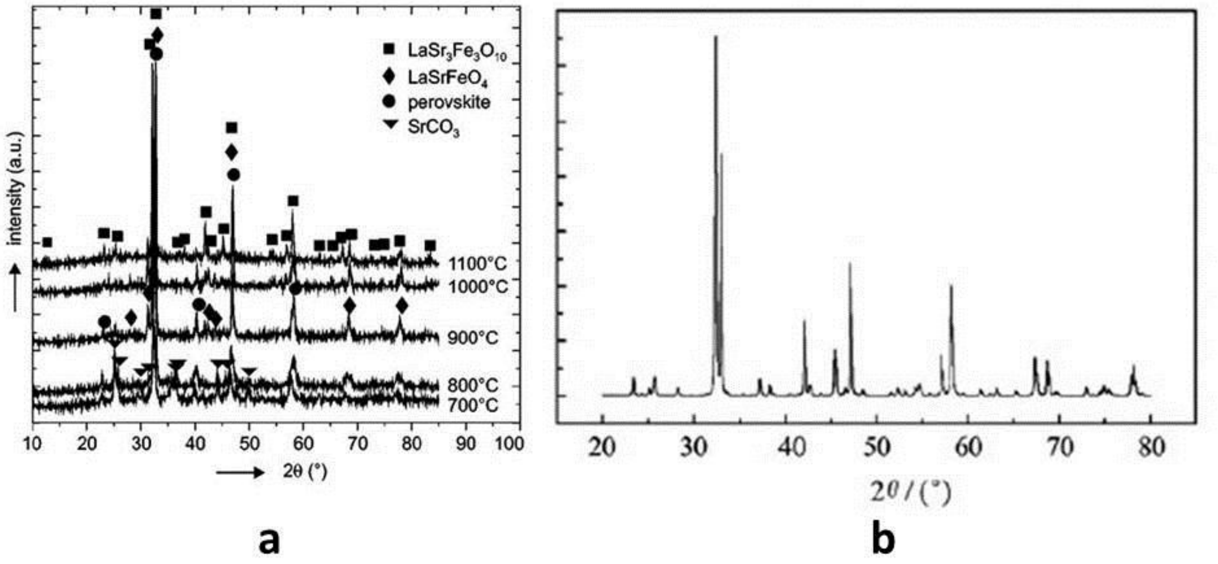

Figure 49. Powder X-ray diffraction patterns of $LaSr_3Fe_3O_{10}$ phase. (a) $LaSr_3Fe_3O_{10}$ precursor powder calcined at different temperatures [58]. (b) $LaSr_3Fe_3O_{10}$ calcined at 1200 °C [62].

As indicated in Table 25, Zhang et al. [62] also synthesized $LaSr_3Fe_3O_{10}$, the precursor powder was calcined at 1000 °C in oven for 12 hours and then pressed into slabs and sintered again at 1200 °C for 8 hours [62].

By comparing Figure 49.a and b as well as Figure 26 on Page 63 (refer to XRD pattern for $LaSr_3Fe_3O_{10}$ in this work), it is highly suspected that the obtained compound calcined at 1100 °C (Figure 49.a) for 2 hours has a large amount of RP1 $LaSrFeO_4$ and perovskite phase.

In this study, the obtained $LaSr_3Fe_3O_{10}$ compound annealed at 1100 °C for 48 hours and followed by 24-hour firing at 1100 °C (refer to Appendix C.2 on Page 128), is a mixture of about 70% RP3 phase and 30% perovskite. When the temperature is elevated at 1350 °C, RP2 occurs as a new secondary phase.

5.2 Oxygen content

5.2.1 Comparing oxygen content from cerimetric titration and TGA

The oxygen content differs in the value obtained from direct cerimetric titration and TGA data. It is noticeable that there were errors and uncertainties in the cerimetric titration, especially for the oxygen deficient samples. As discussed in subchapter 3.3 (Page 55), some factors may contribute to the errors in cerimetric titration; on the other hand, $O_{9.90}$ is only an assumption for all samples being cooled down to room temperature with thermal program (50 ml/min Air, 10 °C/min), see Appendix E on Page 139. In addition, the possible impurities may also contribute this problem.

The real oxygen content is the value slightly higher than the titrated value and lower than TGA results for the compound with expressed oxygen higher than $O_{9.0}$. The result of the oxygen content lower than $O_{9.0}$ is in good agreement in these two methods.

In this work, we use the oxygen content calculated from cerimetric titration as its “real” value of its oxygen stoichiometry.

5.2.2 Approaches of higher oxygen content

There are some ways that have been tried in this project to obtain large range oxygen content in the sample, including ***1)*** fully oxidized ***2)*** quenching ***3)*** oxygen-getter Zr method. The obtained oxygen content of the reduced sample is as low as $O_{8.68}$ for La- series and $O_{8.78}$ for Nd- series.

Thus, there are some methods to obtain larger oxygen deficiencies e.g. $\delta > 1.5$:

- Excessive amount of Zr (due to the fact that Zr reacted partially than calculating).
- By elevating the temperature of Zr site is another route.

In the results section, we used excessive Zr approach instead of modifying temperature on Zr site to control the oxygen content despite the latter approach would give better control.

Jantsky et al. [67] reduced $PrSr_3Co_{1.5}Fe_{1.5}O_{10-\delta}$ with composition as low as $10-\delta = 8.20$ under a 12 hours flow of H_2 atmosphere at 500 °C. Motivated by this method, carefully selected atmosphere and thermal treatment would give larger oxygen deficiencies than that of RP3 phase obtained in this project. It should be pointed out that this method does not allow to make a series of samples with variable oxygen content.

5.3 Rietveld refinement

When dealing with Rietveld analysis, it is of great importance to realize that the information about the crystal structure is limited by the quality of SRXRD pattern. By comparing the refined data from XRD and SRXRD, they both show the same unit cell parameters, as expected. The higher R-factors for the refined SRXRD data is due to the low background, and the excellent signal to noise ratio as well as larger challenges in fitting the profiles of the peaks.

5.3.1 Crystal structure

The (SR)XRD diagrams show that $LaSr_3Fe_3O_{10-\delta}$ ($\delta < 0.5$) and $NdSr_3Fe_3O_{10-\delta}$ ($\delta < 0.8$) crystallize in the RP3 structure, adopting the I4/mmm space group. SRXRD Rietveld results confirm that oxygen vacancies are located to the O4 site in the RP3 structure, see Figure 50.a. This result is consistent with reported scientific report [56, 91].

With increasing amounts of oxygen vacancies at the O4 site, the structure is distorted gradually. At half oxygen occupancy for the O4 site, an ordering process takes place. This structure is described in space. The $LnSr_3Fe_3O_9$ (Ln = La, Nd) is an oxygen deficient RP3 phase than can be considered as the intergrowth of brownmillerite-type ($Sr_2Fe_2O_5$) and K_2NiF_4-type layers ($LnSrFeO_4$; Ln = La, Nd).

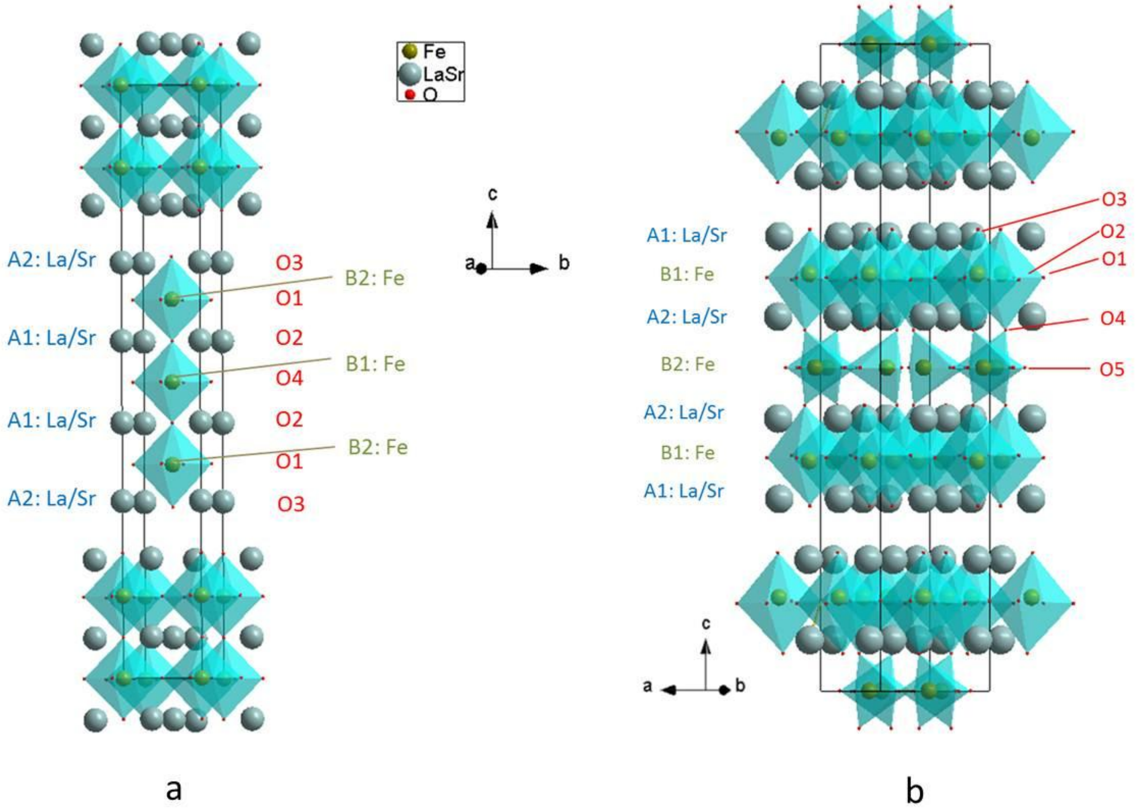

Figure 50. Crystal structure of $LnSr_3Fe_3O_{10-\delta}$ ($0 < \delta < 1.5$). (a) RP3 phase, space group I4/mmm ($0 < \delta < 0.5$ for $LaSr_3Fe_3O_{10-\delta}$ and $0 < \delta < 0.8$ for $NdSr_3Fe_3O_{10-\delta}$) (b) Oxygen deficient RP3 phase $LnSr_3Fe_3O_9$, space group Bbmm.

The oxygen migration in the RP3 phase leads to the concentration of the vacancies in the central perovskite layer (O4 site as shown in Figure 50.a). The process has earlier been described to involve the following successive steps [91]:

1) Vacancies are initially located in the O3 site, the most labile oxygen atoms of the rock salt layer.
2) Then these vacancies will be filled by the nearest oxygen on the O1 site.
3) The oxygen atom on the O2 site will move to the vacant O1 site.
4) Finally, these vacancies will be occupied by the oxygen atoms on the O4 site, thus the vacancy will concentrate in the equatorial plane of the central perovskite block.

The samples of $NdSr_3Fe_3O_{10-\delta}$ ($0.5 < \delta < 0.8$) are single phase. On the other side two phases coexist in $LaSr_3Fe_3O_{10-\delta}$ in the range $0.5 < \delta < 0.8$. By considering the above process of creating oxygen vacancies on the O4 site, this phenomenon may possibly be explained as: the oxygen atoms on the O1, O2 and O4 site are more labile in $LaSr_3Fe_3O_{10-\delta}$ ($0.5 < \delta < 0.8$) than that of $NdSr_3Fe_3O_{10-\delta}$ ($0.5 < \delta < 0.8$).

Further, increased amounts of oxygen vacancies beyond $\delta \approx 1$ are found to mainly locate at the O2 site, see Figure 50.b.

5.3.2 Unit cell parameters of Less Ln–content than $LnSr_3Fe_3O_{10-\delta}$ (Ln = La, Nd)

According to Figure 31 (Page 74), the refined unit cell parameters of phase pure $Ln_xSr_{4-x}Fe_3O_{10}$ is slightly decreasing when the lanthanide content at the A-site in the RP3 phase decreases, especially for the c axis parameter. This could be explained that the size of lanthanide element (La^{3+} = 1.032 Å and Nd^{3+} = 0.983 Å [97]) is smaller than the alkaline earth element at the A-site cation (Sr^{2+} = 1.18 Å [97], in this case). The number of perovskite slabs is largest along the c direction. This leads to a more significant decrease in the c axis than that for the a and b axis.

Comparing the two series, the Nd– series has smaller unit cell dimensions than the La– series for any given value of x for $Ln_xSr_{4-x}Fe_3O_{10}$. This is consistent with the smaller size of Nd^{3+} compared to La^{3+}.

5.3.3 Unit cell parameters of $LnSr_3Fe_3O_{10-\delta}$ (Ln = La, Nd)

As the refined unit cell parameters and the figures above (Figure 34, Page 79; Figure 35, Page 81) shown, the a and b axes of the structure in the of Bbmm space group are $\sqrt{2}$ times longer than for the tetragonal I4/mmm structure.

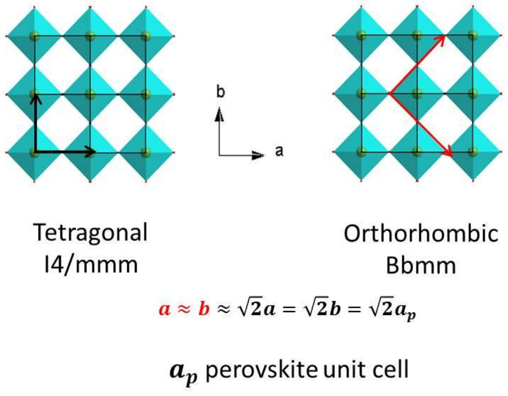

Figure 51. Lattice parameter in a and b direction for two type of structures in space group I4/mmm and Bbmm.

The unit cell parameters increase with decreasing oxygen stoichiometry at room temperature. This phenomenon can be explained as follows:

- Larger size of B-site cations upon reduction. It is reported that B-site cations consist of mixed Fe^{3+} and Fe^{4+} ions . Upon an oxygen content decrease from 10 to 9 per formula unit, the average valence of Fe decreases from +3.67 to +3 according to the titrated Fe valence state. The radius radii Fe^{3+} is larger than that of Fe^{4+} whether being High Spin (HS) or Low Spin (LS) [97].
- Less efficient packing. The packing of all atoms become less efficient if vacancies present in the structure, and also structural distortion makes a contribution.

The current data for the c-axis as a function of oxygen content $LaSr_3Fe_3O_{10-\delta}$ ($\delta < 0.8$) is somewhat inconsistent with the literature (see Figure 52).

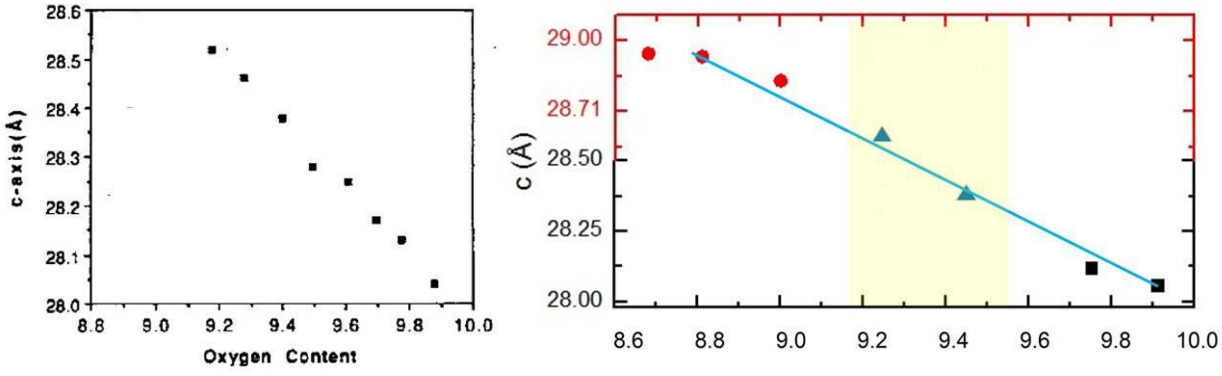

Figure 52. c axis parameters as a function of oxygen stoichiometry in $LaSr_3Fe_3O_{10-\delta}$ at room temperature. (a) Published data are from Lee [56]. (b) c-axis parameters refined from powder X-ray patterns of $LaSr_3Fe_3O_{10-\delta}$. $LaSr_3Fe_3O_{9.46}$ and $LaSr_3Fe_3O_{9.25}$ in the yellow zone were only refined using RP3 structure despite that some peaks were not indexed.

Lee et al. found that $LaSr_3Fe_3O_{10-\delta}$ is able to adopt a larger amount of oxygen vacancies ($\delta < 0.8$) without structural degradation [56]. However, the current XRD data show that there two phases ($LaSr_3Fe_3O_{10-\delta}$ RP3 structure and $LaSr_3Fe_3O_9$ deficient RP3 structure) coexists in $LaSr_3Fe_3O_{10-\delta}$ ($\sim 0.5 < \delta < 0.8$, see yellow zone in Figure 52.b). If $LaSr_3Fe_3O_{10-\delta}$ ($\sim 0.5 < \delta < 0.8$) was refined assuming a single RP3 phase, these erroneous data (see green line in Figure 52.b) would be in good agreement with Lee's result (Figure 52.a [56]).

5.4 Magnetic properties

The paramagnetic parameters as listed in Tables 23 and 24 (Pages 96 and 101 respectively) are unfortunately strongly dependent on how the data is fitted assuming a straight line at higher temperatures (~200 K → 300 K) for a Curie-Weiss regime. There are errors caused by noisy data in some measurements. On the other hand, the Curie-Weiss law fit would be more reliable if the data were measured at temperatures considerably exceeding than 300 K. The derived values of Curie-Weiss temperature, u_{eff} and unpaired electrons should therefore be considered as rough values rather than precise ones.

For the gram susceptibility of these two series, the Nd– series have lager gram susceptibility, especially in the paramagnetic region. This can be explained by the fact that the electron configuration of Nd^{+3} is $4f^3$ while La^{+3} is $4f^0$. In addition the mixed Fe^{3+}/Fe^{4+} would contribute to the paramagnetizaion.

For oxygen deficient samples, the mixed Fe^{3+}/Fe^{4+} are anticipated to be randomly located in Fe1 and Fe2 site of the structure. This implies that the iron in the octahedral and tetrahedral are all mixed valent state. With less oxygen in the structure, the B-site in the equatorial perovskite slabs are not truly octahedral but more like tetrahedra. In addition, the magnetic behavior could be influenced by many aspects, such as electron delocalization and unequal bond distances.

If the A- and/or B- site cation were substituted, a different magnetically ordered state was observed, i.e. $Sr_4Fe_3O_{10}$ or $PrSr_3(Fe_{1-x}Co_x)O_{10-\delta}$ system. Jantsky et al. [15] investigated the magnetic interactions in $PrSr_3(Fe_{1-x}Co_x)O_{10-\delta}$, under field cooled (FC) and zero field cooled (ZFC) condition over the temperature range 5-300 K in a high field of 0.5 T. The ZFC curve for the parent compound x = 0, shows a horizontal inflection point at 124 K, a local minimum at 160 K and a local maximum at 180 K. A Curie-Weiss fit is observed at high temperatures.

Chapter 6

Conclusion

In this study we report for preparation of phase pure $Ln_xSr_{4-x}Fe_3O_{10}$ ($0 < x \leq 1.0$) compounds for Ln = La and x = 0.75-1.0 for Ln = Nd and x = 0.25 and x = 0.75-1.0. Pure phase members in the compositional range $0 < x < 1.0$ are reported to be synthesized for the first time. $LaSr_3Fe_3O_{10}$ (x = 1.0) was synthesized both in air and Ar atmosphere. The unsatisfactory products for $0 < x < 1.0$ (Ln = La, x = 0.25, 0.5; Ln = Nd, x = 0.5) were poorly crystalline RP3 phases containing significant quantities of the corresponding RP2 analouge $(Ln,Sr)_3Fe_2O_7$ and perovskite $(Ln,Sr)FeO_3$. We expect that all compositions for $x \leq 1.0$ will exist as x = 1.0 and x = 0 are reported [44, 53, 89], and some selected compositions are made phase pure in that range in this study.

Attempts to synthesize $Ln_xSr_{4-x}Fe_3O_{10}$ (Ln = La, Nd; $x > 1.0$) with citric acid method were unsuccessful. All powder X-ray analyses proved that all samples contained in addition to a RP3 phase significant quantities of $(La,Sr)FeO_3$ and $(La,Sr)_2FeO_4$ RP1 or $(La,Sr)_3Fe_2O_7$ RP2 as main contaminant. However, it is expected that x slightly can be expanded beyond 1.25 as x = 1.25 members for La is close to phase pure. Larger x-values appear to be less promising relative to finding reported in this study and the work by Fossdal et al [95].

Rietveld refinements of Powder X-ray diffraction data show that a decrease in size of Ln^{3+} is accompanied by a slight decrease in the unit cell parameters for corresponding La and Nd variants of the RP3 phase. Further, for a given Ln^{3+} in $Ln_xSr_{4-x}Fe_3O_{10}$, the unit cell parameters also decrease with decreasing x for $0 < x \leq 1.0$.

A series of compounds of $LnSr_3Fe_3O_{10-\delta}$ (Ln = La, $0 < \delta \leq 1.32$; Ln = Nd, $0 < \delta \leq 1.22$) were obtained with δ interval of ~ 0.2. The oxygen content of the products depend on the cooling temperature. Single-phase $LnSr_3Fe_3O_{10-\delta}$ (Ln = La) annealed at high temperatures and cooled down slowly (5 ^{o}C/min in air) to room temperature gives highly oxygen generated phases with ~$O_{9.9}$. Oxygen content of ~$O_{10.0}$ per unit formula were obtained under a O_2 flow at 350 ^{o}C for 3 days. Samples with δ ~0.5 oxygen vacancies per formula unit were obtained by quenching the sample from high temperature in air. What's more, chemical transport reaction with oxygen-getter Zr gave larger oxygen deficiencies ($0.5 < \delta < \sim 1.5$).

For the $LnSr_3Fe_3O_{10-\delta}$ (Ln = La, Nd) series, (SR)XRD and Rietveld refinement show that these compounds (Ln = La, $\delta < \sim 0.5$; Ln = Nd, $\delta < \sim 0.8$) take the tetragonal RP3 structure, adopting I4/mmm space group. The unit cell parameters are a = b = 3.867 Å, c = 28.059 Å, for the fully oxidized $LaSr_3Fe_3O_{9.96}$ and a = b = 3.855 Å, c = 27.972 Å for the highly oxygen enriched $NdSr_3Fe_3O_{9.98}$. The c-axis parameter is a linear function of the oxygen stoichiometry and decreases with increasing oxygen content. It varies from 28.059 Å for $LaSr_3Fe_3O_{9.96}$ to 28.367 Å for the sample with $O_{9.25}$. On the lowering size of the lanthanide element, i.e. Nd substituting La in the composition, a similar behavior was seen. The c-axis parameter increase from 27.972 Å for nominal composition $NdSr_3Fe_3O_{9.98}$ to 28.243 Å for the sample containing 9.2 oxygen atoms per unit formula. SRXRD shows that these oxygen vacancies occur in the site situated in the equatorial plane of the central perovskite block.

The bond length and bond angles depend on the oxygen stoichiometry and on the element and site in question. The apical Fe1-O2 bond lengths are shorter than equatorial ones. The Fe1-O2 bond lengths of $NdSr_3Fe_3O_{10-\delta}$ decrease with decreasing oxygen deficiencies. An increase in the Fe2-O2 bond lengths from 2.026 Å to 2.243 Å was observed for the $O_{9.87}$ and $O_{9.21}$ samples. The (La/Sr)2 is in ninefold coordination, a monocapped square antiprism with oxygen bond distances varying from 2.410 to 2.751 Å. The (La/Sr)1-O is in a dodecahedral site with a less changing value 2.548 to 2.752 Å.

This study show that at high concentrations of oxygen vacancies ($\delta \approx 1$, occupancy of O4 site is half) in the RP3 phase, the distorted structure crystallize in the orthorhombic Bbmm space group. Increased amounts of oxygen vacancies beyond $\delta \approx 1$ are found to mainly locate at the O2 site.

According to TGA done in air, the oxidized $LnSr_3Fe_3O_{10-\delta}$ (Ln = La) samples ($\delta < 0.1$) start to loose oxygen at around 300 ^{o}C and they maintain loosing oxygen until maximum temperature is reached giving $LnSr_3Fe_3O_{9.15}$ (Ln = La, Nd). Oxygen is reversibly intercalated into the structure upon cooling, and the oxides nearly return to the original oxygen composition at room temperature. This shows that oxygen reversibly enters and leaves the oxygen lattice.

TGA analyses show further that the oxygen deficient compounds ($\delta > 0.5$) are very stable in air until the temperature is raised to some 200 ^{o}C. This observation shows that the oxygen deficient samples are quite resistant to oxygen but CO_2 and H_2O at ambient temperature. Above 200 ^{o}C oxygen absorption is observed and the oxidation reaches its maximum at about 400 ^{o}C, followed by continuous oxygen loss to 1200 ^{o}C. Cooling in air reversibly intercalates oxygen with final composition of ~$O_{9.9}$ at room temperature

M(T) data collected in ZFC and FC mode and M(H) data at 5 K of the two series of compounds $LnSr_3Fe_3O_{10-\delta}$ (Ln = La, Nd) were carried out. The Curie-Weiss temperature is negative based on rather sparse data derived from a temperature limited paramagnetic region. The value of u_{eff} per transition metal decrease with decreasing oxidation state > 3+. The gram susceptibility of $LnSr_3Fe_3O_{10-\delta}$ ($10-\delta < 9$) is higher than that of ($10-\delta \geq 9$). The M(H) curves for the samples with largest oxygen deficiencies in these two series ($10-\delta < 9$) have an S-form that indicate a small ferromagnetic component at 5 K. A quite linear M(H) curve of some composition ($10-\delta = 9.00$ for La– series, $10-\delta = 9.87$, 9.21 and 9.00 for Nd– series) suggests that these samples are antiferromagnetic. A small hysteresis loop in some compositions was observed, indicating a ferromagnetic component.

Chapter 7

Perspectives

This mater thesis work focused on the synthesis, structure evaluations, thermal analysis as well as magnetic measurements of selected members in the series $Ln_xSr_{4-x}Fe_3O_{10-\delta}$ (Ln = La, Nd; $0 < x < 4.0$; $8.5 < 10-\delta < 10$).

Optimize synthesis conditions so we can control sample prepare for all compositions within range for $x \leq 1.0$. Should be doable as $Sr_4Fe_3O_{10}$ also exist. Also focus on expanding the range for $x > 1.0$ – maybe not feasible if findings by Fossdal et al. [95] are correct.

Zr reductions for large δ – find conditions that not require adding Zr in excess.

For the two series of samples, high temperature magnetic measurements up to 1000 K using i.e. Faraday balance to clarify whether Curie-Weiss paramagnetism occurs at high temperatures, as well use this as a tool to look for indications of phase transitions.

Interesting direction to move into is controlled intercalation of H_2O and CO_2 in these oxides. Refer to work of Laurent. Then full characterization regarding structure and properties will be included.

As reported this series are promising cathode materials in SOFCs. Their conductivity at high temperatures should be explored by impedance spectroscopy. For the magnetic order and its Fe valence state Mössbauer spectroscopy and powder neutron diffraction will be most helpful.

RP3 oxides in this work studied as bulk – interesting to try to prepare these oxides as thin film using atomic layer deposition (ALD). Correlate properties films-bulk.

From the viewpoint of composition, substitution of the A-site and B-site cations as well as the ratio of cations in A-/B- site should be further explored in order to understand the family of RP3 phases.

Reference

1. Mitchell, R.H., *Perovskites: Modern and Ancient.* Almaz Press, 2002.
2. S, F., *Structure, properties, and preparation of perovskite-type compounds.* Pergamon Press in Oxford, New York 1969.
3. Navrotsky, A., *Perovskite: A Structure of Great Interest to Geophysics and Materials Science* Amer Geophysical Union, 1989.
4. Borowski, M., *Perovskites: Structure, Properties and Uses.* Nova Science Pub Inc, 2011.
5. Rose, G., *Poggendorffs Annalen der Physik und Chemie.* 1839. XXXXVIII: p. 558-560.
6. Wenk, H.-R.B., Andrei, *Minerals: Their Constitution and Origin.* Cambridge University Press, 2004: p. 413.
7. Tejuca, L. G., J. L. G. Fierro, and J. M. D. Tascón, *Structure and Reactivity of Perovskite-Type Oxides.* 1989. 36: p. 237-328.
8. Megaw, *Crystal structure of Barrium Titanite.* Nature, 15.4.1945. 155.
9. Megaw, H. D., *Temperature changes in the crystal structure of barium titanium oxide.* 1947: p. 261-283.
10. Megaw, H. D., *Proceedings of the Physical Society.* 1946. 58: p. 133-152.
11. M, G. V., *Die Naturwissenschaften.* 1926. 21: p. 477.
12. Woodward, P. M., *Octahedral tilting in Perovskite. II. Structure stabilizing forces.* acta crystallographics, 1996. B53: p. 44-46.
13. Muller, U., *Inorganic structural chemistry.* WILEY, 2007: p. 203-204.
14. *http://abulafia.mt.ic.ac.uk/publications/theses/levy/Chapter3.pdf*.
15. Jantsky, L., *Novel oxides with interesting ionic, electronic and/or magnetic properites.* University of Oslo, 2012.
16. Glazer, A. M., *The classification of tilted octahedra in perovskites.* Acta crystallographica, 1972. B28: p. 3394-3392.
17. Woodward, P. M., *Octahedral tilting in Perovskites. I. Geometrical considerations.* acta crystallographics, 1996. B53: p. 32-43.
18. Ishikawa, Y., *The Study on Substances having the Ilmenite Structure I. Physical Properties of Synthesized $FeTiO_3$ and $NiTiO_3$ Ceramics.* Journal of the Physical Society of Japan, 1956. 11(5): p. 496-501.
19. Frazer, *X-Ray and Neutron Diffraction Study of Ferroelectric PbTiO3.* Physical Review, 1955. 97(4): p. 1179-1180.
20. W. D. Kingery, H.K.B., D. R. Uhlmann, *Introduction to ceramics.* 1976: p. 926-927.
21. G. Shirane, H. D., R. Pepinsky, *Neutron Diffraction Study of Orthorhombic $BaTiO_3$.* Phys. Rev., 1957. 105(3).
22. Fierro, M. A. P. a. J. L. G., *Chemical Structures and Performance of Perovskite Oxides.* American Chemical Society, 2001. 101: p. 1981-2017.
23. HIPPLER, K., *STRUCTURE OF NA3OCL.* Acta crystallographica, 1900. 46(5): p. 736-738.
24. Roehr, C., *Crystal structure of calcium germanium oxide, Ga_3GeO.* 1995. 210: p. 798.

25. Tezuka, H., *Search for new superconductors by the Li-intercalation into layered perovskites of the Aurivillius phase.* Physica C: Superconductivity, 2008. 468(15-20): p. 1152-1154.

26. AURIVILLIUS, B., *MIXED BISMUTH OXIDES WITH LAYER LATTICES .2. STRUCTURE OF BI4TI3O12.* 1950. 1: p. 499-512.

27. A., I. B., *Cation disorder in the ferroelectric Aurivillius phase PbBi2Nb2O9: an anomolous dispersion X-ray diffraction study.* solid State ionics, 1998. 112: p. 281-289.

28. DION, M., *The new phase families* $M(I)M^2(II)Nb_3O_{10}$ *with perovskite sheets.* Materials research bulletin, 1981. 6: p. 1429-1435.

29. A. J. Jacobson, J. W. J., *Interlayer chemistry between thick transition-metal oxide layers: synthesis and intercalation reactions of* $K[Ca_2Na_{n-3}Nb_nO_{3n+1}]$. Inorganic Chemistry, 1985. 24: p. 3727-3729.

30. Bao-Wen Li, M. O., Yasuo Ebina, Tadashi C. Ozawa, Renzhi Ma,, *Impact of perovskite layer stacking on dielectric responses in* $KCa_2Na_{n-3}NbnO_{3n+1}(n=3–6)$*Dion–Jacobson homologous series.* APPLIED PHYSICS LETTERS, 2010. 96.

31. RUDDLESDEN, S. P., P, *The compound* $Sr_3Ti_2O_7$ *and its structure.* ACTA CRYSTALLOGRAPHICA, 1958. 11(1): p. 54-55.

32. Popper, S. N. R. a. P., *New compounds of the* K_2NiF_4 *type.* ACTA CRYSTALLOGRAPHICA, 1957. 10(8).

33. PLIETH, K. B., D, *DIE STRUKTUR DES KALIUMNICKEL-FLUORIDS.* Acta crystallographica, 1954. 7(10): p. 637.

34. Arumugam Manthiram, J.-H.K., Young Nam Kim, Ki-Tae Lee, *Crystal chemistry and properties of mixed ionic-electronic conductors.* J Electroceram, 2011. 27: p. 93-107.

35. Lei Yan, H. N., Craig A. Bridges, Paul A. Marshall, Joke Hadermann, *Unit-Cell-Level Assembly of Metastable Transition-Metal Oxides by Pulsed-Laser Deposition.* Angewandte Chemie, 2007. 46.

36. Kröger, F. A. and H. J. Vink, *Relations between the Concentrations of Imperfections in Crystalline Solids.* Solid State Physics, 1956. 13: p. 307-435.

37. Smyth, D. M., *DEFECTS AND ORDER IN PEROVSKITE-RELATED OXIDES.* Ann. Rev. Mater., 1985. 15: p. 329-357.

38. Smyth, D. M., *Defects and order in Perovskite-related oxides.* Ann. Rev. Mater. Sci, 1985. 15: p. 329-357.

39. L .G. Tejuca, J. L. G. F., *Properties and Applications of Perovskite-Type Oxides.* CRC Press, 1992.

40. Tofield, B. C. S., W. R, *Oxidative notstochiometry in perovskites. An experimental survery - Defect structure of an oxidized Lanthanum manganite by powder Neutron deffraction.* Solid State Chemistry, 1974. 10: p. 183-194.

41. Ole Henrik Hansteen, Helmer F., *Synthesis, Crystal Structure, and Magnetic Properties of* $La_4Co_3O_{10-\delta}$ $(0.00 \le \delta \le 0.30)$. Journal of Solid State Chemistry, 1998. 141(1): p. 212-220.

42. Ole Henrik Hansteen, Helmer F., Bjørn C. Hauback, *Crystal structure, thermal and magnetic properties of* $La_4Co_3O_9$*. Phase relations for* $La_4Co_3O_{10-\delta}$ $(0.00 \le \delta \le 1.00)$ *at 673 K.* Journal of Materials Chemistry, 1998. 8: p. 2089-2093.

43. BRINGLEY, J. T., MCELFRESH, MW, *SYNTHESIS AND CHARACTERIZATION OF A NEW LACUO3-Y PEROVSKITE.* American Chemical Society, 1990. 199: p. 359.

44. Kim, J. H., Lee, K. T, Kim, Y. N, Manthiram, A, *Crystal chemistry and electrochemical properties of* $Ln(Sr,Ca)_3(Fe,Co)_3O_{10}$ *intergrowth oxide cathodes for solid oxide fuel cells.* Journal of Materials Chemistry, 2011. 21(8): p. 2482.
45. Lee, K. T . B., D M; Manthiram, A, $Sr_{3-x}La_xFe_{2-y}Co_yO_{7-\delta}$ $(0.3 \leq x \leq 0.6$ *and* $0 \leq y \leq 0.6)$ *intergrowth oxide cathodes for intermediate temperature solid oxide fuel cells.* JOURNAL OF THE ELECTROCHEMICAL SOCIETY, 2006. 153(7): p. A1255-A1260.
46. Yutie Liu, X. T., and K. Li, *Mixed Conducting Ceramics for Catalytic Membrane Processing.* Catalysis Reviews, 2006. 48: p. 145-198.
47. Tong Jianhua, Y.W., *Methods for selection perovskitetype oxides used as mixed-conducting membranes for oxygen separation.* Membrane Science and Technology, 2003. 23: p. 33.
48. B. Raveau, C. M., M. Hervieu, D. Groult, *Crystal chemistry of High Tc superconducting Copper Oxides.* Springer Verlag, 1991.
49. C N R Rao, B.R., *Colossal Magnetoresistance, Charge ordering and related properties of manganese oxides.* World Scientific, Singapore, 1998.
50. http://www.hk-phy.org/energy/commercial/cell_phy/flash/fuel_cell_e.swf.
51. Sun, C., R. Hui, and J. Roller, *Cathode materials for solid oxide fuel cells: a review.* Journal of Solid State Electrochemistry, 2009. 14(7): p. 1125-1144.
52. Jorg Richter, P.H., *Materials design for perovskite SOFC cathodes.* Monatsh Chem, 2009. 140: p. 985-999.
53. Kim, Y. N. and A. Manthiram, *Electrochemical Properties of* $Ln(Sr,Ca)_3(Fe,Co)_3O_{10} + Gd_{0.2}Ce_{0.8}O_{1.9}$ *Composite Cathodes for Solid Oxide Fuel Cells.* Journal of The Electrochemical Society, 2011. 158(10): p. B1206.
54. Kim, J. H., Y. I. Park, and H. Kim, *A bi-layer cathode based on lanthanum based cobalt- and iron-containing perovskite and gadolinium doped ceria for thin yttria stabilized zirconia electrolyte solid oxide fuel cells.* Ceramics International, 2012. 38(8): p. 6303-6310.
55. C. Brisi, P. R., *Studies on system* $SrO\text{-}Fe_2O_3\text{-}O$. Annali di chimica, 1969. 59(5): p. 385.
56. Lee, J. Y., *The Crystal chemistry and physical properties of the triple layer perovskite intergrowths* $LaSr_3Fe_3O_{10-\delta}$ *and* $LaSr_3(Fe_{3-x}Al_x)O_{10-\delta}$. Journal of Solid State Chemistry, 1993. 103: p. 1-15.
57. D. Pelloquin, J. H., M. Giot, V. Caignaert, C. Michel, M. Hervieu, B. Raveau, *Novel, oxygen-deficient n=3 RP-Member* $Sr_3NdFe_3O_{9-\delta}$ *and its topotactic derivatives.* Chem. Mater., 2004. 16: p. 1715-1724.
58. NIKOLAY VELINOV, N.B., VLADIMIR KOZHUKHAROV, *SYNTHESIS, STRUCTURE AND CONDUCTIVITY OF LAYERED PEROVSKITES.* Ceramics, 2005: p. 29-33.
59. Cui Mingjie, Z. G., Li Qin, Liu Ting, *Studies on the structure and oxygen nonsotichometry of* $LaSr_3Fe_3O_{10-\delta}$ *mixed conductor.* Journal of Nanchang Hangkong University (Natural Science), 2007. 21(3).
60. T. Armstrong, F. P., A. Manthiram, *Synthesis, crystal chemistry, and oxygen permeation properties of* $LaSr_3Fe_{3-x}Co_xO_{10}(0 < x < 1.5)$. Solid State Ionics, 2001: p. 89-96.
61. Lehtimäki, M., *Water-containing derivative phases of the* $Sr_{n+1}Fe_nO_{3n+1}$ *series.* Journal of Solid State Chemistry, 2007. 180(11): p. 3247-3252.

62. ZHANG Guoguang , L. Q., CAO Jingqian, CUI Mingjie, *Defect structure and electrical properties of* $LaSr_3Fe_3O_{10-\delta}$. JOURNAL OF RARE EARTHS, 2010. 28(2): p. 270.
63. K. KUZUSHITA, S. M., *The Mössbauer Study of* $LaSr_3Fe_3O_{10}$ *with a Triple Layer of* FeO_6 *Octahedra.* Hyperfine Interactions, 2002. 141: p. 199-205.
64. Takahashi, H., Watanabe, Hiroshi, *Solid Alkaline Fuel Cell Composed of Layered Perovskite-Type Oxide LaSr.* 2011: p. 267-272.
65. K. Kuzushita, S. M., S. Nasua, S. Kawasaki, M. Takano, *Charge disproportionation and magnetic order of Fe in* $LaSr_3Fe_3O_{10}$. Solid State Communications, 2002. 123.
66. Ana Ecija, K.V., *Advances in Crystallization Processes.* 2012.
67. Laurent Jantsky, H. O., *Tuning of water and hydroxide content of intercalated Ruddlesden-Poper type oxides in the* $PrSr_3Co_{1.5}Fe_{1.5}O_{10-\delta}$. Inorganic Chemistry, 2012. 51(17): p. 81-91.
68. Van Arkel, A.E.d.B., J. H, *Darstellung von reinem Titanium-, Zirkonium-, Hafnium- und Thoriummetall. Zeitschrift für anorganische und allgemeine Chemie*, 1925. 148: p. 345-350.
69. C. Barry Carter, M.G.N., *Ceramic Materials: Science and Engineering.* 2007. chapter 15 Phase boundaries, particles and pores: p. 269-288.
70. W. Freidrich, P.K., M. Laue, *Interference appearances in X-rays.* Proceedings of the Bavarian Academy of Sciences, 1912: p. 303-322.
71. Hull, A.W., *A New Method of Chemical Analysis.* Chem. Soc., 1919. 41(8): p. 1168–1195.
72. G. Rosenbaum, K.C.H., *Synchrotron radiation as a source for X-ray diffraction.* Nature, 1971: p. 434-437.
73. J. W. Elmer, T.A.P., *Advanced Techniques for In-Situ Monitoring of Phase Transformations During Welding Using Synchrotron-Based X-Ray Diffraction.* 7th International Trends in Welding, 2005.
74. Young, R. A., *The Rietveld Method.* Oxford University Press, 1993.
75. Rietveld, H. M., *A profile refinement method for nuclear and magnetic structures.* CRYSTALLOGRAPHY, 1969. 2.
76. Rietveld, H. M., *Line profiles of neutron powder-diffraction peaks for structure refinement.* Acta crystallographica, 1967. 22.
77. GSAS, http://www.ccp14.ac.uk/solution/gsas/.
78. TOPAS, http://www.topas-academic.net/.
79. Fullprof, http://www.ill.eu/sites/fullprof/.
80. Furman, N., *Applications of ceric sulfate in volumetric analysis.* THE AMERICAN CHEMICAL SOCIETY, 1928.
81. KOLTHOFF, I., *VOLTAMMETRIC BEHAVIOR OF THE IRON(II)-(III) AND CERIUM(III)-(IV) COUPLES IN POTENTIOMETRIC TITRATIONS AT CONSTANT CURRENT AND AMPEROMETRIC TITRATIONS WITH 2 INDICATOR ELECTRODES.* Analytica Chimica Acta, 1957. 17: p. 329-338.
82. Rao, G. G., *Nickel phthalocyanine sulphonic acid as a redox indicator in cerimetry.* FRESENIUS ZEITSCHRIFT FUR ANALYTISCHE CHEMIE, 1962. 190(3): p. 213-222.
83. Haines, P. J., *Thermal methods of analysis principles, applications and problems.* 1995.

84. Hysteresis loop, *http://www.ndted.org/EducationResources/CommunityCollege/MagParticle/Physics/HysteresisLoop.htm.*
85. *Schematic of TGA instrument. http://www.netzschthermalanalysis.com/uploads/tx_nxnetzschmedia/files/STA_449_F1_E_0413.pdf.*
86. PPMS, *http://www.qdusa.com/sitedocs/productBrochures/16TPPMS7.pdf*.
87. http://balance.balances.com/scales/40.
88. *http://www.bruker.com/products/x-ray-diffraction-and-elemental-analysis/single-crystal-x-ray-diffraction/d8-venture/overview.html*.
89. Boklund, H., *Ruddlesden-Popper phases in the Sr-Fe-O system.* KJM2010 Undergraduate Research I, 2013.
90. Mingjie, C., *Fabrication of* $LaSr_3Fe_3O_{10-\delta}$ *and* $LaSr_3(Fe_{3-x}Al_x)O_{10-\delta}$ *and investigation of their properties.* 2010.
91. Jantsky, L., *Temperature dependant X-ray diffraction study of* $PrSr_3Co_{1.5}Fe_{1.5}O_{10-d}$*; n= 3 Ruddlesden-Popper phase.* Zeitschrift für Kristallographie, 2009. 224(5-6): p. 295-301.
92. Brown, I.D., *Bond Valences-A Simple Structural Model for Inorganic Chemistry.* Chem. Soc. Rev., 1978. 7: p. 359-376.
93. O'Keeffe, M., *A Method for Calculating Bond Valences in Crystals.* Acta crystallographica, 1990. A46: p. 138-142.
94. Tugova, E.A., *A Comparative Analysis of the Formation Processes of Ruddlesden–Popper Phases in the* La_2O_3*–SrO–*M_2O_3*(M = Al, Fe) Systems.* Glass Physics and Chemistry, 2009. 35(4): p. 416-422.
95. Anita Fossdal, M.-A.E., Tor Grande, *Phase Relations In The Pseudo-Ternary System* La_2O_3*–SrO–*Fe_2O_3. Communications of the American Ceramic Society, 2005. 88(7): p. 1988-1991.
96. A. Fossdal, M.-A.E., T. Grande, *Phase Equilibria in the Pseudo-binary System SrO-*Fe_2O_3. J. Am. Cera. Soc., 2004. 87: p. 1952-1958.
97. Database of Ionic radii. *http://abulafia.mt.ic.ac.uk/shannon/ptable.php*

Appendix

A Temperature gradient in furnace used for Zr-reduction experiment

To get large oxygen deficient RP3 phases, a quartz reactor with RP3 oxide and Zr were kept at 500 ^{o}C and 750 ^{o}C, respectively. A tube furnace was calibrated to find the temperature gradient of the furnace, to define positions for the Zr and oxide in the quartz reactor.

The calibration procedure started measuring the temperature (T = 750 ^{o}C) at a fixed defined position using two thermocouples. When the furnace temperature had stabilized at 750 ^{o}C one of the thermocouples was manually moved a given distance (2 cm) from the fixed predefined point. When the temperature controller for the moved thermocouple indicated stable temperature, the temperature and position was recorded. This procedure was repeated until the furnace we have reached the position in the furnace that was at some 300 ^{o}C.

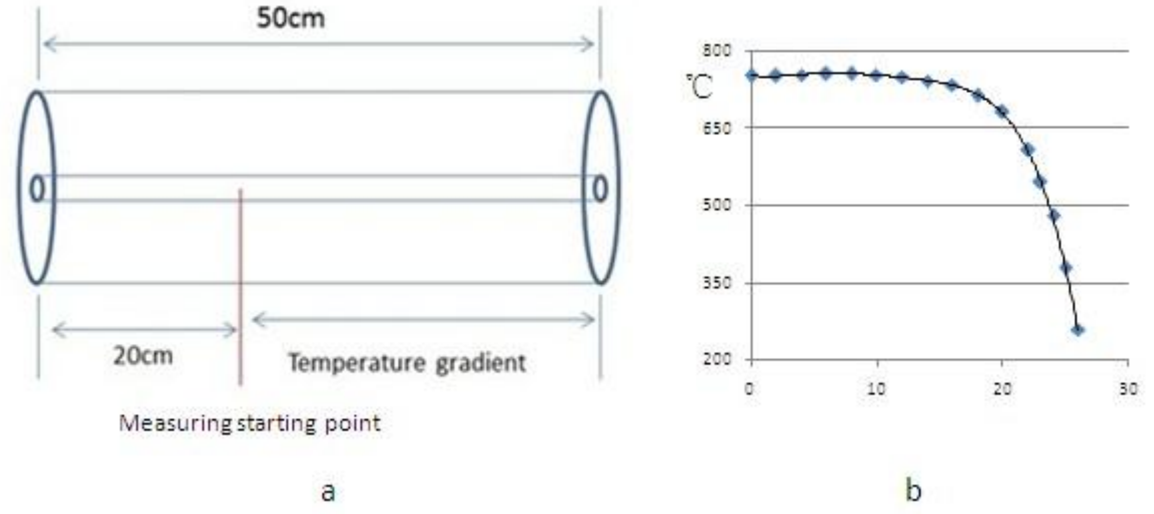

a

b

Figure A-1. Schematic and data of calibrated temperature gradient in furnace. (a) Tube furnace and its starting point of measurement. (b) Temperature gradient curve for the calibrated tube furnace.

As shown in Figure A-1, the curve illustrates the temperature gradient of the tube furnace. To get the temperature of 500 ^{o}C and 750 ^{o}C, the distance of the oxide and Zr is in the range of 12 cm to 24 cm.

B Powder X-ray diffraction of gravimetrically determined chemicals

Powder XRD diffraction patterns obtained after having calcined $SrCO_3$, $Fe(COO)_2·2H_2O$ and $(NH_4)_2SO_4·FeSO_4·6H_2O$ to its corresponding oxides, SrO and Fe_2O_3 are reported in Figures A-2.

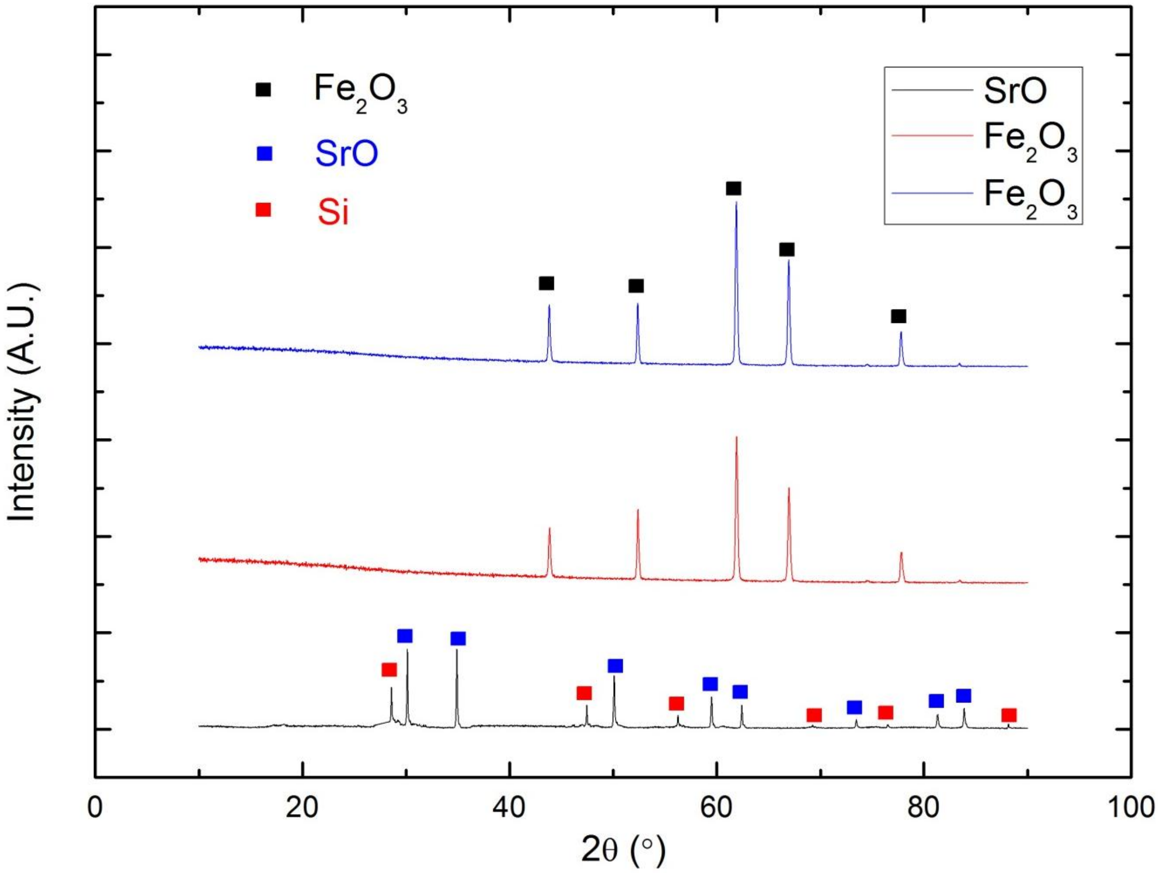

Figure A-2. Powder X-ray diffraction patterns of SrO and Fe_2O_3 formed during the gravimetrically decomposed $SrCO_3$, $Fe(COO)_2·2H_2O$ and $(NH_4)_2SO_4·FeSO_4·6H_2O$. Black curve is SrO formed from $SrCO_3$ while blue and red curves are Fe_2O_3 decomposed from $Fe(COO)_2·2H_2O$ and $(NH_4)_2SO_4·FeSO_4·6H_2O$ respectively. Blue, red and black filled squares indicate the Bragg reflections of the respective phase of SrO, Si and Fe_2O_3. Powder X-ray diffraction patterns were collected using monochromatic Cu $K_{\alpha1}$ ($\lambda = 1.540598$ Å) radiation.

C Powder X-ray diffractorams of $Ln_xSr_{4-x}Fe_3O_{10}$ (Ln = La, Nd; 0 < x < 4)

Powder X-ray diffraction patterns of some of selected samples in the series $Ln_xSr_{4-x}Fe_3O_{10}$ (Ln = La, Nd) obtained via different annealing conditions not presented in the result section. For all samples, the annealing conditions are described in Tables 10 and 11, result section.

C.1 $LaSr_3Fe_3O_{10}$ prepared in air and Ar atmosphere

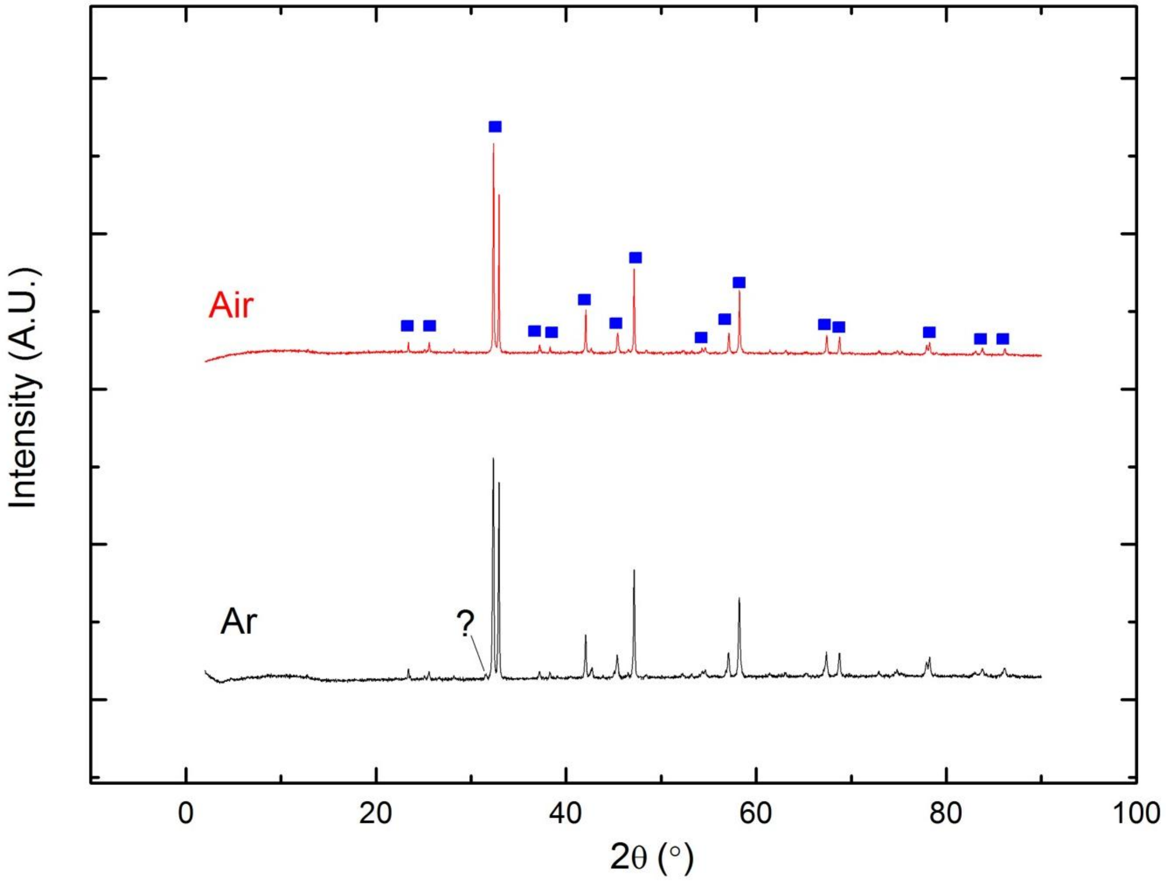

Figure A-3. Powder X-ray diffraction patterns of $LaSr_3Fe_3O_{10}$ annealed in air (1250 ^oC) and Ar (1100 ^oC). Blue filled squares indicate the Bragg reflections of the RP3 phase. A very low intensity peak (marked with "?") is unidentified. Powder X-ray diffraction patterns were collected using monochromatic Cu $K_{\alpha 1}$ (λ = 1.540598 Å) radiation.

C.2 $LaSr_3Fe_3O_{10}$ prepared at various conditions

Table A-1. Refined data for $LaSr_3Fe_3O_{10}$ prepared at various conditions

Batch	Annealing condition	Phase	Phase fraction	*GOF*	R_{exp}	R_{wp}	R_p
[1]1	1050 °C × 15 h 1250 °C × 25 h	Perovskite	18.16%	1.13	7.34%	8.27%	6.65%
		RP3	80.70%				
[1]2	1100 °C × 48 h 1100 °C × 24 h	Perovskite	30.96%	1.2	7.19%	8.66%	6.82%
		RP3	69.04%				
[2]3	1050 °C × 15 h 1350 °C × 25 h	Perovskite	30.71%	1.48	3.98%	5.87%	4.47%
		RP3	69.29%				
[3]4	1050 °C × 15 h 1250 °C × 25 h	Perovskite	33.61%	2.22	2.86%	6.36%	4.34%
		RP3	66.39%				
[4]5	1050 °C × 15 h 1250 °C × 25 h	Perovskite	30.77%	1.52	2.87%	4.38%	3.25%
		RP3	69.23%				
[1]6	1050 °C × 15 h 1250 °C × 25 h 1350 °C × 12 h	Perovskite	22.19%	1.34	7.38%	9.88%	7.7%
		RP2	8.48%				
		RP3	69.33%				

1 Pellet taken in and out of furnace at room temperature

2 Pellet put into the furnace at 1050 °C and 1250 °C and taken out at the same temperature, and allowed to cool down in air

3 Pellet put into the furnace at 1050 °C and 1250 °C and taken out at the same temperature, and allowed to cool down in a desiccator

4 Pellet put into the furnace at room temperature and taken out at high temperature, and allowed to cool down in desiccator

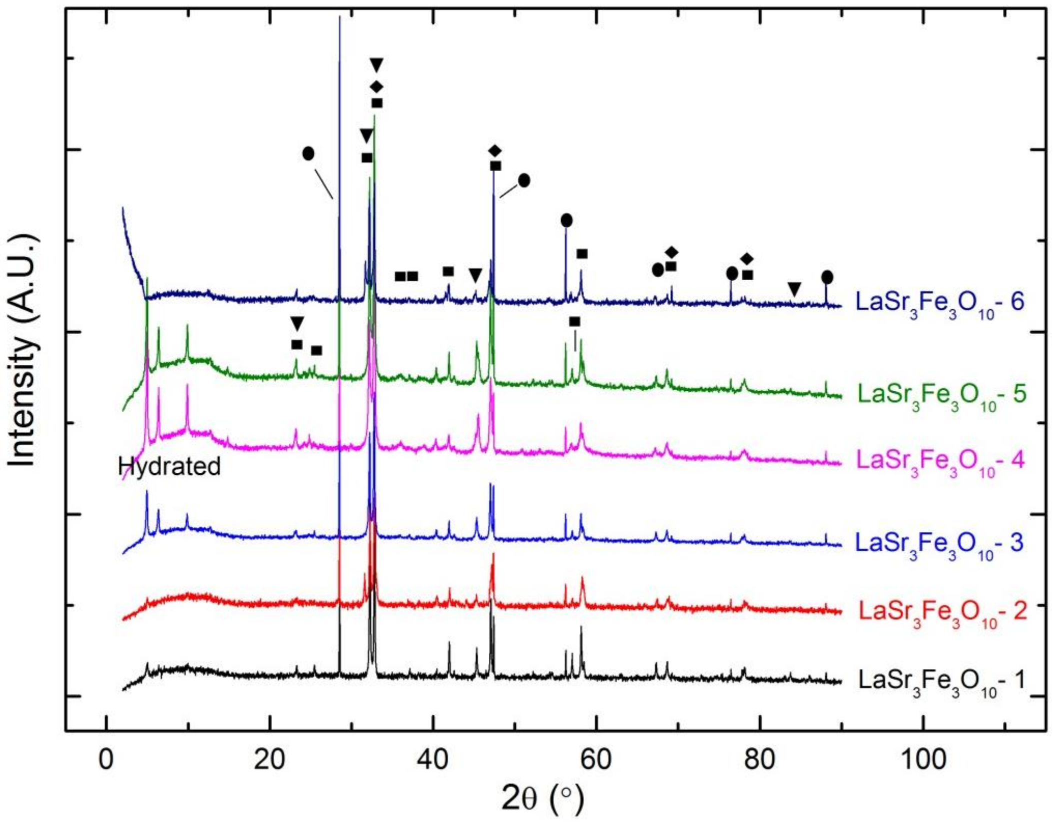

Figure A-4. Powder X-ray diffraction patterns of $LaSr_3Fe_3O_{10}$ obtained from different sintering conditions. Powder X-ray patterns were collected using monochromatic Cu $K_{\alpha1}$ (λ = 1.540598 Å) radiation.

C.3 $La_{1.25}Sr_{2.75}Fe_3O_{10}$

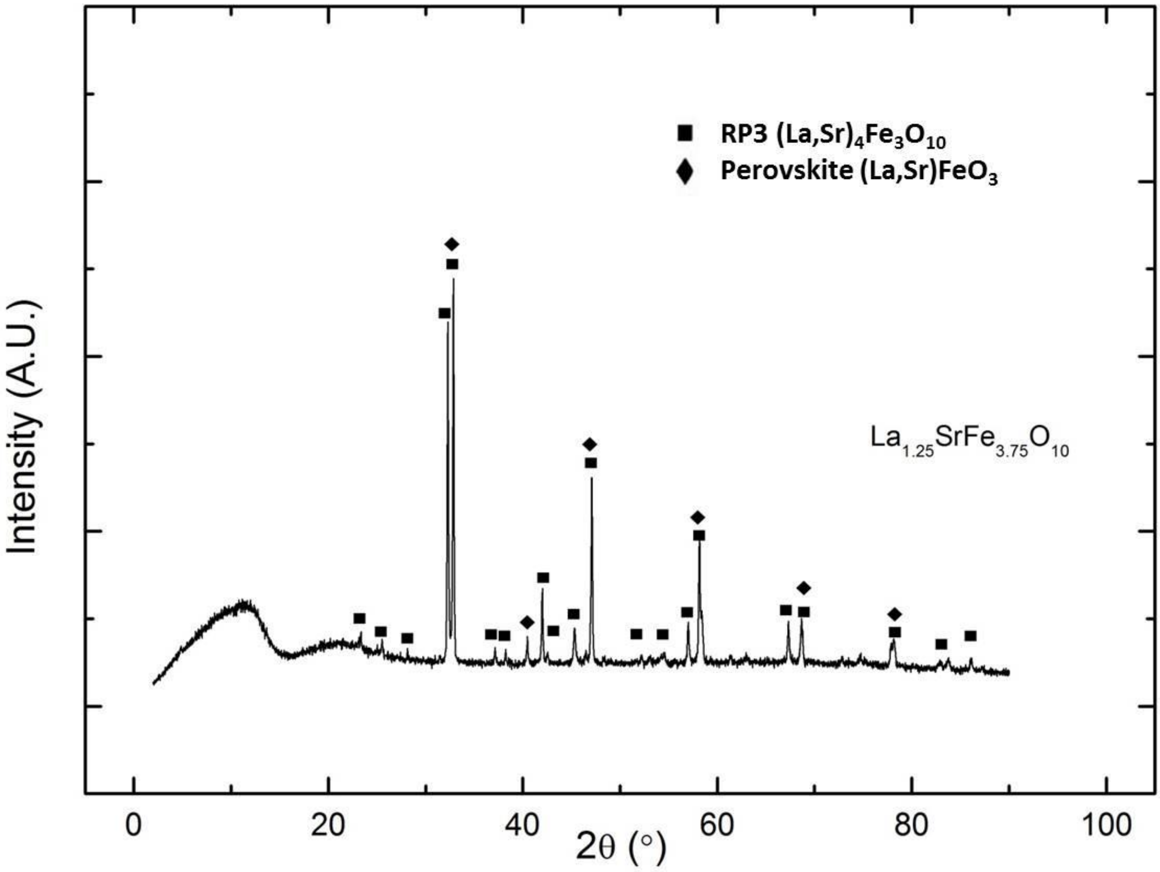

Figure A-5. Powder X-ray diffraction patterns of $La_{1.25}Sr_{2.75}Fe_3O_{10}$ annealed in air at 1300 ^{o}C. Powder X-ray diffraction patterns were collected using monochromatic Cu $K_{\alpha1}$ (λ = 1.540598 Å) radiation. The refined phase fractions are 74.23% RP3 phase and 25.77% perovskite $(La,Sr)FeO_3$ according to TOPAS. GOF = 1.27, R_{exp} = 4.17%, R_{wp} = 5.31%, R_p = 4.1%.

C.4 $La_{1.5}Sr_{2.5}Fe_3O_{10}$ prepared at various conditions

Table A-2. Attempts for synthesizing $La_{1.5}Sr_{2.5}Fe_3O_{10}$ and refined data

Batch	Annealing condition	Phase	Phase fraction	*GOF*	R_{exp}	R_{wp}	R_p
1	[1]1100 °C × 12 h (Ar) 1100 °C × 12 h (Ar)	Perovskite	78.08%	2.4	3.46%	8.29%	5.54%
		RP1	7.79%				
		RP3	14.12%				
2	[2]1000 °C × 12 h 1250 °C × 12 h 1250 °C × 12 h	Perovskite	5.83%	3.26	3.87%	12.62%	8.1%
		RP1	53.88%				
		RP3	40.29%				

1 Pellets were fired at 1100 °C for 12 hours under the Ar flow.

2 Pellets were fired at 1100 °C for 12 hours in air.

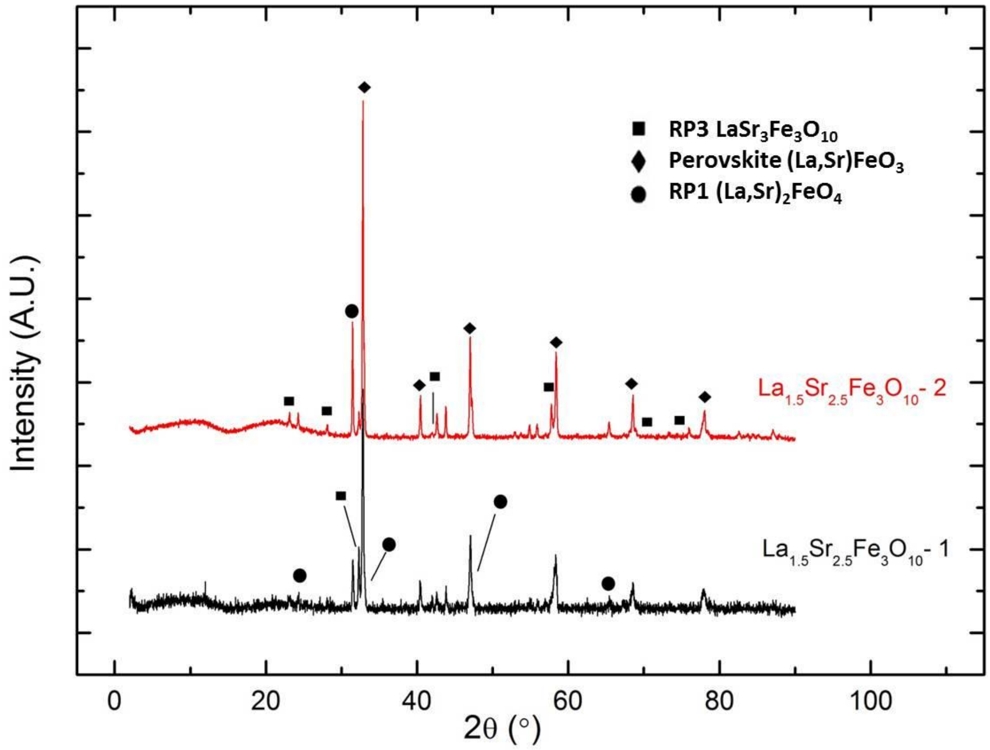

Figure A-6. Powder X-ray diffraction patterns of $La_{1.5}Sr_{2.5}Fe_3O_{10}$ obtained from sintering conditions. Powder X-ray patterns were collected using monochromatic Cu $K_{\alpha 1}$ (λ = 1.540598 Å) radiation.

C.5 $La_2Sr_2Fe_3O_{10}$ prepared at various conditions

Table A-3. Refined data for $La_2Sr_2Fe_3O_{10}$ under different synthetic condition

Annealing condition	Phase	Phase fraction	*GOF*	R_{exp}	R_{wp}	R_p
1100 °C (Ar) × 12 h × 2	Perovskite	44.05%	1.63	3.82%	6.21%	4.74%
	RP1	17.06%				
	RP3	38.4%				
1000 °C × 12 h 1200 °C × 12 h 1200 °C × 12 h	Perovskite	21.37%	2.08	3.2%	6.67%	4.52%
	RP2	24.61%				
	RP3	54.02%				
1000 °C × 12 h 1250 °C × 12 h 1250 °C × 12 h	Perovskite	44.73%	2.29	3.54%	8.1%	5.48%
	RP1	16.42%				
	RP3	38.85%				
1000 °C × 12 h 1300 °C × 12 h 1300 °C × 12 h	Perovskite	46.34%	2.34	3.7%	8.67%	5.8%
	RP1	14.57%				
	RP3	39.09%				

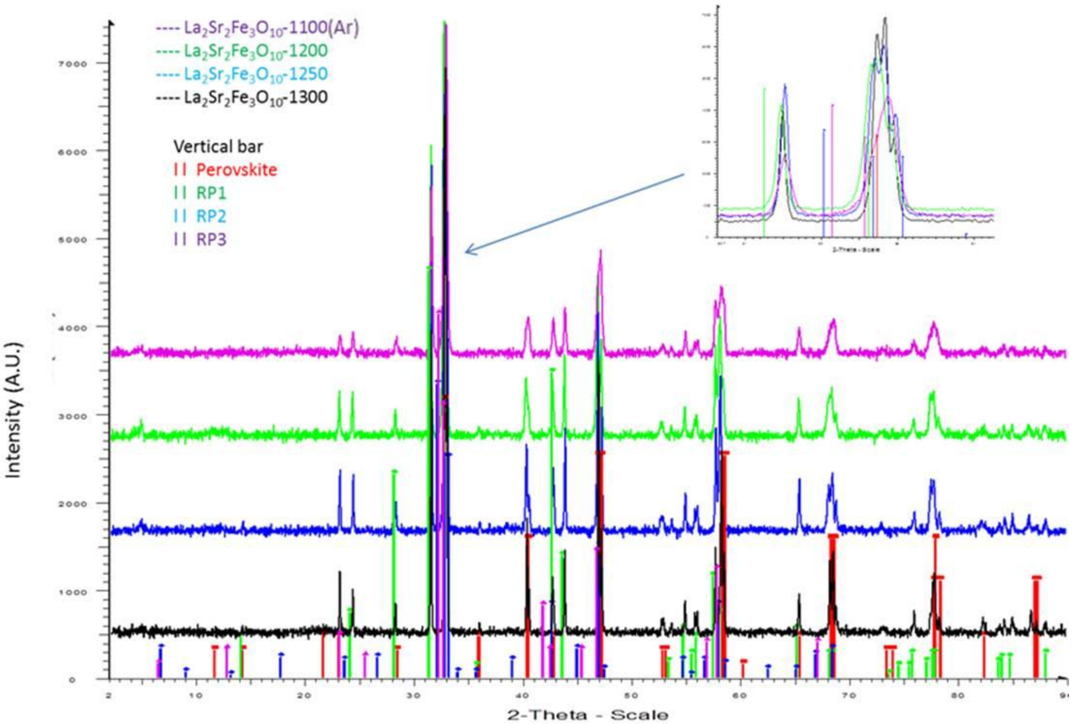

Figure A-7. Powder X-ray diffraction pattern of sintered $La_2Sr_2Fe_3O_{10}$ series under different conditions. The inset shows the peak splitting between 2θ = 30.4° and 2θ = 34.7°. Powder X-ray diffraction patterns were collected using monochromatic Cu $K_{\alpha1}$ (λ = 1.540598 Å) radiation.

C.6 $La_3SrFe_3O_{10}$ prepared at various conditions

Table A-4. Attempts for synthesizing compound $La_3SrFe_3O_{10}$ and refined data

Batch	Annealing condition	Phase	Phase fraction	*GOF*	R_{exp}	R_{wp}	R_p
1	1000 °C × 12 h	Perovskite	78.08%	2.4	3.46%	8.29%	5.54%
	1250 °C × 12 h	RP1	7.79%				
	1250 °C × 12 h	RP3	14.12%				
2	1000 °C × 12 h	Perovskite	5.83%	3.26	3.87%	12.62%	8.1%
	1300 °C × 12 h	RP2	53.88%				
	1300 °C × 12 h	RP3	40.29%				
3	1000 °C × 12 h	Perovskite	74.19%	1.61	5.66%	9.1%	7.13%
	1350 °C × 12 h	RP2	4.78%				
	1350 °C × 12 h	RP3	21.03%				

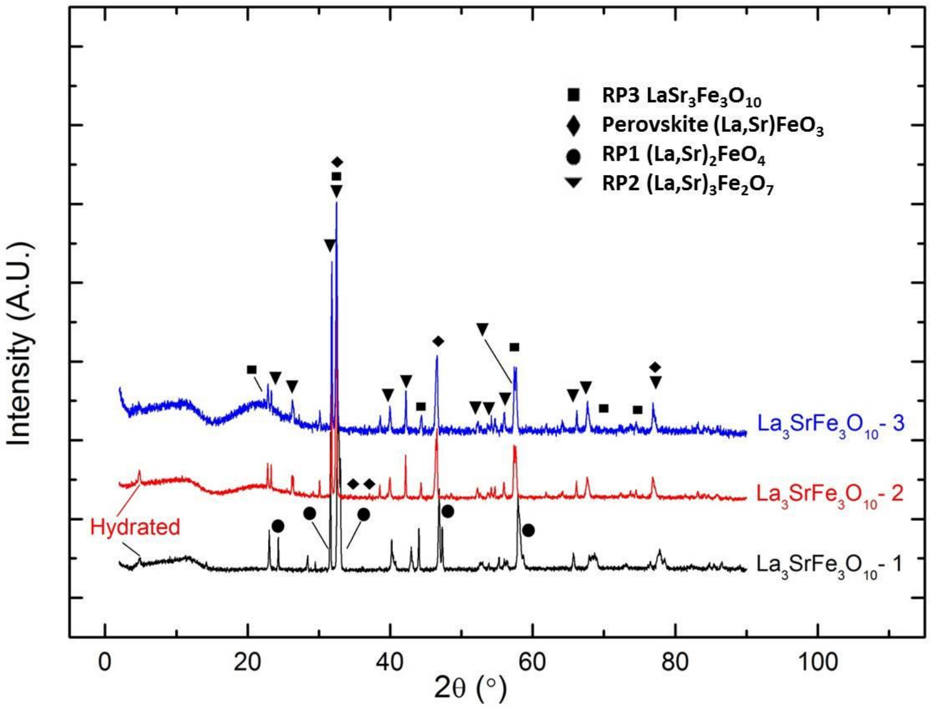

Figure A-B. Powder X-ray diffraction patterns of $La_3SrFe_3O_{10}$ obtained from sintering conditions. Powder X-ray patterns were collected using monochromatic Cu $K_{\alpha 1}$ (λ = 1.540598 Å) radiation.

C.7 $NdSr_3Fe_3O_{10}$ prepared at various conditions

Table A-5. Attempts for synthesizing compound $NdSr_3Fe_3O_{10}$ and refined data

Batch	Annealing condition	Phase	Phase fraction	*GOF*	R_{exp}	R_{wp}	R_p
1	1100 °C × 48 h 1100 °C × 48 h	Perovskite	35.1%	1.19	6.59%	7.87%	6.21%
		RP2	3.42%				
		RP3	61.48%				
2	1050 °C × 15 h 1250 °C × 25 h	Perovskite	49.54%	1.12	9%	10.08%	7.92%
		RP2	4.25%				
		RP3	46.21%				
3	1050 °C × 15 h 1350 °C × 25 h	Perovskite	36.89%	1.24	9.34%	11.56%	8.99%
		RP3	63.11%				
4	1050 °C × 15 h 1250 °C × 25 h 1350 °C × 24 h	Perovskite	37.34%	1.17	9.48%	11.1%	8.81%
		RP3	62.66%				
5	1050 °C × 15 h 1250 °C × 25 h 1350 °C × 25 h	Perovskite	19.31%	1.52	2.87%	4.38%	3.25%
		RP1	3.04%				
		RP3	77.65%				
6	1000 °C × 12 h 1350 °C × 12 h 1350 °C × 12 h	RP3	100%	1.29	3.86%	5%	3.84%

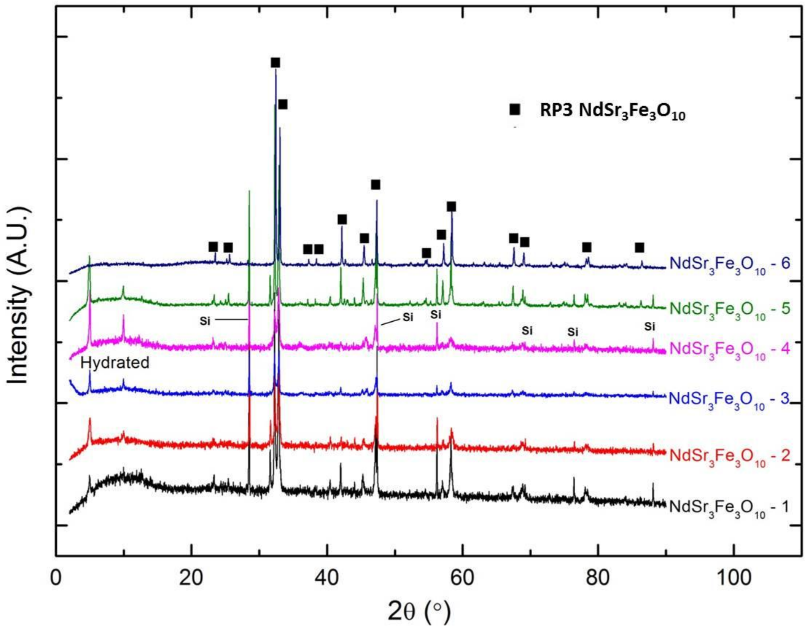

Figure A-9. Powder X-ray diffraction patterns of $NdSr_3Fe_3O_{10}$ obtained from different sintering conditions. Powder X-ray diffraction patterns were collected using monochromatic Cu $K_{\alpha 1}$ (λ = 1.540598 Å) radiation.

C.8 $Nd_{1.25}Sr_{2.75}Fe_3O_{10}$ prepared at various conditions

Table A-6. Attempts for synthesizing compound $Nd_{1.25}Sr_{2.75}Fe_3O_{10}$ and refined data

Batch	Annealing condition	Phase	Phase fraction	*GOF*	R_{exp}	R_{wp}	R_p
1	1000 ^{o}C × 12 h	Perovskite	81.8%	1.27	5.83%	7.4%	5.62%
	1250 ^{o}C × 12 h	RP1	15.60%				
	1250 ^{o}C × 12 h	RP3	2.59%				
2	1000 ^{o}C × 12 h	Perovskite	83.69%	1.10	12.36%	13.56%	10.65%
	1300 ^{o}C × 12 h	RP1	15.62%				
	1300 ^{o}C × 12 h	RP3	0.69%				
3	1000 ^{o}C × 12 h	Perovskite	80.15%	1.36	5.39%	7.33%	5.39%
	1350 ^{o}C × 12 h	RP1	4.71%				
	1350 ^{o}C × 12 h	RP3	15.14%				
4	1000 ^{o}C × 12 h	Perovskite	79.85%	1.27	5.71%	7.27%	5.37%
	1400 ^{o}C × 12 h	RP1	14.6%				
	1400 ^{o}C × 12 h	RP3	5.54%				

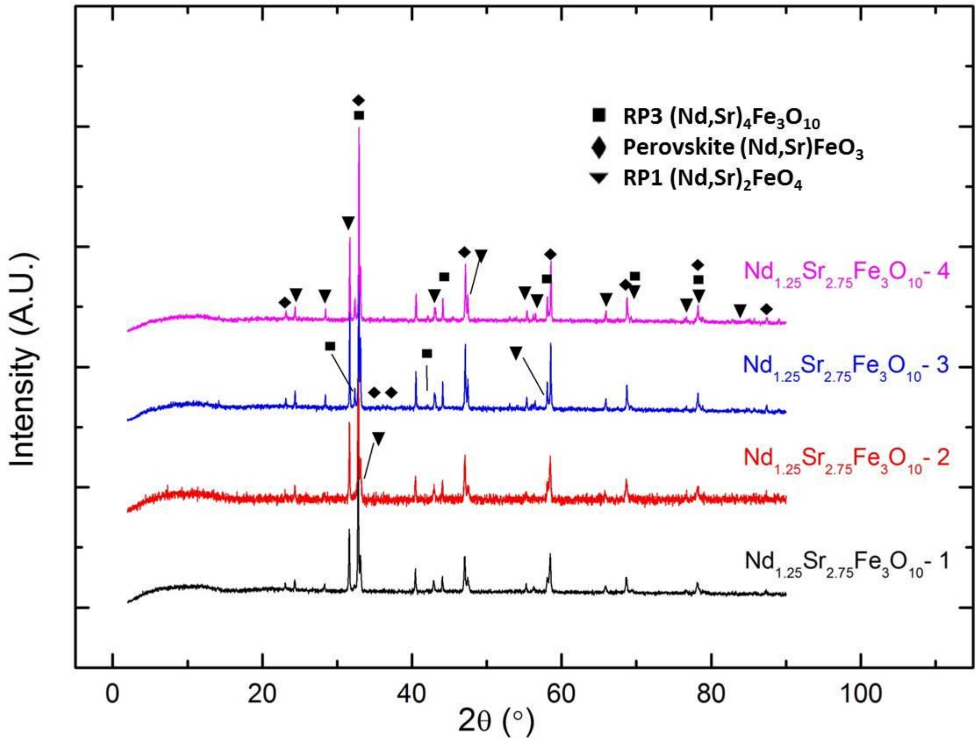

Figure A-10. Powder X-ray diffraction patterns of $Nd_{1.25}Sr_{2.75}Fe_3O_{10}$ obtained from sintering conditions. Powder X-ray diffraction patterns were collected using monochromatic Cu $K_{\alpha1}$ (λ = 1.540598 Å) radiation.

C.9 $Nd_2Sr_2Fe_3O_{10}$ prepared at various conditions

Table A-7. Attempts for synthesizing compound $Nd_2Sr_2Fe_3O_{10}$ and refined data

Batch	Annealing condition	Phase	Phase fraction	*GOF*	R_{exp}	R_{wp}	R_p
1	1050 °C × 15 h 1350 °C × 25 h	Perovskite	76.21%	1.23	8.42%	10.33%	8.06%
		RP1	11.34%				
		RP3	12.45%				
2	1050 °C × 15 h 1400 °C × 25 h	Perovskite	84.52%	1.99	3.06%	6.09%	4.45%
		RP1	11.89%				
		RP3	3.59%				
3	1050 °C × 15 h 1450 °C × 25 h	Perovskite	80.12%	1.24	9.34%	11.56%	8.99%
		RP1	15.99%				
		RP3	3.89%				
4	1050 °C × 15 h 1250 °C × 25 h 1350 °C × 24 h	Perovskite	81.41%	1.19	9.76%	11.56%	8.95%
		RP1	17.26%				
		RP3	1.33%				
5	1050 °C × 15 h 1250 °C × 25 h	Perovskite	73.09%	1.49	7%	10.44%	7.37%
		RP1	20.34%				
		RP3	6.57%				

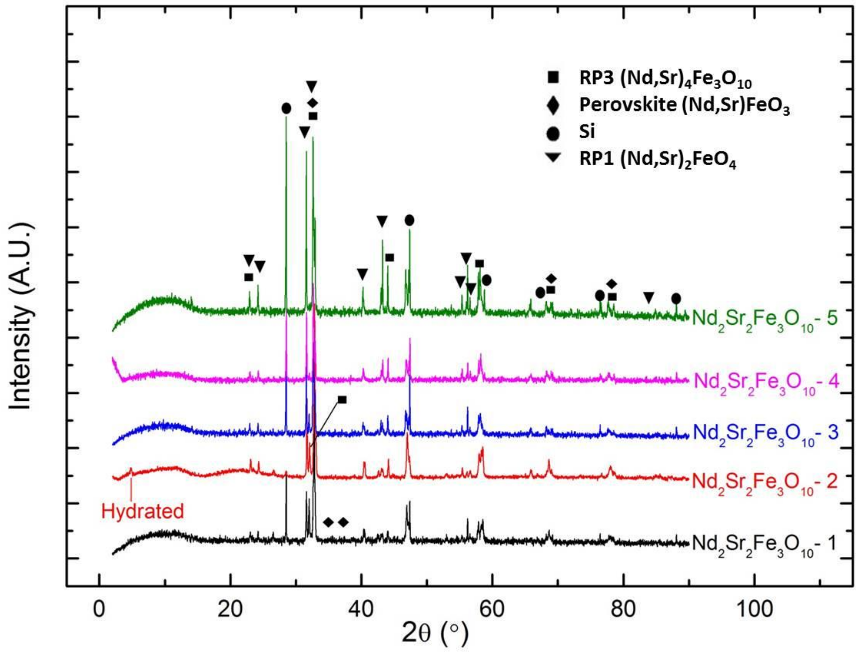

Figure A-11. Powder X-ray diffraction patterns of $Nd_2Sr_2Fe_3O_{10}$ obtained from sintering conditions. Powder X-ray diffaction patterns were collected using monochromatic Cu $K_{\alpha 1}$ (λ = 1.540598 Å) radiation.

C.10 $Nd_3SrFe_3O_{10}$ prepared at various conditions

Table A-8. Attempts for synthesizing compound $Nd_3SrFe_3O_{10}$ and refined data

Batch	Annealing condition	Phase	Phase fraction	*GOF*	R_{exp}	R_{wp}	R_p
1	1000 ^oC × 12 h	Perovskite	71.37%	2.32	3.42%	7.94%	5.15%
	1250 ^oC × 12 h	RP2	6.62%				
	1250 ^oC × 12 h	RP3	22.01%				
2	1000 ^oC × 12 h	Perovskite	69.45%	2.1	3.76%	7.91%	5.91%
	1300 ^oC × 12 h	RP2	24.3%				
	1300 ^oC × 12 h	RP3	6.25%				
3	1000 ^oC × 12 h	Perovskite	74.19%	2.18	3.63%	7.93%	5.27%
	1350 ^oC × 12 h	RP2	4.78%				
	1350 ^oC × 12 h	RP3	21.03%				

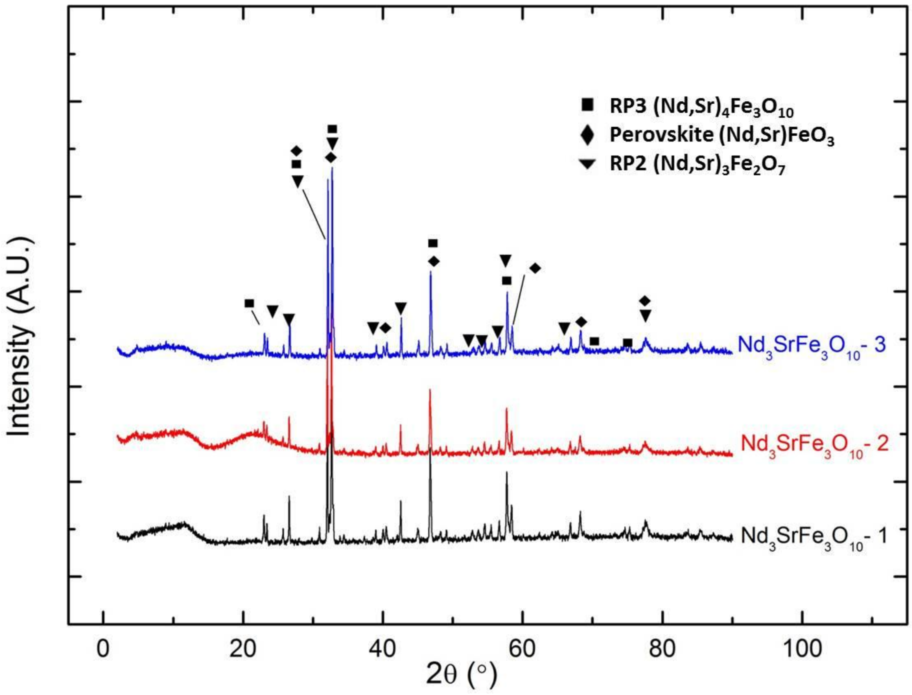

Figure A-12. Powder X-ray diffraction patterns of $Nd_3SrFe_3O_{10}$ obtained from sintering conditions. Powder X-ray diffraction patterns were collected using monochromatic Cu $K_{\alpha1}$ (λ = 1.540598 Å) radiation.

D Calculations for determining of oxygen content with temperature

The TGA raw data of mass change between 30 °C and 1200 °C in an air atmosphere was read from the TGA curves (see Table A-9). It is assumed that only oxygen was lost and intercalated upon heating and cooling. $LaSr_3Fe_3O_{10-\delta}$ is taken as an example in the calculations. Cerimetric titration gave the oxygen content as $10–\delta_1$.

Table A-9. Raw data obtained from TGA

Temperature °C		Mass g	
T_1	30.059	M_1	100
T_2	35.54524	M_2	99.99148
T_3	36.885	M_3	99.98549
T_4	39.59652	M_4	99.98517
T_5	43.95576	M_5	99.98694
T_6	50.15571	M_6	99.9847
……	……	……	……

The formula weight of $LaSr_3Fe_3O_{10-\delta 1}$ is denoted as FW_1 and calculated using following procedure:

Assume that the initial sample mass is 100 g, so the mole of the sample at T_1 was:

$$n_1 = \frac{100}{Fw_1}\ mol \qquad \text{Equation A-1}$$

When temperature is increased to T_2, the mass change of the sample is M_2-100 g, and therefore the change of the mole of oxygen (denated as $\delta_1 - \delta_2$) involved is:

$$\delta_1 - \delta_2 = \frac{M_2 - 100}{n_1 * FW_O} \qquad \text{Equation A-2}$$

where FW_O is the relative atomic mass of oxygen.

Thus the calculated oxygen content at T_2 is

$$10 - \delta_1 + \frac{M_2 - 100}{n_1 * FW_O} \qquad \text{Equation A-3}$$

Likewise, the oxygen content at other temperatures can also be calculated.

E Calculation of oxygen content of reduced $LnSr_3Fe_3O_{10}$ (Ln = La, Nd) via thermogravimetric analysis

For the reduced sample, the oxygen content can be calculated using the thermogrametric data under the assumption that the sample not re-oxidizes before the TGA experiments is started and the final oxygen stoichiometry is $O_{9.90}$.

Table A-10. Raw data obtained from TGA

Temperature °C		Mass g	
T_1	30.06	M_1	100
T_2	35.45	M_2	99.99148
T_3	36.85	M_3	99.98549
……	……	……	……
$T_{n/2}$	1200	$M_{n/2}$	100.31149
……	……	……	……
T_{final}	30.02	M_{final}	101.77123

$LaSr_3Fe_3O_{10-\delta 1}$ is taken as an example. The formula weight of $LaSr_3Fe_3O_{9.9}$ is denated as $FW_{O9.9}$, and the mole of sample at T_{final} is of

$$n_{final} = \frac{M_{final}}{FW_{O9.9}} \qquad \text{Equation A-4}$$

The formula weight of $LaSr_3Fe_3$ is FW_1 and the mass of this part keeps stable as

$$m = FW_1 n_{final} \qquad \text{Equation A-5}$$

As a result, the oxygen content of the sample at T_1 is

$$10 - \delta_1 = \frac{M_1 - \mathrm{m}}{n_{final} \times FW_O} \qquad \text{Equation A-6}$$

where FW_O is the relative atomic mass of oxygen.

The oxygen content at other temperatures can be calculated using the same procedure.

F Calculations of cerimetric titration

The principle of cerimetric titration together with some equations involved are presented in section 2.4. Since Mohr salt only reduce iron in the RP oxide to Fe (III) we define iron as having average valence 3+x; or Fe^{3+x}. We set up the calculations according to this to find x (and δ) in Fe^{3+x} for $LnSr_3Fe_3O_{10-\delta}$:

$$FW_{LnSr3Fe3O10-\delta} = FW_{LnSr3Fe3O9} + 3 \times x/2\ FW_o \qquad \text{Equation A-7}$$

Known amounts of RP3 oxide (50 mg) and Mohr salt (in excess to reduce all the high valent cations and consume around 8 mL 0.1 M $Ce(SO_4)_2$) were put in a beaker with Ar flowing as a protecting blanket. Both the oxides and Mohr salt were dissolved simultaneously in diluted HNO_3, Fe^{3+x} would be released from the oxide and react with Fe^{2+}.

$$x\ Fe^{2+}(\text{Mohr}) + Fe^{3+x}(\text{oxide}) \rightarrow (1+x)\ Fe^{3+} \qquad \text{Equation A-8}$$

After the reaction is completes, there were only Fe^{2+} and Fe^{3+} left in the solution, as shown in Equation A-9. Consumed Mohr salt depends on x.

$$n\ Fe^{2+}(\text{left}) = n\ Fe^{2+}(\text{Mohr}) - 3n\ x\ Fe^{3+x}(\text{oxide}) \qquad \text{Equation A-9}$$

One drop of Ferroin was added to the solution, giving a light red color. Then 0.1 M $Ce(SO_4)_2$ were used to titrate the solution until critical point arrives where the color changes to light green.

$$Ce^{4+} + Fe^{2+} \rightarrow Ce^{3+} + Fe^{3+} \qquad \text{Equation A-10}$$

The consumed Ce4+ oxidized the remaining Fe2+ in the solution as Equation A-10 illustrates:

$$n\ Ce^{4+} = n\ Fe^{2+}(\text{left}) \qquad \text{Equation A-11}$$

Combining Equation A-9 and A-11 gives:

$$n\ Ce^{4+} = n\ Fe^{2+}(\text{Mohr}) - 3n\ x\ Fe^{3+x}(\text{oxide}) \qquad \text{Equation A-12}$$

Then the calculated mole of oxide is:

$$n\ Fe^{3+x}(\text{oxide}) = (n\ Fe^{2+}(\text{Mohr}) - n\ Ce^{4+})/3x \qquad \text{Equation A-13}$$

The mole of oxide can also be derived as mass (m(oxide)) divided by formula weight ($FW_{LnSr3Fe3O10-\delta}$).

$$n\ Fe^{3+x}(\text{oxide}) = m(\text{oxide})/\ (FW_{LnSr3Fe3O9} + 3 \times x/2\ FW_o) \qquad \text{Equation A-14}$$

Equation A-13 and A-14 gives

$$\mathbf{(n\ Fe^{2+}(Mohr) - n\ Ce^{4+})/3x = m(oxide)/\ (FW_{LnSr3Fe3O9} + 3 \times x/2\ FW_o)} \qquad \textbf{Equation A-15}$$

Find x in Equation A-15

$$x = \frac{[nFe^{2+}(Mohr) - nCe^{4+}]\ Fw_{LaSr3Fe3O9}}{3m(oxide) - \frac{3}{2} FW_O [nFe^{2+}(Mohr) - nCe^{4+}]} \qquad \textbf{Equation A-16}$$

where $FW_{LnSr3Fe3O9}$ is the formula weight of $LaSr_3Fe_3O_9$, see equation A-7.

FW_O is the formula weight of oxygen.

m(oxide) is the weight of RP3 oxide in this case (read from the balance).

nFe^{2+}(Mohr) is the mole of Mohr salt, can be calculated as the mass (read from the balance) divided by its formula weight (this value would be determine gravimetrically prior to use, for results see section 4.1.1 on Page 58).

nCe^{4+} is the mole consumed $Ce(SO_4)_2$ obtained from the molarity times volume (read from the buret). The real molarity of $Ce(SO_4)_2$ would be determined from three parallel measurements at the onset of every titration.

Ruddlesden-Popper phases $LnSr_3Fe_3O_{10-\delta}$ with Sr(II) and Ln(III) (Ln = La, Nd) as A-site cations and oxygen has 2– state valence. As assumed, Iron has the average oxidation states 3+x. A simple Equation A-17 is established based on the electroneutrality principle.

$$\mathbf{3 + 2 \times 3 + 3 \times (3 + x) = 2 \times (10 - \delta)} \qquad \textbf{Equation A-17}$$

The oxygen nonstoichiometry δ is (1–1.5x), and the oxygen content 10–δ in the sample is (9+1.5x), where x can be calculated using Equation A-16.